WARSAW UNIVERSITY
OF TECHNOLOGY

Faculty of Physics

Ph.D. THESIS

Marcin Słodkowski, M.Sc., Eng.

Study of K^* resonances production in nuclear collisions at the CERN SPS energies

Supervisor
Marek Gaździcki, Ph.D., D.Sc.

Streszczenie

Praca stanowi część programu badań zderzeń ciężkich jonów wykonywanych dla wyjaśnienia własności silnie oddziałującej materii w wysokich temperaturach i przy dużej gęstości liczby barionowej. Do tego typu badań zbudowano eksperyment NA49 (typu stałej tarczy) rejestrujący cząstki naładowane. Jest on usytuowany na przyspieszaczu cząstek Super Proton Synchrotron (SPS) w Europejskim Ośrodku Badań Jądrowych (CERN). Podstawowe detektory tego eksperymentu, Komory Projekcji Czasowej - Time Projection Chambers (TPCs), rejestrują ślady cząstek naładowanych, co pozwala na rekonstrukcję ładunku elektrycznego, masy i pędu cząstki. W wysokich temperaturach, odpowiadającym dużym gęstościom energii, może następować przejście fazowe z materii hadronowej do materii uwolnionych kwarków i gluonów nazywanej plazmą kwarkowo gluonową - Quark Gluon Plasma (QGP). W czasie ponad dwudziestoletniego okresu badań wykryto szereg zjawisk wskazujących na produkcję QGP w zderzeniach ciężkich jąder przy wysokich energiach. Eksperyment NA49 odkrył efekty które wskazują, że próg na produkcję QGP znajduje się w obszarze energii SPS.

Podstawowym celem tej pracy jest analiza produkcji rezonansów $K^*(892)^0$ i $\bar{K}^*(892)^0$ w centralnych oddziaływaniach ołów-ołów przy energii wiązki 158 GeV na nukleon. Produkcja rezonansów jest szczególnie czuła na dynamikę zderzenia i warunki, w których ustają oddziaływania pomiędzy wyprodukowanymi cząstkami (tzw. wymrażenie, ang. freeze-out). Przekroczenie progu na produkcję QGP może być sygnalizowane przez anomalię krotności (liczba rezonansów na pojedyncze oddziaływanie) $K^*(892)^0$ i $\bar{K}^*(892)^0$ w zależności od energii zderzenia. Otrzymane krotności rezonansów mogą pomóc w wyznaczeniu progu przejścia fazowego pomiędzy materią hadronową (HG) a plazmą kwarkowo-gluonową (QGP).

Analiza produkcji rezonansów $K^*(892)^0$ i $\bar{K}^*(892)^0$ napotyka na duże trudności doświadczalne. Ze względu na małe krotności i szerokie rozkłady masy (krótki czas życia ~ 4 fm) sygnały rezonansów toną w olbrzymim tle generowanym przez wielką liczbę wyprodukowanych cząstek.

Podczas realizacji pracy przyśpieszono czasochłonne programy do analizy danych. W znaczący sposób ulepszono procedury do opisu tła masy niezmienniczej dzięki stworzeniu nowego algorytmu tzw. mieszania przypadków. Algorytm ten umieszczono w oprogramowaniu eksperymentu NA49. Określono efektywność detekcji potrzebnej do otrzymania ostatecznych wyników poprzez symulację przypadków i generowanie sygnału odpowiedzi detektora. Dla symulacji i rekonstrukcji przypadków dokonano szeregu optymalizacji skryptów generując dużą statystykę symulowanych zdarzeń.

W celu zbadania własności fizycznych mezonów K^* i $\bar{K}^*$ przeprowadzono szereg badań. Wydobyto sygnał rezonansów K^* i $\bar{K}^*$ z rozkładu masy niezmienniczej. Sygnał rezonansów jest dobrze widoczny w różnych przedziałach pośpieszności i pędu poprzecznego. Otrzymano rozkłady kinematyczne pośpieszności i pędu poprzecznego mezonów K^* i $\bar{K}^*$ wraz z określeniem ich krotności dla centralnych zderzeń ołów-ołów dla energii wiązki 158 GeV na nukleon. Uzyskane wyniki porównano z wynikami eksperymentu STAR i z modelami UrQMD oraz HGM. Zaobserwowano efekt tłumienia produkcji rezonansów w funkcji czasu życia dla rezonansów K^*, $\Lambda(1520)$ i ϕ. Prześledzono efekt tłumienia rezonansów K^* i $\bar{K}^*$ w funkcji wielkości systemu w porównaniu do danych modelu HGM.

Pokazano, że mezony K^* i $\bar{K}^*$ są szczególnie wrażliwe na dynamikę zderzenia. Spadek krotności rezonansów w porównaniu do modelu gazu hadronowego (HGM) jest zapewne spowodowany absorpcją krótkożyciowych cząstek w gęstej, silnie oddziałującej materii i zarazem rozpraszaniem produktów ich rozpadu. Informacje te mogą pomóc w oszacowaniu czasu
hadronizacji pomiędzy wymrażaniem chemicznym, a wymrażaniem kinetycznym.

Wyniki tej pracy motywują do dalszego pomiaru produkcji rezonansów w zderzeniach ciężkich jąder przy wysokich energiach, w szczególności do analizy rezonansów przy wszystkich energiach dostępnych w eksperymencie NA49 oraz do przeprowadzenia pełnej analizy produkcji krótkożyciowego rezonansu $\rho(770)$. Wyniki dotyczące jego produkcji mogłyby istotnie wzmocnić interpretacje wyników dotyczących rezonansów K^* przedstawionych w tej pracy.

Acknowledgements

My dissertation has been performed thanks to efforts of many friendly persons. At first I would like to thank my supervisor Professor Marek Gaździcki for critical remarks, hints and permanent mobilization to progressive and effective analysis, and help in every stage of this work together with reading of this manuscript. It was a pleasure to work with Professor Peter Seyboth. I appreciate his help in results interpretation, his interest in analysis and his kindness and understanding. I would like to thank for systematic weekly EVO meetings where research of my study was discussed.

I appreciate help of Robert Korus in training me at the early stage of my K^* resonance analysis. Many warm thanks to Tim Schuster for his help and introducing me to the NA49 experiment software problems. I wish to express my gratitude to Christoph Blume, Benjamin Lungwitz, Milica Utvic, Michael Mitrovski for active cooperation and sharing their experimental experience with me. Private exchange of results with Sascha Vogel was very useful for simulation and NA49 data comparison by using the UrQMD model. I would like to thank Claudia Hohne for sharing with me her results in different system (p+p, C+C,Si+Si) to make plots complementary with Pb+Pb system. I wish to thank all members of the IKF Institute group for their hospitality and kindness during my stays in Frankfurt. Thanks to whole Collaboration for the possibility to use NA49 data.

I would like to thank Professor Jan Pluta for giving me the opportunity and support during realization of my Ph.D. studies. Specially thanks to Katarzyna Grebieszkow for creative scientific discussions which helped me to understand the method of NA49 analysis. I thank all members of HIRG group from Warsaw University of Technology collaboration for effective cooperation.

My wife Agnieszka Słodkowska I wish to thank for understanding, patience and active support during realization of my work. This work has been supported by Polish Ministry of Science and Higher Education in years 2007-2009 as a research project grant no. 0297/B/H03/2007/33.

This thesis I dedicate my daughter Kamila,
who was born in the final
stage of my work.

Contents

Chapter 1

Introduction

This thesis is a part of the broad program to study hadron production in central lead+lead collisions at beam energy 158 GeV per nucleon (corresponding to center-of-mass energy 17.3 GeV per nucleon pair).These investigations allow to establish properties of strongly interacting matter at high energy densities created in relativistic nucleus-nucleus collisions. The work is based on the data registered by the NA49 experiment located at the Super Proton Synchrotron (SPS) accelerator at European Organization for Nuclear Research (CERN) in Geneva, Switzerland. The NA49 detector is a large acceptance spectrometer with particle identification capabilities, where a beam lead nuclei collide with a fixed lead target. Charged particles are registered by the Time Projection Chambers (TPCs) in the form of tracks. Typically about 1000 tracks are recorded in central Pb+Pb collisions at 158 GeV per nucleon (this is the highest SPS energy for Pb+Pb interaction).

With increasing collision energy, the energy density of matter created in nucleus-nucleus collisions increases. At low energy densities strongly interacting matter is in the form of a gas of hadrons. At sufficiently high energy densities ($\geqslant\ 0.6-1$ GeV/fm^3) the created matter is expected to be in a state in which quarks and gluons are deconfined; so-called quark-gluon plasma (QGP) is created. During the last twenty years of research, there were numerous observations of possible signatures of QGP creation. Difficulties in data interpretation are caused by the requirement that the QGP signatures should survive the process of hadronization not succumbing to the change from the QGP state to the hadrons registered in particle detectors. The results of the NA49 energy scan program with lead-lead collisions serve as an evidence for the onset of deconfinement at the low CERN SPS energies. Some of the predicted signatures of QGP appear rapidly when crossing the CERN SPS low energy domain (30-60A GeV).

This work is a part of a vivid effort to study resonance production in nucleus-nucleus collisions. Resonances are strongly decaying hadrons with lifetimes that are comparable to the lifetime of hot dense matter produced in heavy-ion collisions. They are particularly sensitive to the dynamics of collision as well as conditions at which strong interactions between hadrons cease, so-called freeze-out of the system.

The specific goal of this work is to analyze the production of $K^*(892)^0$ and $\bar{K}^*(892)^0$ resonances in central Pb+Pb collisions at the top SPS energy, 158A GeV. This is the first step towards establishing the energy dependence of $K^*(892)^0$ and $\bar{K}^*(892)^0$ production properties in the region where the onset of deconfinement is located. Crossing the threshold for the production of QGP may also influence the production of strange resonances $K^*(892)^0$ and $\bar{K}^*(892)^0$, and thus a next evidence for the onset of deconfinement may be established. Measuring the $K^*(892)^0$ and $\bar{K}^*(892)^0$ is important due to their short life-time and the non-zero strangeness content. The strangeness production carries information on the early stage of collisions, when its yield is established. The short life-time results in a sensitivity to the rescattering and regeneration effects in hadronic phase, which properties and duration depends on the history of collisions. Experimental analysis of resonance production in nucleus-nucleus collisions encounters huge difficulties and thus the existing data are relatively poor. First, this is due to the small multiplicities and the broad mass distributions (short life-times) of resonances. Second, due to a high multiplicity of all produced hadrons and consequently very high background present in the resonance analysis. Thus, the weak resonance signal is covered by a flood of background.

The thesis is organized as follows. In Chapter 2, the theoretical background relevant for this work is introduced. The experimental setup and the reconstruction software are described in Chapter 3. Special attention is given to the particle identification using the specific energy loss in the TPC gas, fundamentals of this procedure are presented in Chapter 4. The data analysis methods are explained in details in Chapter 5. The results on rapidity and transverse momentum spectra of $K^*(892)^0$ and $\bar{K}^*(892)^0$ are shown in Chapter 6. The data are compared to the other measurements and to the Ultrarelativistic Quantum Molecular Dynamics (UrQMD) model as well as to the Hadron Gas Model (HGM) in Chapter 7. The work is summarized in Chapter 8.

Chapter 2

Theoretical background

In this chapter theoretical concepts which are needed to understand a motivation of the performed experimental study are summarized. The Standard Model of elementary particles and interactions is presented in section 2.1. The concept of strongly interacting matter (SIM) and a hypothetical phase transition between hadron-resonance gas (HRG) and quark gluon plasma (QGP) are discussed in section 2.2. In Fig. 2.1 an artistic view of two phases is shown: hadronic matter and the state of quark gluon plasma. The experimental role of nucleus-nucleus collisions in the study of the phase diagram of SIM is presented in section 2.3. Signatures of the phase transition between HRG and QGP are discussed in section 2.4. The production of strange resonances and their role in the study of A+A collisions is introduced in section 2.5.

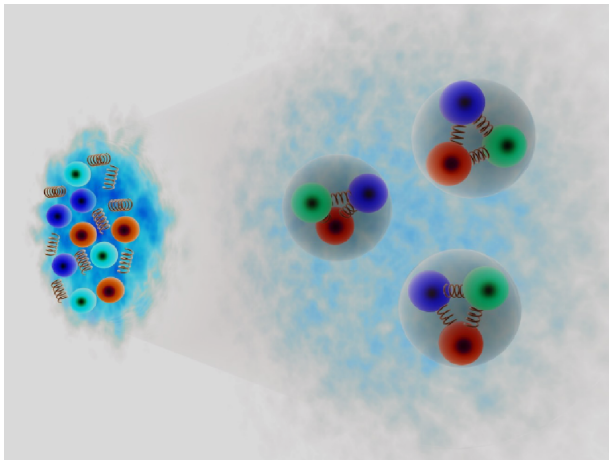

Figure 2.1: Artistic view of the two phases of strongly interacting matter, quark-gluon plasma (left) and hadron-resonance gas (right) [1].

2.1 Standard Model

The Standard Model summarizes the current orthodox view on the elementary particles and their interactions. The main theoretical idea was born in 1970s and it was developed in 1980s. Up to now, almost all strong, electro-magnetic and weak tests of the Standard Model, that describes the three fundamental forces, have agreed with its predictions. However, the Standard Model falls short of being a complete theory of fundamental interactions, primarily because of its lack of gravity inclusion. Furthermore, quantitative predictions for strong interactions are up to today limited only to a very rare class of processes with a very large momentum transfer. The Standard Model has a large number of numerical free parameters ($\geqslant 19$) that must be put "by hand" into the theory. The matter particles described by the Standard Model, all have an intrinsic property known as "spin" that absolute value is determined to $\frac{1}{2}$. Thus, the matter particles are fermions and they follow the Pauli exclusion. Apart from their antiparticle partners, a total of twelve different types of matter particles are known and accounted by the Standard Model. Six of these are quarks: up, down, strange, charm, top and bottom, and the other six leptons: electron, muon, tau, and their corresponding neutrinos [2, 3, 4].

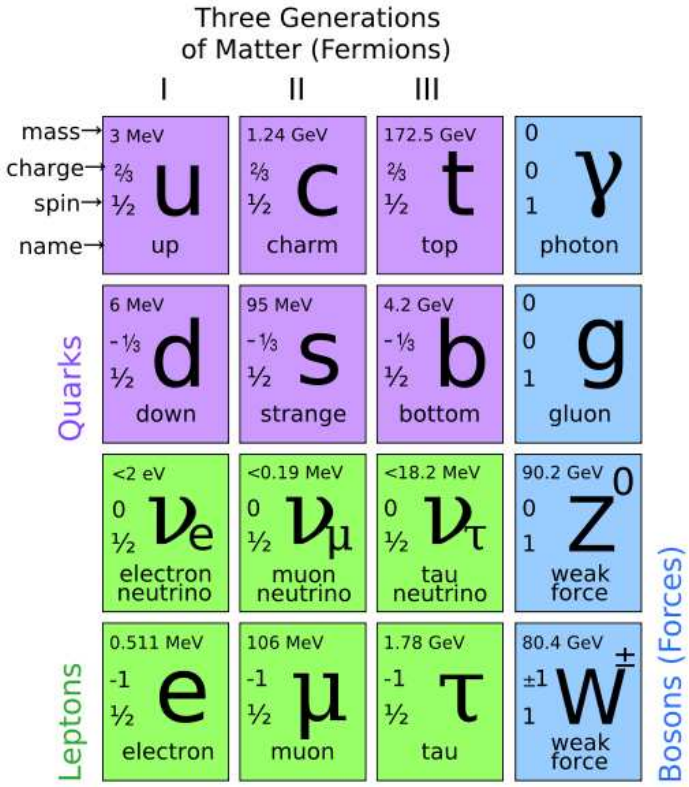

Figure 2.2: Particles of the Standard Model. Figure taken from [5].

In the Standard Model the interactions between matter particles are pictured as an exchange of bosons. Electromagnetic interactions are mediated by photon γ exchange, weak interactions are described by bosons W^+, W^- and boson Z^0. The strong interactions are determined by gluons. Each quark is able to have one of the three colors (additional quantum number) which indicates state of charge. Finally, the three colorful charges give color charge which is equal to zero. It is similar situation to tone of light for example blue, green, and red. After mixing the three colors together, they give white neutral color. Furthermore, each quark has an opposite charge particle that is called anti-quark. They have three anti-colorful charges (anti-red, anti-green, anti-blue). So far all observed strongly interacting particles are color neutral, they are called hadrons and consists of different combinations of quarks and anti-quarks. Two types of hadrons are distinguished: mesons and baryons. Mesons contain quark-antiquark pairs, barions contain quark-quark-quark combination and anti-barions contain three anti-quark structures. Thus quarks are confinemed into hadrons and this is an unique property of strong interactions. A carrier of strong interactions is gluon which has color charge (an unit of color and unit of anti-color). A particular feature of strong interactions is confinement, it is when the distance between two quarks increases then the interaction between them becomes stronger. The strong interactions are described by the Quantum Chronodynamics (QCD). In the description of quark properties it is necessary to take into account also electromagnetic and weak interactions. The properties of particles which were discussed above are summarized below and in Fig. 2.2.

- Each quark carries one of three color charges (red, green or blue), enabling it to participate in strong interactions.
- The up-type quarks (up, charm, and top quarks) carry an electric charge of $+\frac{2}{3}$, and the down-type quarks (down, strange, and bottom) carry an electric charge of $-\frac{1}{3}$, enabling both types to participate in electromagnetic interactions.
- Leptons do not carry any color charge - they are color neutral, preventing them from participating in strong interactions.
- The electron-type leptons (the electron, the muon, and the tau lepton) carry an electric charge of -1, enabling them to participate in electromagnetic interactions.
- The neutrino-type leptons (the electron neutrino, the muon neutrino and the tau neutrino) carry no electric charge, preventing them from participating in electromagnetic interactions

- Both quarks and leptons carry a handful of flavor charges, including the weak isospin, enabling all particles to interact via the weak interactions.

2.2 Phase diagram of Strongly Interacting Matter

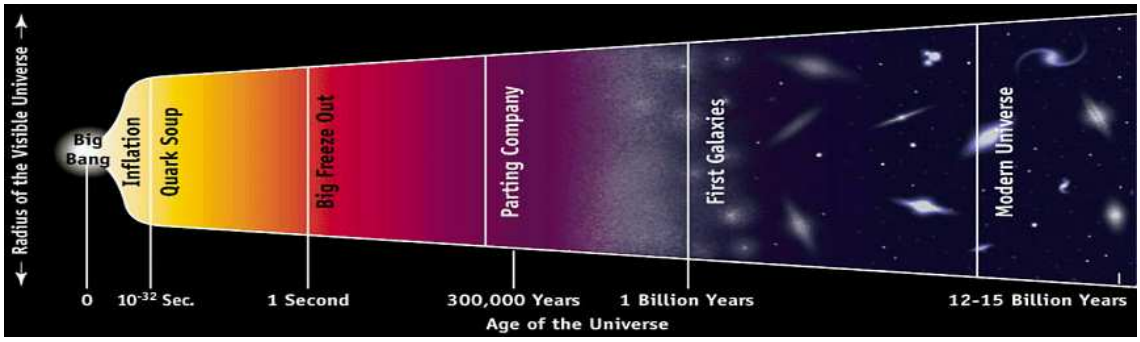

Figure 2.3: Sketch of a possible Universe evolution. Figure taken from [6].

Properties of an equilibrium state of strongly interacting particles, Strongly Interacting Matter (SIM), have been discussed since beginning of 1970s [7]. One of the goals of contemporary physics is to establish properties of SIM its phases and transitions between them. It is commonly believed that QGP existed in the first moments of the Universe creation (see Fig. 2.3 for illustration) and today may exist in the interior of neutron stars. The only method which allows us to study QGP in the laboratory is to collide heavy nuclei. At the early stages of the collisions QGP may be created [8, 9].

Accordingly to the current theoretical prediction the state in which matter exists depends on values of the thermodynamical parameters, such as temperature, T, and baryo-chemical potential, μ_B. Fig. 2.4 shows the hypothetical phase diagram of SIM in ($T - \mu_B$) plane. The matter at high values of T and μ_B exists in the QGP state, whereas the matter at low values of T and μ_B in the state of HRG. The gray strip indicates a region of the first order phase transition which the matter exists in the mixed phase. The strip ends by the critical point of the second order. Between this point and $\mu_B = 0$ the cross-over region is located. The critical point is predicted by QCD based calculations using analytical methods [10] and using numerical lattice QCD simulations [11]. At zero μ_B QCD methods allow to determine the equation of state EoS of QCD and indicate that the transition is a crossover.

The current best estimate of the location of the critical point gives its position at $T_E = 162 \pm 2$ MeV and $\mu_B^E = 360 \pm 40$ MeV [12, 13, 14]. The search for the critical point is the

aim of future heavy-ion programs at the CERN SPS and at the BNL RHIC [15]. Results of the first estimate [16] of the shape and size of a phase diagram region in which matter properties are affected by the vicinity of the critical point are shown in Fig. 2.5. Guided by consideration of [16] the critical point signals were parametrized Gaussian shapes in T and μ_B with $\sigma(T) \approx 10$ MeV and $\sigma(\mu_B) \approx 30$ MeV respectively [17].

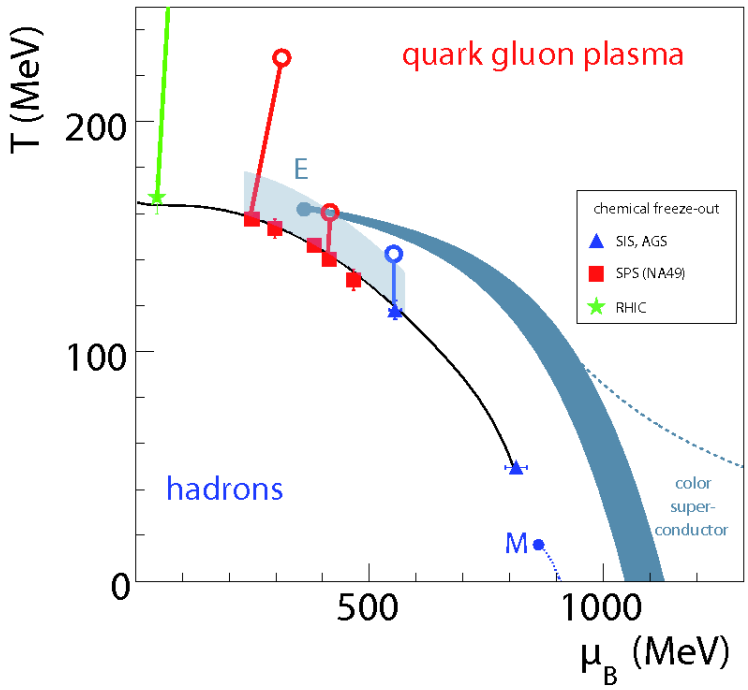

Figure 2.4: QCD phase diagram of nuclear matter in terms of the temperature (T) and chemical potential (μ_B). Solid points indicate chemical freeze-out points of central heavy ion collisions, whereas the colored solid line hypothetical trajectories of the matter created in these collisions. Figure taken from [1].

Potentially important for the search of critical point is that there is an extended $T - \mu_B$ region which is affected by the vicinity of the critical point.

2.3 Ultrarelativistic nucleus-nucleus collision

The main goal of research programs, in which relativistic nucleus-nucleus collisions are studied, is to establish properties of strongly interacting matter and, in particular, discover its high density state the Quark-Gluon Plasma. For this purpose, nuclei from Pb to proton have been collided with various collision energies. Matter in the nuclei before collisions is in its low energy density state and consists of bound protons and neutrons. Soon after a collision hot and dense fireball is formed. Its proprieties depend on the size and energy of the colliding nuclei.

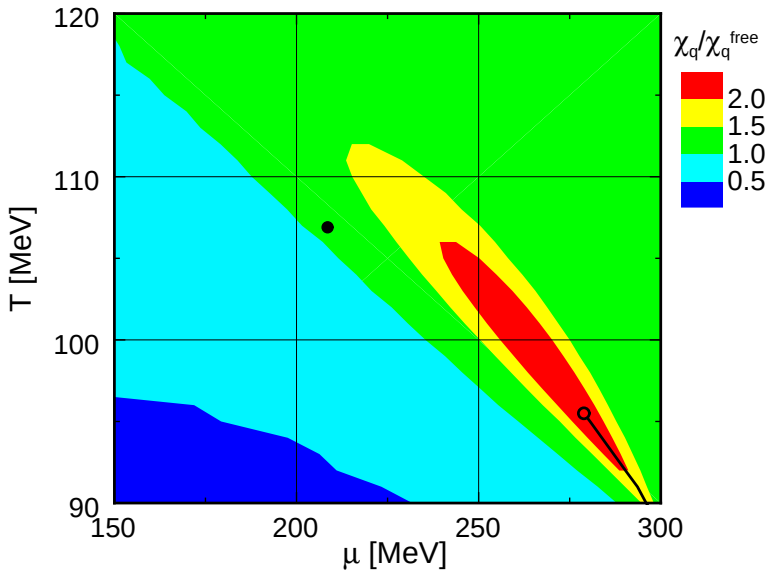

Figure 2.5: The model calculations of the shape of critical region ($\mu = \mu_B/3$). The values of quark number susceptibility is divided by that of the massless free theory (χ_q/χ_q^{free}). Figure taken from [16].

In particular, it temperature increase with increasing collision energy. At sufficient high energies the fireball energy density is high enough to liberate quark and gluon from their hadrons. The matter in the QGP state is formed. The sketches of the space-time evolution of this dense matter are shown in Figs 2.6 and 2.7. The fireball created in the initial stage of collisions expands and cools down maintaining local thermodynamical equilibrium (for RHIC $\sim 0.6 \rightarrow$ at $\tau_0 = 1$ fm/c). This expansion can be modeled by relativistic hydrodynamics [18, 19, 20]. This state of matter might be represented by fluid dynamic. Its evolution is simulated using finite difference algorithm [21, 22, 23, 24, 25]. When the matter approaches $T \simeq (150 - 200)$ MeV a phase transition from QGP to HRG takes place [26]. Hadrons and resonances are formed. During further expansion and cooling-down first inelastic (chemical freeze-out) and later elastic (kinetic freeze-out) interactions cease. Final state hadrons are detected by an experimental apparatus surrounding a collision point.

Nucleus-Nucleus collisions at relativistic energies have been studied experimentally over last 40 years in several laboratories which carried various research programs performed by numerous experiments. In particular, these were performed in: the JINR Dubna, the LBL Berkeley, the BNL AGS, the CERN SPS and the BNL RHIC.

In the near future new programs shall start at the CERN SPS, the CERN LHC, the BNL RHIC (low energy), the JINR NICA and the FAIR SIS-100/300.

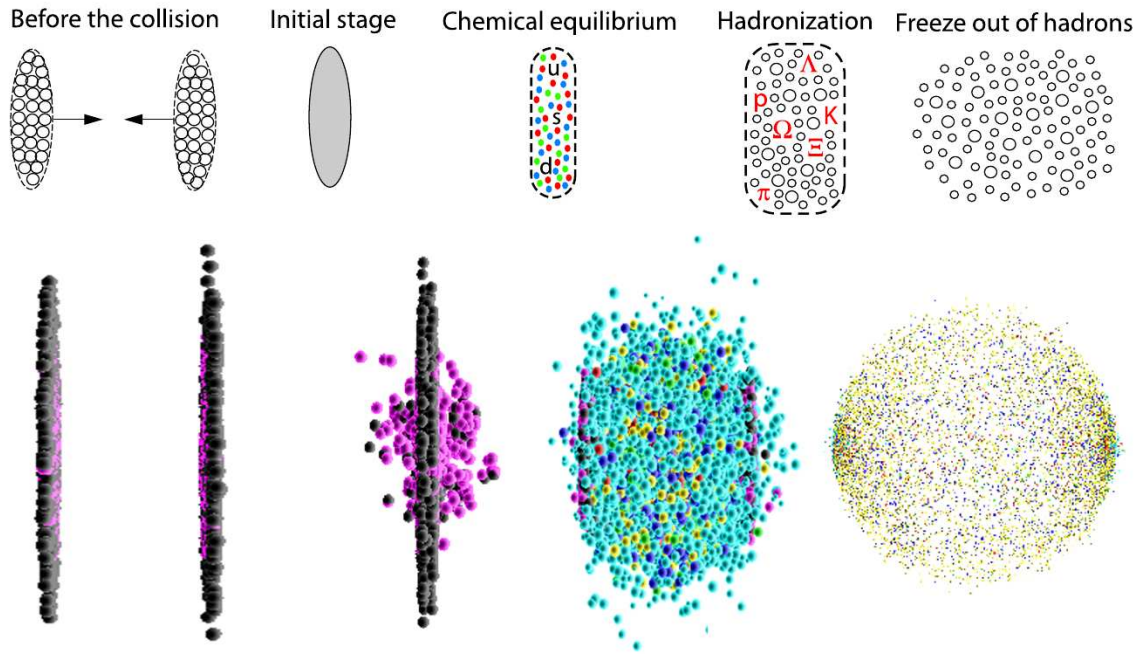

Figure 2.6: The space-time evolution of a heavy ion collision. Top: stages of evolution [28]. Bottom: visualisation of UrQMD model simulation [29, 30].

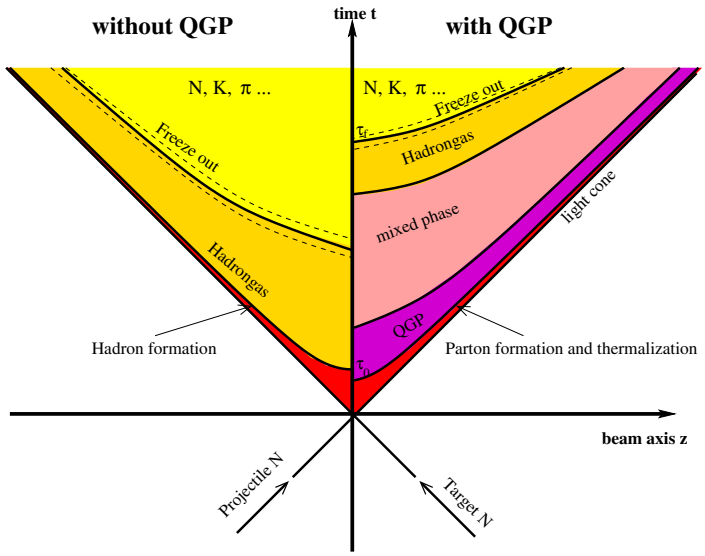

Figure 2.7: The space-time evolution of nucleus-nucleus collisions with (right) and without (left) QGP formation. Figure taken from [31].

2.4 NA49 searches for the transition: HRG - QGP

Two strategies have been followed in experimental studies of nucleus-nucleus collisions with the aim to investigate properties of SIM. First collisions of heavy nuclei at the highest possible energy have been studied with the hope to identify signals of the QGP creation at early stage. Many signatures of QGP creation have been proposed. Among the most popular are: an enhanced production of strange hadrons and a suppression of production of J/ψ mesons as well as high transverse momentum hadrons. These signals were observed in A+A collisions at the CERN SPS [32] and BNL RHIC [33], but appeared to be not specific only for QGP. Second, the energy dependence of hadron production properties have been studied with a hope to observe the signals predicted when crossing a threshold energy for the QGP production, the so-called onset of deconfinement. This strategy have been followed since mid 90s by the experiment NA49 experiment at the CERN SPS. The results of this program confirmed the predictions for the onset of deconfinement and suggested that the threshold energy for the QGP creation is located at about 30A GeV ($\sqrt{s_{NN}} \approx 7.62$ GeV). The future measurements at the CERN SPS [34] (NA61/SHINE [35]) and at BNL RHIC [36] (STAR [37], PHENIX [38]) are planed in order to verify the NA49 results as well as to perform a detailed study of the transition region. In the following subsections the basic ideas and the recent results on the onset of deconfinement are summarized.

2.4.1 The onset of deconfinement - SMES model

The Statistical Model of The Energy Stage (SMES) [39] predicts that the onset of deconfinement is located between top AGS (11.7A GeV) and top SPS energies (158A GeV). The NA49 data suggest that the deconfinement starts at about 30A GeV [40, 41].

The main assumptions of the SMES model are:

- the matter created at the early stage of A+A collision is in equilibrium,
- at low temperatures the matter is in the confined state whereas at high temperatures it is deconfined state,
- the transition is assumed to be of the 1^{st} order,
- the entropy and total number of s and $\bar{s}$ quarks are assumed to be conserved from the early to the final states.

The SMES model has several additional assumptions. The ideal gas and the "Bag model" equations of state are assumed for the confined matter and QGP, respectively. Characteristic property of the first order of phase transition is presence of the mixed phase, the phase in which confinement and deconfinement phases coexist. The SMES model assumes that the temperature of the phase transition is $T_c = 200$ MeV, somewhat larger than the temperature of the chemical freeze-out. The number of internal degrees of freedom g increases at deconfinement, due to an activation of partonic degrees of freedom. In final stage the entropy is proportional to the total number of pions. Thus, the SMES model relates the properties of the early stage, be the QGP or the confined matter, with the properties of the final state.

The SMES model predicts rapid changes in the energy dependence of several hadron production properties. Three of them, the 'kink', the 'horn' and the 'step' (Fig 2.8) concern inclusive particle production, whereas the other two event-by-event fluctuations of hadron production properties (the 'shark fin' and the 'tooth' see [39] for details). The first three will be discussed here in detail as only for them a conclusive comparison with the experimental data is possible.

The 'kink' prediction concerns the energy dependence of the total entropy to the number of participant nucleon. If the state of matter does not change the total entropy is predicted to increase linearly with Fermi's energy [40]:

$$F \equiv \left[\frac{(\sqrt{s_{NN}} - 2m_N)^3}{\sqrt{s_{NN}}}\right]^{1/4}, \tag{2.1}$$

where $\sqrt{s_{NN}}$ is the center-of-mass energy per nucleon pair and m_N the rest mass of the nucleon. The slope of this dependence is proportional to $g^{1/4}$, where g is the internal number of degrees of freedom at the early stage. In the QGP g is larger than in the confined matter due to the activation of partonic degrees of freedom. Thus, the SMES model predicts an rapid increase of the slope of entropy dependence on the Fermi's energy measure (the 'kink') at the onset of deconfinement.

The 'horn' structure concerns the energy dependence of the strangeness to entropy ratio. A narrow maximum is expected and called the 'horn'. It is due to a reduction of the ratio of internal number of degrees of freedom for strange and non-strange particles and a reduction of the mass of strangeness carries at deconfinement.

The 'step' structure concerns the energy dependence of the early stage temperature, which in the final state is reflected in the energy dependence of the inverse slope parameter of the trans-

verse mass spectra of produced hadrons. In the pure phases, the confined matter and the QGP, the temperature increase with increasing energy density and thus with increasing collision energy. In the mixed phase the temperature is independent of the energy density and consequently collision energy and is equal to the assumed temperature of the phase transition, in the SMES $T = T_c = 200$ MeV. Therefore the SMES predicts a step like structure in the mixed phase region with the plateau extending approximately over domain $2.23 < F < 2.9$ GeV$^{1/2}$ (p_{lab} from 30A to 64A GeV).

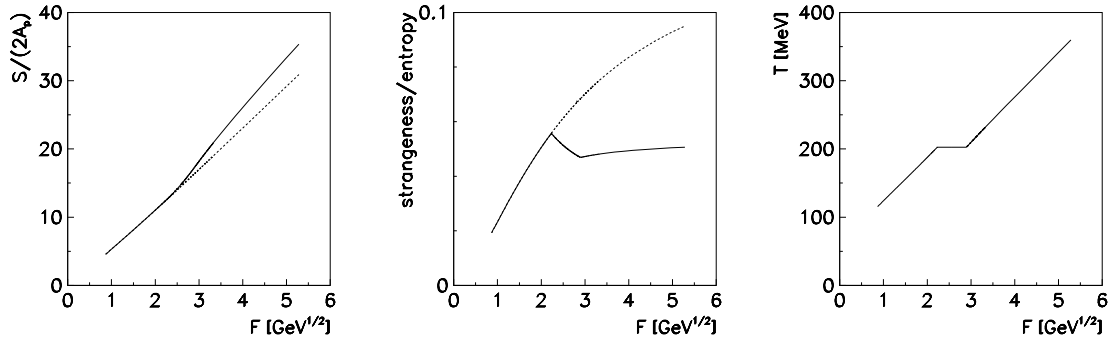

Figure 2.8: The SMES model predictions: left - the kink structure, middle - the horn structure, right - the step structure. Figure taken from [39].

The predictions of SMES model were verified by the NA49 experiment at the CERN SPS. The study was focused on the pion and kaon production in central Pb+Pb collisions at 20A, 30A, 40A, 80A and 158A GeV which were registered during the data taking periods in 1999, 2000 and 2002. Fig. 2.9 shows the mean multiplicity $\langle\pi\rangle = 1.5\,(\langle\pi^+\rangle + \langle\pi^-\rangle)$ per wounded nucleon $\langle N_w\rangle$ as a function of the Fermi's energy measure. The world data are compared with the SMES prediction. The results are consistent with the kink-like structure, however other models (HSD and UrQMD) which do not assume the onset of deconfinement also can approximately reproduce the results.

The strangeness to entropy ratio predicted within the SMES to have the 'horn' structure at the onset of deconfinement is in a good approximation proportional to the $\langle K^+\rangle\,/\,\langle\pi^+\rangle$ ratio and the E_s ratio defined as:

$$E_s = \frac{\langle\Lambda\rangle + \langle K\rangle + \left\langle\bar{K}\right\rangle}{\langle\pi\rangle}. \tag{2.2}$$

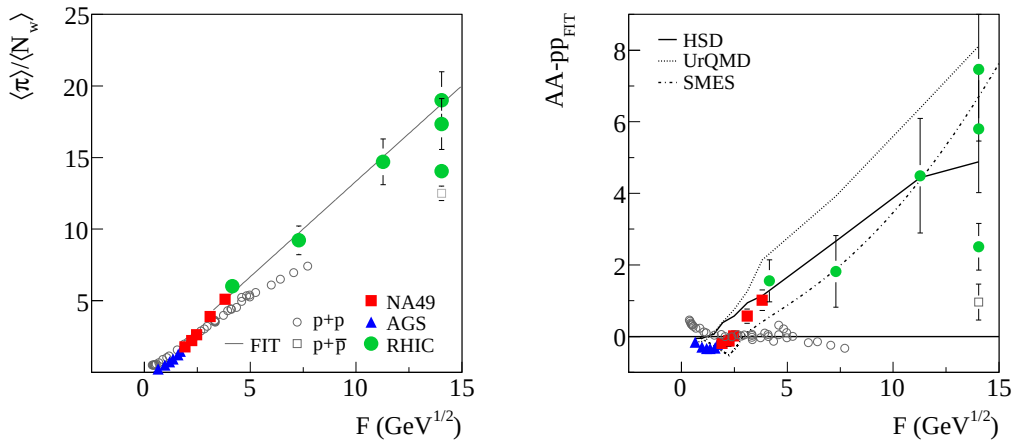

Figure 2.9: Left: Energy dependence of the mean pion multiplicity per wounded nucleon measured in central Pb+Pb and Au+Au collision (solid symbols), compered to the corresponding result from $p+p$ reaction (empty circle). Right energy dependence of the difference between the measured mean pion multiplicity per wounded nucleon and a parametrization of $p+p$ data. The meaning of solid and empty symbols is the same as in the left plot. The lines indicate various model predictions. Figure taken from [40].

Within the model E_s is calculated as:

$$E_s = \frac{(N_s + N_{\bar{s}})\,\zeta}{(S - S_s)\,/4 - \alpha\,\langle N_p \rangle}, \tag{2.3}$$

where $\zeta = 1.36$ is experimentally estimated ratio between total strangeness and strangeness carried by Λ and $K + \bar{K}$ mesons, S_s is the fraction of entropy carried by strangeness carries and $\alpha = 0.35$ is a correction for the transfer of entropy to baryons. More details can be found in [39]. Calculations within the SMES for the E_s show in fact the 'horn-like' structure, which is consistent with the world experimental data, see Fig. 2.10. Results on the $\langle K^+ \rangle \,/\, \langle \pi^+ \rangle$ ratio also show the 'horn-like' structure. The SMES model can reproduce the sharp maximum in the $\langle K^+ \rangle \,/\, \langle \pi^+ \rangle$ and E_s ratios located at about $30A$ GeV. The UrQMD with the bag model equation of state and strong first order of phase transition in qualitative agreement with the experimentally observed step-like behaviour in the $< m_T >$ excitation function [42].

The world data on the energy dependence of the inverse slope parameter of the transverse mass spectra of K^+ and K^- mesons are shown in Fig. 2.11. The data confirm the predicted 'step-like' structure, with the plateau characteristic for the mixed phase region. A linear increase of the inverse slope parameter with the collision energy is seen outside of the plateau, for AGS and RHIC energies. The model assuming the first order phase transition reproduces well the data, whereas the models which do not assume the transition fail to describe them.

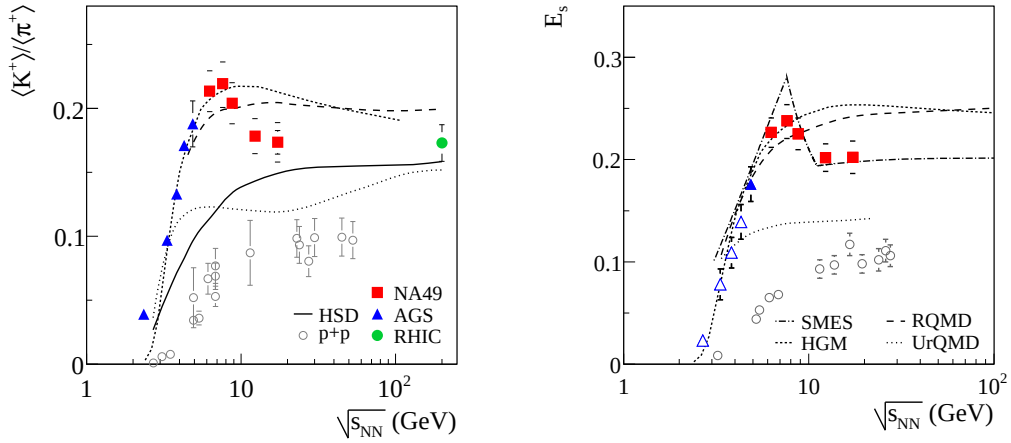

Figure 2.10: Left: Energy dependence of $\langle K^+ \rangle / \langle \pi^+ \rangle$ ratio measured in central Pb+Pb and Au+Au collisions (solid symbols) compered to corresponding results from $p+p$ reaction (empty circles). Right: Energy dependence of the relative strangeness production as measured by E_s ratio in central Pb+Pb and Au+Au collisions (solid symbols) compered to corresponding results from $p+p$ reactions (empty circles). The curves in figures shows predictions of various models. Figure taken from [40].

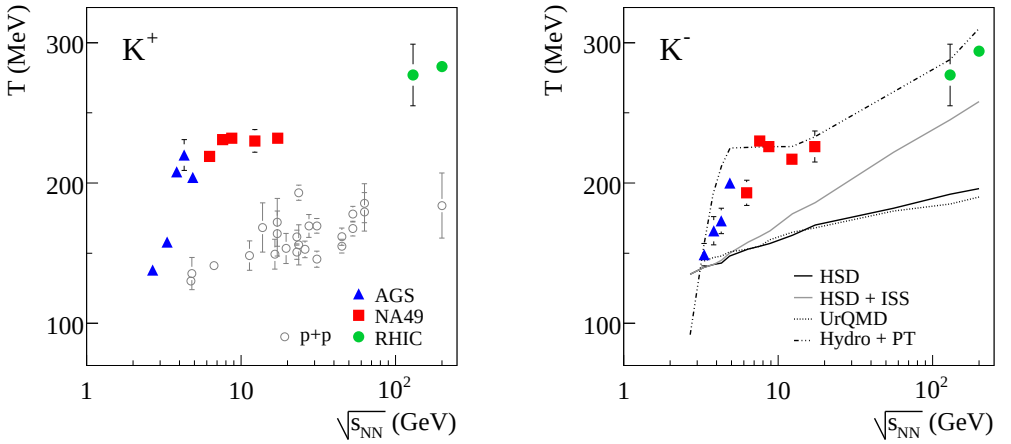

Figure 2.11: Energy dependence of the inverse slope parameter T of the transverse mass spectra of K^+ (left) and K^- mesons (right) measured at mid-rapidity in central Pb+Pb and Au+Au collisions. The K^+ slope parameters are compered to those from $p+p$ reactions on the left-hand plot (empty circles). The curves on right-hand plot represent predictions from various models. Figure taken from [40].

The phase transition to QGP seems to be observed at the low SPS energies, future measurements can further confirm this hypothesis. The signatures of the onset of deconfinement, which have been described above, are observed in the region of low SPS energies. The experiments at the CERN SPS such as NA49 and its successor NA61 have a challenge to investigate the area of the mixed phase and give a significant evidence for phase transition.

2.4.2 Other signatures of QGP creation

The pioneering signatures of QGP were proposed in the 1980s. Some of them are briefly discussed below.

- **Strangeness enhancement.** In dynamical approaches to the A+A collisions the strange hadrons or quarks are assumed to be produced in elementary interactions of matter constituents (quarks and gluons or hadrons). As the strange quark mass is much lower than the masses of strange hadrons, the strangeness production in QGP was originally expected to be much easier than in the confined matter [43, 44, 45]. Thus, strangeness yield relative to the pion yield was predicted to increase when the threshold energy for QGP creation is crossed. This prediction is in contradiction with the NA49 experimental data, and with SMES predictions which indicated that the relative strangeness production decreases with increasing energy [39].

- **Charmonium suppression.** The suppression of charmonium [1] production relative to the Drell-Yan pairs [2] was predicted as a signal of QGP [46, 47]. This is due to the expectation that in QGP the quark-antiquark QCD potential (color charges of charm quarks) will be screened by deconfined quarks and gluons. Indeed the strong J/ψ suppression was measured in central Pb+Pb collisions at 158A GeV by the NA50 experiment, and the results are presented for example in [46, 48]. This suppression cannot be explained via J/ψ absorption in normal nuclear matter. It is seen only for central Pb+Pb collisions at energy density higher then 2.2 GeV/fm^3 [48]. The data can be, however, explained by the statistical models of J/ψ production [49], which do not invoke the QGP creation. Moreover the recent result from PHENIX experiment at RHIC surprisingly showed the

[1] Charmonium is charm quark/anti-charm meson so-called quarkonium.

[2] Quark of one hadron and an antiquark of another antihadron annihilate, creating a virtual photon or Z boson which then decays into a pair of oppositely-charged leptons.

same level of J/Ψ although the energy density at RHIC is much higher. This puzzle can be probably solved only at LHC heavy ion experiments [50].

- **Electromagnetic probes.** Leptons and photons created during the A+A collisions travel practically undistorted through the created dense matter as they do not participate in strong interactions. The electromagnetic radiation may be an important probe to study the early stage of the collision process. It can be produced in the QGP phase via $q\overline{q}$ annihilation and also in the hadron gas phase, essentially via $\pi^+\pi^-$ annihilation. The thermal radiation emitted via quark-anti-quark annihilation process produces an exponential spectrum with a slope parameter reflecting the temperature of the system [51, 52, 54]. Photons and leptons may provide a measure of the thermal radiation from a quark-gluon plasma, if the QGP emission can be isolated from the other processes. However, the yields of electromagnetic probes are small with respect to the background processes, it is electromagnetic decays of hadrons and resonances after freeze-out [55]. Up to now there are no conclusive experimental results concerning the electromagnetic radiation from the QGP phase. Nevertheless, the direct photon measurements are perform by many experiments.

- **Jet quenching.** The jets are strongly focused beams of hadrons which are produced as a product of a fragmentation of quarks or gluons with high transverse momenta, p_T. In heavy ion collisions jets can be produced by the hard scattering of quarks and gluons from colliding nuclei. In particular, so-called dijets are two jets emitted in the opposite direction. Due to momentum conservation each jet is expected to have a "brother" jet emitted in the opposite direction. In the case of QGP creation a strong jet quenching in the dense QGP matter is expected [56, 57]. This should cause a suppression of the jet yield, as well as a suppression of the "brother" jet production. In fact, experimental data at the BNL RHIC confirm these predictions [58].

2.5 Production of resonances

Resonances were discovered in 1950s when strong maxima were observed in the meson-nucleon interaction cross section as a function of collision energy. These phenomena were classified as nucleon excitations. The excitation life time is about 10^{-23}s and the phenomenon was called production of resonances. At the beginning, these "resonance states" were not seen as particles.

First, a resonance as a particle was discovered in the 1952 and it was $\Delta(1238)$ resonance produced in pion-proton interactions. Mass of the resonance is defined as a position of the peak maximum in the invariant mass spectra of its decay products. The width of peak is connected to the lifetime of the resonance according to the Heisenberg uncertainty principle $\tau = \frac{h}{\Gamma}$. The meson for example $\rho(770)$ has a mass 771 MeV/c^2 and width 149 MeV which corresponds to lifetime $\tau = 4.3 \cdot 10^{-24}$s. Soon after the first observations there was a sequence of discoveries of new resonance states. Due to very short life times only the resonance decay products can be observed in the detector. For a long period it was discussed whether resonances are real particles [59, 60]. Currently, it is commonly accepted that the resonances are particles like any other elementary particles but they only have a short life time. Clearly, a resonance decay process conserves all quantum numbers as well as energy and momentum [61, 62, 63]. Thus, the measurement of the decay products determines the resonance properties. The invariant mass of N particles is given by:

$$m_{inv} = \sqrt{\left(\sum_{i=0}^{N} E_i\right)^2 - \left|\sum_{i=0}^{N} \vec{p_i}\right|^2} \tag{2.4}$$

in the particular the invariant mass of two particles is:

$$m_{inv} = \sqrt{(E_1 + E_2)^2 - (\vec{p_1} + \vec{p_2})^2}. \tag{2.5}$$

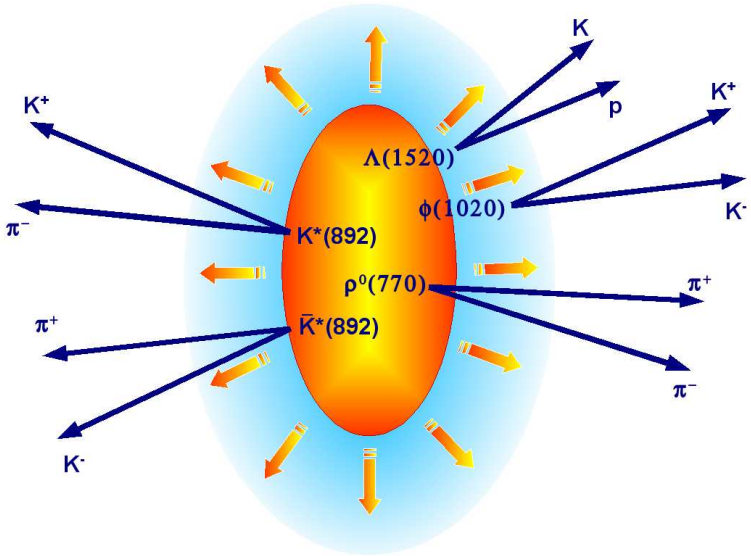

Figure 2.12: Sketch of the resonance production and decay in a heavy ion collision.

The study of resonance production in heavy ion collisions is difficult because in the nucleus-

nucleus collisions a large number of hadrons is produced. This leads to a very large combinatorial background. Nevertheless, numerous experimental results on the resonance production in A+A collisions are already published. In particular, these can be found in:
- overview of the resonance production in Ref. [8, 64, 65],
- resonance production in heavy ion collisions at STAR in Ref. [66],
- ϕ production in Pb+Pb collisions in Ref. [67, 68, 69],
- K^* production in Au+Au and p+p collision at $\sqrt{s_{NN}} = 200$ GeV in Ref. [70],
- K^* production in relativistic heavy ion collisions at $\sqrt{s_{NN}} = 130$ GeV in Ref. [71],
- K^* production in Cu+Cu and Au+Au collision a $\sqrt{s_{NN}} = 62.4$ GeV and 200 GeV in STAR in Ref. [72].

Life-time of resonances is similar to the duration time of the hadronization, hadronic expansion and freeze-out processes. Thus, resonances give unique opportunity to study these late phases of A+A collisions. Furthermore, strange resonances are sensitive to the strangeness production. As both, strangeness production and the system space-time evolution should be sensitive to the creation of QGP, the resonance production is considered to carry an important information on nucleus-nucleus collisions. The resonances can be produced directly at the hadronization or formed later in the processes of hadron-hadron scattering. The decay products may interact with the produced matter and thus lead to a suppression of the resonance signal if the decay take place before the freeze-out.

The high-density state evolves into a hadron resonance gas which finally decouples into the observed hadrons. The $K^*(892)^0$ and $\bar{K}^*(892)^0$ resonance states contain an $\bar{s}$ and s valence quark respectively and therefore are sensitive to the strangeness enhancement effects. Due to the short lifetime of $K^*(892)^0$ and $\bar{K}^*(892)^0$ (~ 4 fm/c) the resonance productions is sensitive to the hadronic phase. Thus, scattering process might destroy or regenerate them and thus their yields were conjectured to be sensitive to the duration of the hadronic fireball stage [73, 74]. Furthermore, $K^*(892)^0$ and $\bar{K}^*(892)^0$ propagate in dense matter thus fraction of produced resonances might be absorbed. In Fig. 2.12 there is an illustration of $\rho(770)$, $\Lambda(1520)$, $\phi(1020)$, $K^*(892)$ and $\bar{K}^*(892)$ production during the nucleus-nucleus collision.

Studies of $K^*(892)^0$ production at mid-rapidity in p+p, Cu+Cu, and Au+Au collisions at RHIC energies have been performed by the STAR collaboration [70, 71, 72]. This thesis present measurements of $K^*(892)^0 \rightarrow K^+\pi^-$ and $\bar{K}^*(892)^0 \rightarrow K^-\pi^+$ production at the CERN SPS in central Pb+Pb collision at $158A$ GeV. The data were recorded by NA49 experiment.

Chapter 3

NA49 experiment at the CERN SPS

The NA49 experiment is described in this chapter. The beams and beam counters are introduced in section 3.1. The overview of the experimental set-up is given in section 3.2. The Time Projection Chambers (TPCs), the most important sub-detectors, are presented in section 3.3. The Time-of-Flight (TOF) detectors and the Veto calorimeter are characterized in sections 3.4 and 3.5, respectively. Data acquisition system is introduced in section 3.6. Finally, the NA49 reconstruction, simulation and analysis software is described in the section 3.7.

3.1 Beams and beam counters

The H2 beam line is located in north experimental area of the SPS where the NA49/NA61 detector facility is installed. The experiment is uses beams from the CERN SPS, a circular accelerator with circumference of 6.9 km. The beam is produced by a chain of accelerators. First ions are produced by Electron Cyclotron Resonance (ECR) source. The Pb ions are pre-accelerated in Radio Frequency Quadrupole (RFQ) and Linear Accelerator (LINAC). Ions are striped from the electrons and they are injected to the Proton Synchrotron Booster (PSB) and then to the Proton Synchrotron (PS) accelerator. Finally, the beam enters into the Super Proton Synchrotron (SPS) and is accelerated to its final energy. The CERN accelerators schematic view is shown in Fig. 3.1. From the SPS the beam is extracted to the H2 beam line. The transverse position of incoming beam particles is measured in the telescope of the beam position detectors located along the beam line (BPD-1/2/3), see Fig. 3.2. The resulting precision of the predicted beam position at the target is about 40 μm for Pb and 170 μm for proton beams. This has to be compared to the beam profile with σ of 0.5 mm and 1.3 mm, respec-

tively [75]. The primary event vertex position is obtained from the extrapolation of the beam projectile trajectory which is measured by the BPD detectors. Additional method to obtain the interaction points is a fit to main vertex position. The distribution of fitted points is delivered by extrapolation the beam of the beam particle measured by the beam position detectors to the target foil (BPD vertex). Both methods give almost the same results so the difference between the BPD and Fitted vertex should equal zero. Together with quartz Cerenkov counter S1, helium-gas Cerenkov counter S2 and S3 detector behind allow to select one specific nucleus. The information about charge is given by the pulse height of the signal in the counters S1 or S2.

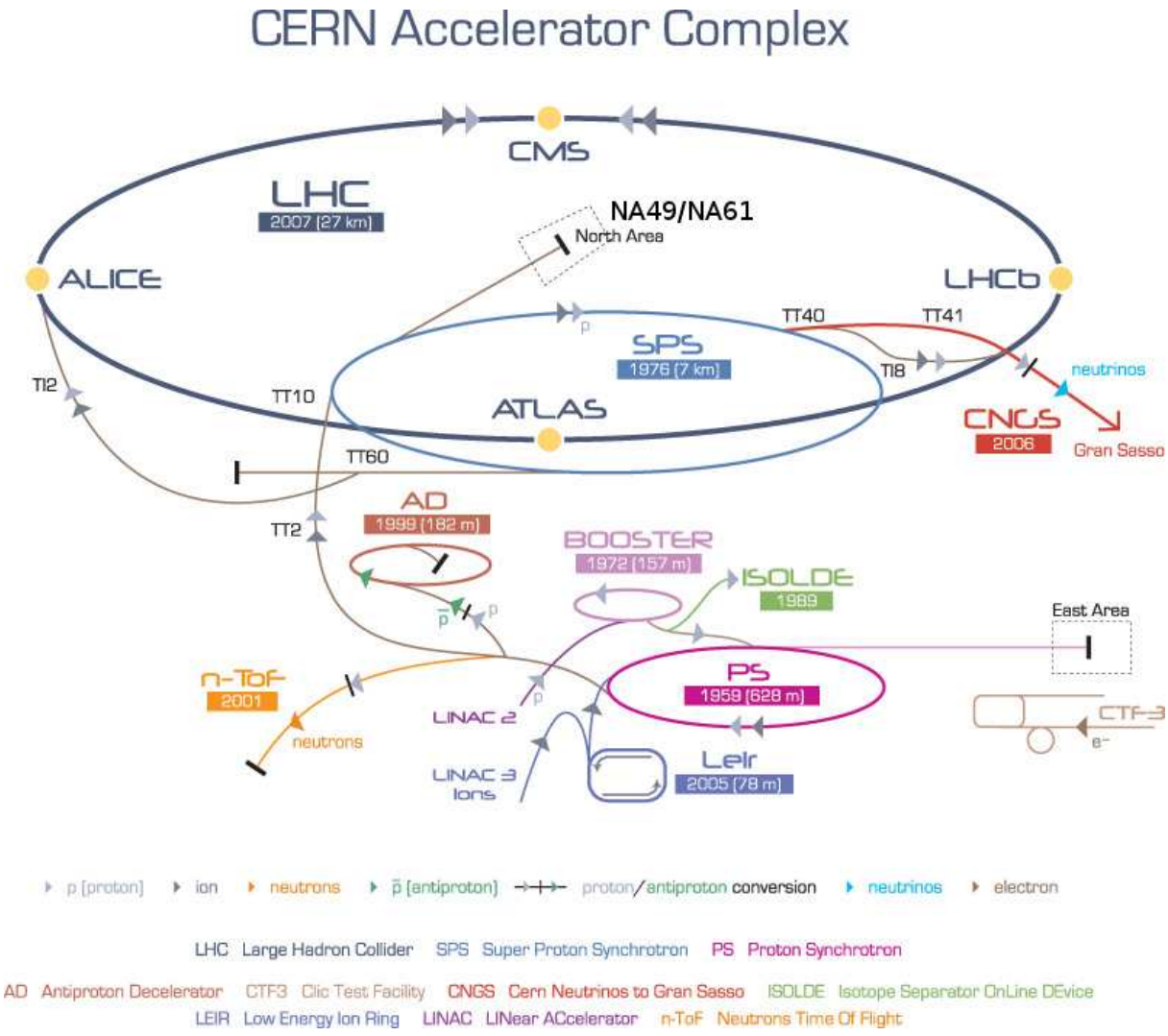

Figure 3.1: Overview of the CERN accelerators. Figure taken from [76].

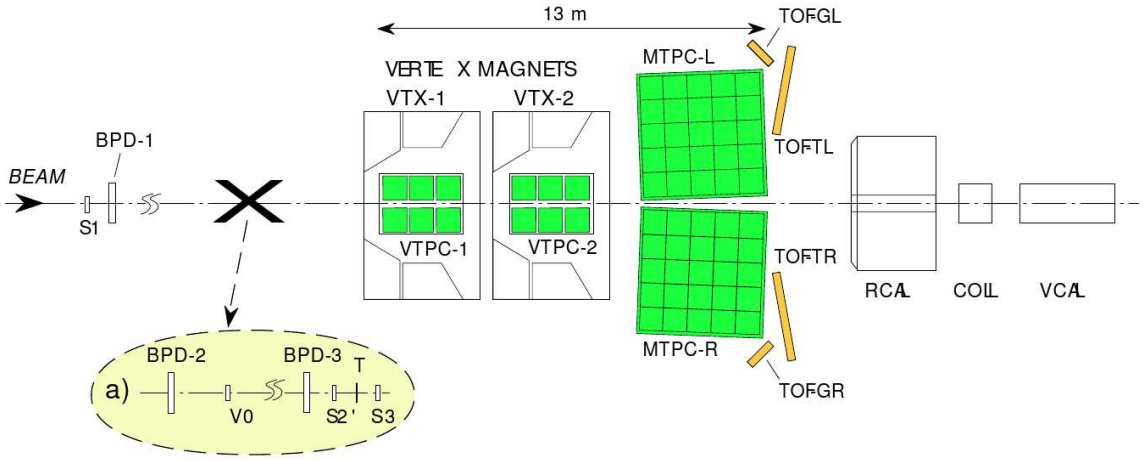

Figure 3.2: Setup of the NA49 experiment with beam definition and target arrangement for Pb+Pb collisions. The target position is at front face of the first Vertex Magnet. Figure taken from [75].

3.2 Experimental setup

The NA49 experiment was designed to measure charged hadrons produced in elementary (p+p) and heavy ion collisions with a large acceptance, good momentum resolution, and good two-track resolution. The NA49 is a fixed-target experiment constructed to register high-multiplicity particles produced in central lead-lead interactions. Different target configurations are available for the NA49 (lead Pb 224 mg/cm^2 foil, carbon C 561 mg/cm^2, silicon Si 1170 mg/cm^2 disks, and liquid hydrogen cylinder). Main components of the experiment are four large volume time projection chambers TPCs. They are able to register a large number of particle tracks, for instance 1500 charged particle in central Pb+Pb interaction at the top SPS energy. Two of the TPC detectors (VTPC-1,VTPC-2) are installed inside the dipole of the superconducting magnets (VTX-1, VTX-2).

Operation of the TPCs in a magnetic field requires either a homogeneous magnetic field precisely aligned with the drift field, or precise knowledge of magnitude and orientation of the magnetic field. For $158A$ GeV the magnetic field of the first magnet (VTX-1) was set to 1.5 T and the second magnet (VTX-2) had the field reduced to 1.1 T [77]. The magnetic field was calculated with the TOSCA software. The magnetic field B deflects tracks of charged particles. In case of the uniform field the momentum of a particle is determined by following formula:

$$p = q \cdot B \cdot R \cdot \frac{1}{cos\lambda}, \tag{3.1}$$

where q [e] is the charge of a particle, R [m] the radius of curvature of the track, and the λ is an angle of track in y direction.

Downstream of the magnets the two main TPCs are installed (MTPC-L, MTPC-R). Similarity to VTPCs they allow for particle identification by the energy loss dE/dx measurement. For MTPC resolution is about 5%. The dE/dx particle identification is complemented by a measurement of the time-of-flight, with a resolution of about 60 ps, in two TOF detector arrays positioned downstream of the MTPCs. The start signal for the TOF detectors is measured by the Quartz Cerenkov counter S1. The mass of a particle is related to its momentum (measured by the TPCs) and its time-of-flight (measured by the TOF detectors). The relativistic relation gives opportunity to determine

$$pc = \gamma\beta m_0 c^2, \tag{3.2}$$

where $\gamma = 1/\sqrt{1-\beta^2}$ and $\beta = v/c$ and

$$(m_0 c^2)^2 = (pc)^2 \cdot \left(\frac{c^2 t^2}{s^2} - 1\right). \tag{3.3}$$

Another sub-detector of the NA49 facility is the Veto calorimeter which was designed to determine centrality of collisions by measuring the energy of the projectile spectators (protons, neutrons and nuclear fragments). The Veto-Calorimeter is located 20 meters behind the target for $158A$ GeV. A typical threshold setting at $E_{veto} \leqslant 8$ TeV results in a selection of about 4% of the most central Pb+Pb collisions with an impact parameter below 3 fm [75, 28, 78]. Experimental setup contains also the BPD-1, BPD-2, BPD-3 beam position detectors and the S1, S2, S3, S4 scintillator detectors used for the beam position measurements and triggering. Fig. 3.3 shows a schematic view of the NA49 experiment with indicated sub-detectors. The experimental setup is described below in more detail. A full description of the NA49 detector can be found in Ref. [75].

The origin of the NA49 coordinate system is located in the middle of the VTX-2 magnet. The z axis is oriented along beam line, the y axis goes to the top and x axis is horizontal and oriented towards Jura Mountains (Fig. 3.4).

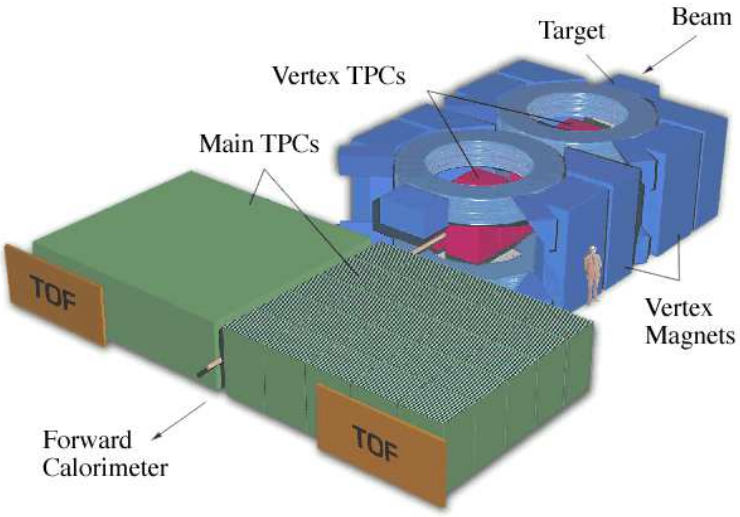

Figure 3.3: Schematic view of the NA49 experiment. The sub-detectors are indicated in the plat: the super-conducting magnets around the vertex TPCs, main TPCs and TOF detectors. Figure taken from [27].

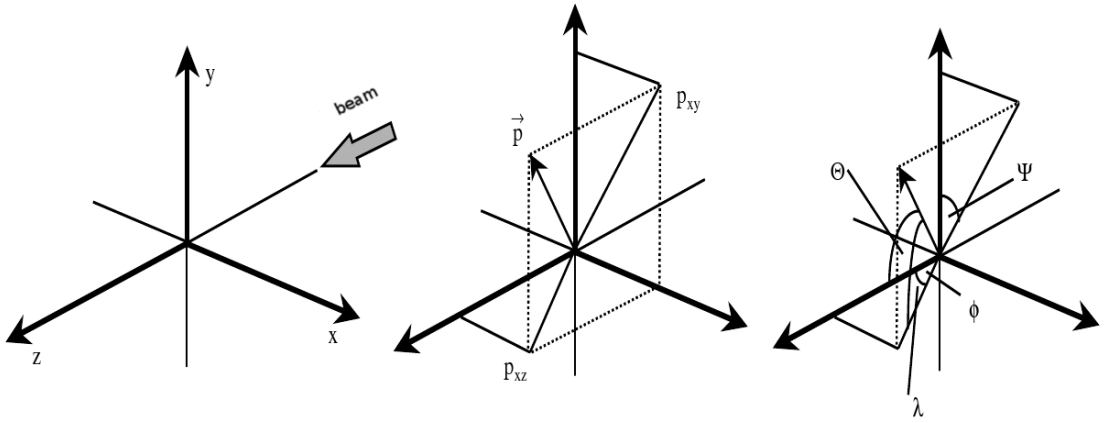

Figure 3.4: The NA49 coordinate system and definition of the used kinematic variables. $\vec{p}$ (momentum vector), θ (polar angle), ϕ (azimuthal angle). Figure taken from [79].

3.3 Tracking system: Time Projection Chambers

Tracking system of the NA49 experiment consists of four Time Projection Chambers (TPCs) which can record three dimensional trajectories and the energy loss of charged particles. In the case of NA49, these are boxes filled with a gas in the electric field (Fig. 3.5). Top planes of the TPC detectors contain readout chambers and electronics. Charged particles ionize gas atoms along their tracks. Under the influence of electric field, free electrons drift to the top plane of detector. The readout chambers contain three wire planes and a pad plane (Fig. 3.6).

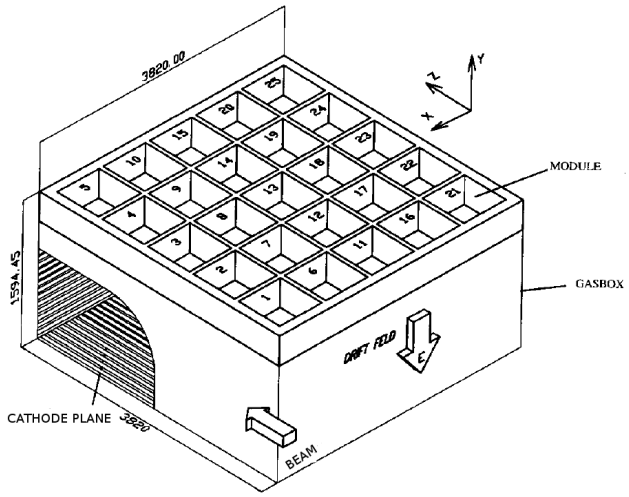

Figure 3.5: Design of the Main TPC (MTPC). Figure taken from [75].

After passing the gating grid, the electrons are suddenly accelerated in the direction of the sense wires until they have sufficient energy for secondary ionization. The original number of drifting electrons is proportional to the amount of electrons originated in secondary ionization. The cathode plane separates the drift volume from the amplification volume. The total charge of secondary electrons is deposited on the sense wires.

Furthermore, electron-ion pairs and photons are produced. They cause a noise by additional ionization with spark discharges. Charge deposited on the sense wires induces charge on several pads (a cluster) of the pad plane which allows to determine the horizontal coordinates of the primary ionization. The vertical coordinate is determined from the measured drift time and known drift velocity. The distribution of clusters is shown in Fig. 3.7 for the main TPC detector (MTPC-R). The accuracy of the coordinate reconstruction is about 0.3 mm. The large particle multiplicities encountered in heavy ion collisions lead to extreme track densities of up to 0.6 particles per cm^2 in the plane orthogonal to the beam direction [75].

The pad geometry is optimized to obtain a good momentum resolution and a good two track

resolution. The energy loss of the charged particles is determined by integrating charge on its clusters. This allows to distinguish between protons, kaons, pions and electrons.

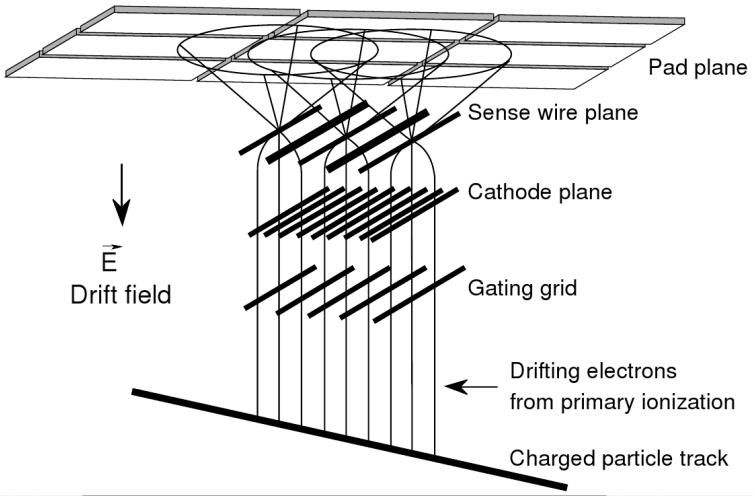

Figure 3.6: Schematic layout and operation of TPC readout chamber. Figure taken from [75].

The two vertex TPCs (VTPCs) are located inside the magnets covering 2 m $\times$ 2.5 m plane with a drift length of 0.67 m. Between the VTPCs there is a gap of 20 cm. The two larger main TPCs are installed outside of magnetic field and have a drift length of 1.12 m and plane of 3.9 m $\times$ 3.9 m. The MTPCs are also split into two equal halves located on both sides of the beam line. The gas mixtures are chosen to reduce diffusion and noise. For the VTPCs a gas mixture of Ne/CO_2 $(90/10)$ and for the MTPCs of Ar/CH_4/CO_2 $(90/5/5)$. Diffusion coefficients have been measured to be 220 μm$/\sqrt{\text{cm}}$ and 270 μm$/\sqrt{\text{cm}}$ respectively, for the two gases, in both transverse and longitudinal direction. Drift fields of 200 V/cm (175 V/cm) correspond to drift velocities of 1.4 cm/μs (2.4 cm/μs) in the two types of detectors. The characteristic properties of NA49 TPCs are summarized in Table 3.1.

The TPC readout system records signals from 182000 pads. Each front-end card reads 32 pads and contains two pre-amplifiers, analog memories and analog-digital converter (ADC). The front-end cards work with 50 μs cycle which represents 512 time bins.

The 8 bit channel of ADC card stored charges and transferred with a frequency of 100 kHz [75]. The total number of front-end cards is 5688. The digitalized information is transferred to Control and Transfer boards (CT) which are also located on the TPC support plates. Each CT-board receives the data from 24 front-end cards. The TPC readout system contains 237 CT-boards. The data are sent to the counting room using the optical fiber links with the speed of 62.5 MHz. The 768 electronic channels are multiplex in a single fibre. Storage and digital data processing tasks including pedestal calculation, zero suppression, noise rejection and event buffering are

performed by receiver boards (3072 channels per boards) mounted in a VME crate system. All these tasks are managed by a VME computer using Motorola DSP 96000 processors. In this stage the data volume is compressed to less than 10% of its raw volume. The raw events contain 8 MB data for central Pb+Pb collisions at 158A GeV.

	VTPC-1	VTPC-2	MTPC
Ne	90%	90%	0%
Ar	0%	0%	90%
CO_2	10%	10%	5%
CH_4	0%	0%	5%
length	2.5 m	2.5 m	3.9 m
width	2 m	2 m	3.9 m
height	0.98 m	0.98 m	1.8 m
drift length	0.67 m	0.66 m	1.12 m
sectors	6 (2×6)	6 (2×6)	25 (5×5)
pads	27648	27648	63360
pad rows per sector	24	24	18
pads per row	192	192	192/128
pad length	16/28 mm	28 mm	40 mm
pad width	3.5 mm	3.5 mm	3.6/5.5 mm
pad angles	12°-55°	3°-20°	0°-15°

Table 3.1: Physical properties of NA49 TPCs [75].

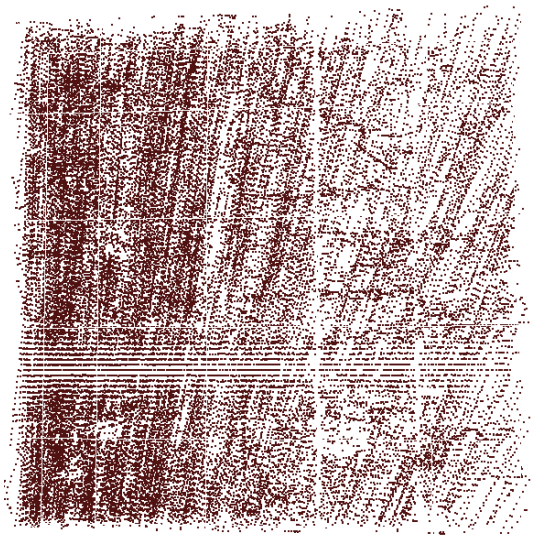

Figure 3.7: Cluster of particle tracks in MTPC1. Figure taken from [27].

3.4 Time of flight detectors

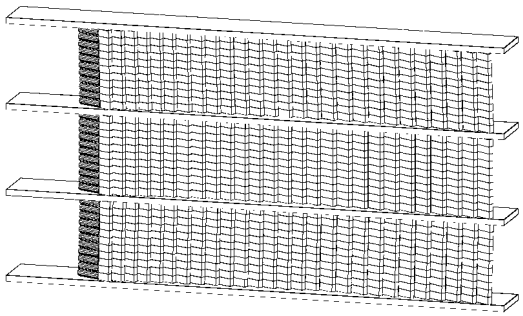

Figure 3.8: The pixel-scintillator wall (TOF-TR/TL) as a part of TOF detector systems [80].

The NA49 Time-Of-Flight detectors (TOF) are scintillator detectors which measure a particle time of flight from the interaction point to the TOF detector. The TOF detectors are associated with trigger detector system. The NA49 experiment contains four Time Of Flight walls. Two pixel-scintillator walls (TOF-TL/TR) of 4.4 m^2 total surface work with time resolution of 60 ps (Fig. 3.8). The pixel detectors TOF-TR/TL contain 1782 individual scintillation counters.

To determine a mass of particle using the TOFs detector, the momentum measurement is necessary. The momentum of the particle is known by tracking particle curvature in the magnetic field. The Time-of-Flight and dE/dx measurements allow identification of particles in most efficient way. Performing two dimensional histograms of the energy loss and mass measurements increases separation between different sorts of particles and thus improves precision of the particle identification (Fig. 3.9). Unfortunately, the TOF detectors have a limited acceptance and therefore are not helpful for the analysis performed in this work.

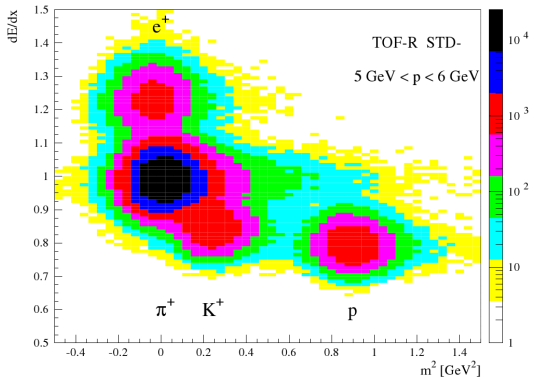

Figure 3.9: Particle identification with dE/dx and time-of-flight. Data for central Pb+Pb collisions with total momentum interval chosen as $5 < p < 6$. Figure taken from [81].

3.5 Centrality measurement

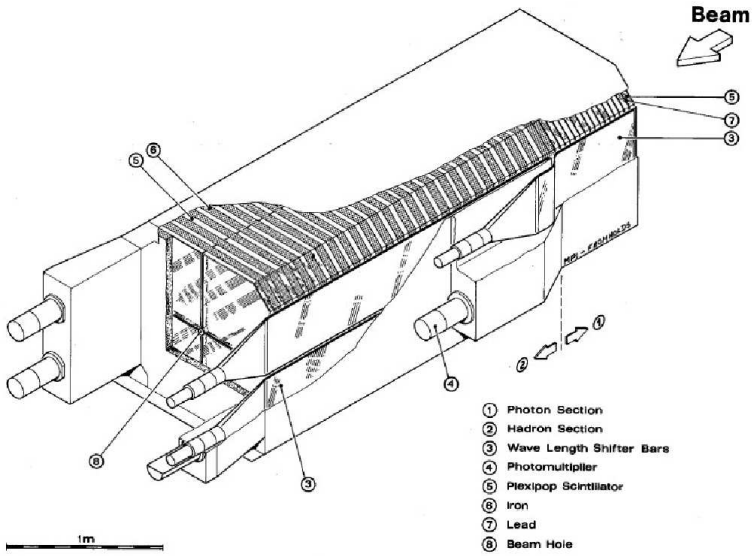

Figure 3.10: The Veto calorimeter. Figure taken from [82].

The collisions centrality is determined by measurement of the energy deposited by spectators in the Veto calorimeter. The Veto detector contains an electromagnetic section of lead scintillator layers of 16 radiation lengths which is followed by a hadron section of the iron scintillator layers of 7.5 interaction lengths. The Veto calorimeter is composed by four segments of electromagnetic part in the front and a hadronic part in the back (see Fig. 3.10). The light conductors located on the left and right sides of the calorimeter transport the light produced in each segment to photo-multipliers. Readout is provided by 8 photomultipliers for each section. The calorimeter is located 20 m behind the target to avoid possible hitting of participants and produced particles. All projectile spectator protons, neutrons and nuclear fragments reach the Veto calorimeter [83, 84] .

3.6 Data acquisition

Flow and order of data is managed by the NA49 data acquisition system. Data of an event (100 MB) are transferred from the front-end electronics to 60 receiver boards by fibre optical links. The receiver boards are installed in 6 VME crates with 9U bus slots. The receiver boards buffer data which can hold 32 raw events. A digital signal processor DSP processes buffered data and applies zero suppression algorithm. Until data is transferred from TPC front-end electronics, the buffered data are not accessible for the DSP. Storing data is controlled by a master

processor based on the Motorola 68040 CPU with master/slave and VSB/master interfaces. Reading the event fragment is done by directly access to the local memory of the master CPU installed in the master VME crate which steers all the data acquisition. Finally, complete events are assembled by the master VME CPU processors. Raw events are transferred to a SONY DIR-1000M 19 mm tape recorder which can operate at a transfer rate up to 16 MB$/$s. The drive of the type operates in streaming mode. About 100 minutes of uninterrupted recording correspond to 10000 events on tape which has capacity of 100 GB. All the VME processors run under the OS9/68000 operating system. The standalone UNIX machines are responsible for booting and file hosting over the network VME computer card. The system takes approximately 85 ms to assemble a single event and transfer to the tape controller [75]. The data taking mode was changed in year 2000. The events were sampled by 256 time bins instead of 512 in the standard mode. Smaller size of the raw events allows to configure the receiver boards to keep 64 raw events. A compression algorithm was optimized into DSPs, reducing the event size from 8 MB to 3 MB [85]. These allowed to increase the data taking speed to about 44 events per spill.

3.7 Reconstruction, simulation and analysis software

The process of measuring and reconstructing charged particles produced in collisions of nuclei in the experiment NA49 is a complex procedure. It can be divided into four basic stages.

- Storing measured data by sub-detectors ("on-line"). This stage is performed during a data taking period. Raw events are stored and are managed by the data acquisition (DAQ) system.
- Reconstruction of the stored data ("off-line"). In order to extract physical information the raw events have to be processed to obtain information necessary for physics analysis like particle momenta, charges and masses.
- Physical analysis of the reconstructed data ("off-line"). Analysis is done using as an input the reconstructed data.
- Monte Carlo simulations which allow to correct the results for the experimental effects such as a limited detector acceptance and efficiency.

3.7.1 Reconstruction of raw data

The process of the reconstruction can be divided into three stages:

- Cluster finding
- Track and vertex finding
- Track and vertex fitting

A typical reconstructed event is shown in Fig. 3.11.

Reconstruction of raw events is done by the NA49 software. The reconstruction software contains many small programs, which form a complex reconstruction system the so-called reconstruction chain. Such a design is characteristic for UNIX-like software. The programs perform: cluster finding, track finding, positioning of primary and secondary vertices, dE/dx and time-of-flight (TOF) determination and a lot of other tasks. At first, the data on magnetic field and detector geometry are given in the configuration files, which are the parameters for the programs of the reconstruction chain. Data events are delivered by a DSPACK server which is started during the reconstruction. DSPACK is a structural client-server data manager system which provides a technique of passing data between the programs [86]. DSPACK operates on raw data files and writes reconstructed events into output Data Summary Tape (DST) files. Thus all programs have a multiple IO access to the raw data files and DST files during the reconstruction. The results of the reconstruction are stored into `DSTs`. In order to reduce the amount of stored information the `DSTs` are converted to `miniDSTs`. The `miniDST` files are written using ROOT [87] format files. This operation is done after reconstruction.

Cluster finding

The program `dipt` is responsible for cluster finding. It looks for connected area in pad row of the TPCs when the ADC value is above the threshold value. The center of charge distribution determines a position of the cluster. The coordinates in x-z plane are calculated from the pad positions, whereas the y-coordinated is calculated using the drift time. High track density may result in overlap of track clusters. In order to recognize the overlapping clusters special criteria on the distance between two maxima are set up. The force on the drifting electrons is not completely vertical and this leads to deflection from an ideal vertical trajectory. This is important at edges of the VTPCs where the magnetic field is not homogeneous and close to the sense-wires

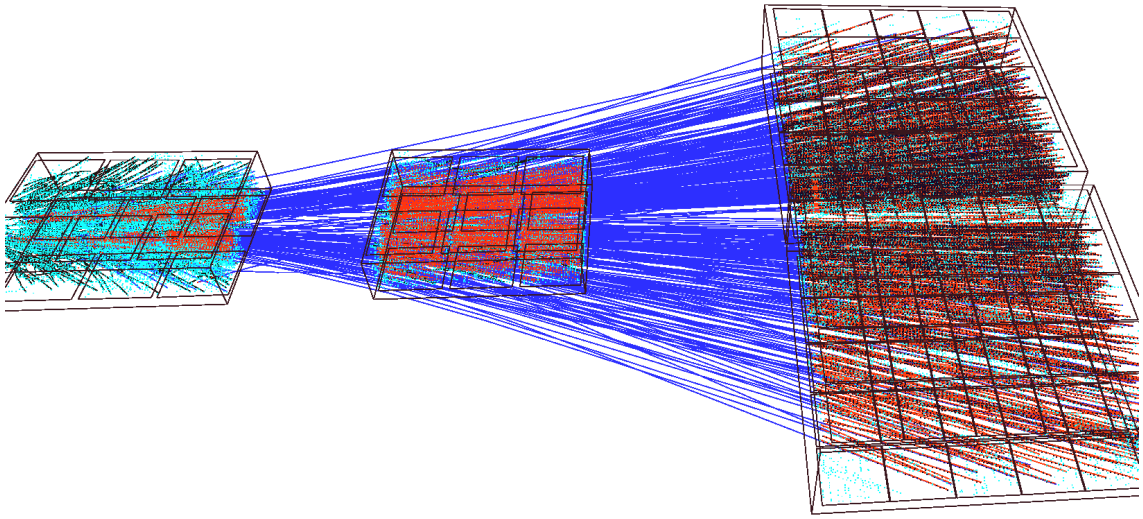

Figure 3.11: Visualisation of three dimensional tracks a reconstructed for central Pb+Pb collision. The tracks are interpolated between TPCs detectors by reconstruction software [27].

where the electric field is not uniform [88]. These distortions are corrected by the `edisto`, and `vt_ncalc` clients. [89]. The remaining deviations of the reconstructed track trajectories from ideal ones are corrected by the residual correction `tpc_rescorb` client.

Track finding

Track finder begins to find particle traces from the most distant points measured from the vertex with an additional criterion of track pointing to the main vertex.

First stage of tracking is done in each TPC detector separately. It starts from tracking in MTPCs which is done by the `mtrack` client. Tracks in MTPCs are straight lines, which simplifies the tracking. The VTPCs are close to the vertex and placed in the magnetic field, thus the track density is high and the trajectories are curved. Therefore, finding tracks in this case is more difficult. Thus a complex track model of a distorted helix is used. The program predicts a track trajectory in VTPC by extrapolating the MTPC track. This procedure facilitates reconstruction of tracks' part in VTPC2 by `patrec` client. In order to match each track, the reconstructed VTPC2 tracks are extrapolated to the MTPC by the `mpat` program. Reconstructed tracks in VTPC2 and MTPC are extrapolated to VTPC1 by `mpat`.

Track and vertex fitting

In order to determine momentum all track trajectories are fitted to the main vertex or to the secondary vertices .

The `r3d` program is responsible for the momentum determination. It is tracing the particles in the magnetic field. The momentum resolution is of order of $dp/p^2 \approx 10^{-4}$ $[(\mathrm{GeV}/c)^{-1}]$. By a backward track extrapolation the main vertex position is determined by the (`vtx`) client.

Using the fitted trajectory the number of potential points is calculated according to detectors' geometry by the `ppoints` client. The merging of track segments is done by the `domerge` client.

After these procedures the reconstruction software searches for tracks which do not originate from the main vertex. The reconstruction chain program recognises the secondary vertices which are produced mainly by weakly decaying particles ($\Lambda_s, \Xi_s, \Omega_s$ and K^0_s). The clients `v0find`,`v0fit`, and `xi_find` are used in this procedure.

Finally the information on a particle flight time is reconstructed by `tof_client`, `tofr_client` and `tofg_client`. In the last stage of reconstruction the energy loss dE/dx is determined by `gen_dedx` client. The clients' scheme of reconstruction chain from raw data to the reconstructed event is illustrated in Fig. 3.12.

3.7.2 Simulation

The simulation is necessary to correct the data for effects related to imperfectness of the detector.

The simulation input can be taken from Monte Carlo events generators such as Venus and UrQMD models. The initial momentum vectors are delivered in ASCII file format to the GEANT detector simulation package. The GEANT software tracks particles through the materials of the detector in the magnetic fields. The GEANT software adopted to the NA49 experiment is called GNA49. In the simulation and the reconstruction chains the same detector geometry and magnetic field maps are used. The tracks from GEANT must be distorted by TPC simulation program so-called MTSIM. This program takes Monte-Carlo points of a track and produces digitalized data based on the properties of the TPC gas and the readout electronics. The signal is prepared in the same format as raw data events delivered from data acquisition system (DAQ) with the threshold cuts and compression algorithm. In the case of the embedding simulation the simulated raw data are added to the raw data of a real event. The real events

Figure 3.12: The NA49 reconstruction chain. Figure taken from [28].

are delivered by GTEMBED. The process of track embedding requires adding ADC signals in each pad-timeslice pixel from the both data sets. Such prepared raw data events are processed through the reconstruction chain in the same way as for real data reconstruction. In order to compare reconstructed tracks to the simulated tracks the GTEVAL tool is used. It matches TPC points with the track MC points. Simulated MC tracks and their reconstructed tracks are compared. Number of matched points is used to select reconstructed track candidates for matched MC tracks. The output of the simulation chain is written in DSPACK file, which can be converted to ROOT [87] `miniDST` format [27]. The schemats of the simulation chain is shown in Fig. 3.13.

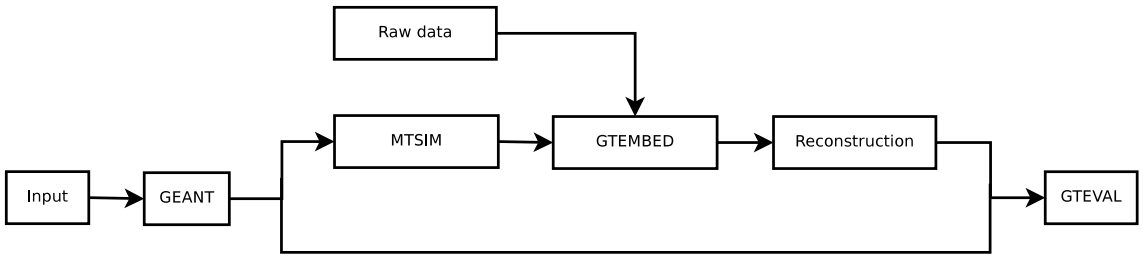

Figure 3.13: Simulation chain software of the NA49 experiment.

3.7.3 Analysis software

The analysis of reconstructed events is based on the software in ROOT environment. The ROOT, is an object oriented data analysis framework with numerous packages and tools. The ROOT environment has the C++ interpreter so-called CINT which allows to write ROOT macros in C++ language style and interactively compile and processes them. Originally the ROOT project started within the NA49 experiment. The NA49 experiment has an ideal environment to develop the next generation of data analysis tools [87]. Nowadays, many experiments and projects related to high energy physics (HEP), heavy ion physics, and also other research fields use this software.

The NA49 experiment has a special ROOT extender called ROOT49 which contains two libraries `T49DST`, `T49ANA` dedicated to the experiment. The NA49 libraries are called T49 analysis framework. The T49 libraries support the `miniDSTs` format that is based on ROOT file. The `miniDSTs` event format is reduced and compressed to analyze the reconstructed events in the frame of the smaller amount of data. The ROOT49 allows also direct access to NA49 data in DSPACK format using `TRootDS` class.

Chapter 4

Specific energy loss in the TPC gas

In this work the specific energy loss in the TPC gas is used to select suitable candidate of particles (K,π). reduce the background of unwanted particles. Therefore, in this chapter a basic information concerning the specific energy loss and its role in the particle identification is discussed.

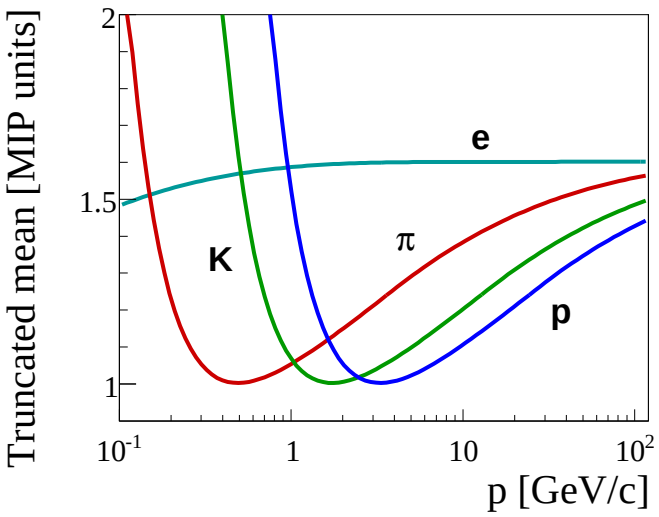

Figure 4.1: Bethe-Bloch function for different particles.

4.1 Ionization energy loss

A charged particle traversing the active volume of the TPC detectors ionizes the chamber gas by Coulomb interactions with the electrons of the gas molecules. The magnitude ionisation depends on gas which was used in the TPCs of NA49. The specific ionization of particles is

obtained from the measurements of the charges of clusters on tracks. The Bethe-Bloch formula [90, 91] describes the relation between particle momentum and mean energy loss as presented in Fig. 4.1 for several particle types. It is seen that the mean energy loss depends on the particle mass. Thus, a simultaneous measurements of the specific energy loss and momentum allows a particle identification. For example, selecting particles within a band around a selected Bethe-Bloch curve allows to enhance a contribution of a given particle type within the selected particle sample. The Bethe-Bloch formula is given by:

$$\left\langle -\frac{dE}{dx} \right\rangle = \frac{4\pi N e^4}{m_e \beta^2} \left(\ln \frac{2 m_e \beta^2}{I(1-\beta^2)} - \beta^2 - \delta(\beta) \right), \tag{4.1}$$

where $\langle dE/dx \rangle$ is the mean specific energy loss, $\beta = v/c$ is the particle velocity, e is the charge of the electron, m_e its mass, N is the density number of the electrons in gas of detector and I the average potential excitation [85]. The reduction of ionisation at large velocities, due to coherent polarization of the surrounding atoms which shields the field of the traversing particle, is parametrized by the function δ [85].

$$\delta = \begin{cases} 0 & \text{if} \quad \beta\gamma < a_1 \\ 2(\ln \beta\gamma - b) + c(\ln a_2 - \ln \beta\gamma)^d & \text{if} \quad a_1 < \beta\gamma < a_2 \\ 2(\ln \beta\gamma - b) & \text{if} \quad \beta\gamma > a_2 \end{cases} \tag{4.2}$$

Parameters b, c, and d in equation 4.2 are tabulated for many materials, but are fitted to data in the case of parametrization used by the NA49 [92, 93]. The values of a_1 and a_2 are calculated so as to make δ as continuous function of β [].

4.2 The $\langle dE/dx \rangle$ measurements

The $\langle dE/dx \rangle$ measurements are based on the measurements of the total charge which is deposited on each cluster on a track registered in TPC. The cluster charge, follows an asymmetric Landau distribution:

$$p(x) = \frac{1}{\pi} \int_0^\infty \exp\left(-t \log t - xt\right) \sin(\pi t) dt. \tag{4.3}$$

Figure 4.2 in left panel shows the distribution of the cluster charges which has a long tail. This is an intrinsic property of the ionisation process. If the particle track measured in the

TPCs is long enough then many clusters are measured and the energy loss distribution becomes similar to Gaussian (right panel of Fig. 4.2). For the tracks with small number of clusters the most probable energy loss is significantly lower than the mean energy loss. In order to reduce statistical fluctuations of the mean value the fixed percentage of the smallest and the highest energy loss measurements are rejected. From the clusters selected by this produced the mean is calculated which is called the truncated mean. Its distribution is approximately Gaussian for tracks which have at least 30 clusters. For tracks with lower number of clusters the distribution is significantly asymmetric. For p+p, C+C and Si+Si systems in the NA49, the best results

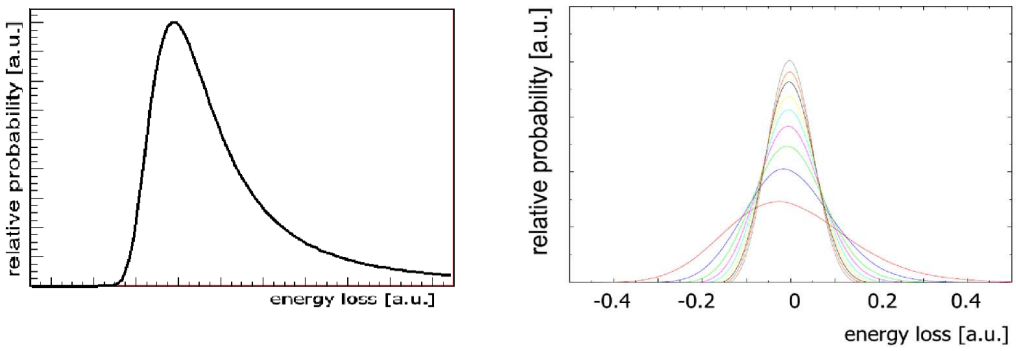

Figure 4.2: Left: Outlook view of Landau distribution of the energy loss of a charged particle. Right: Truncated mean distribution of Main and Vertex TPC tracks with different number of clusters $(10, 20, ..., 90)$. Figure taken from [94, 95].

are obtained by cutting off upper 50% of the clusters and for Pb+Pb the upper 35% [96]. The resulting resolution of the truncated mean σ_{abs} depends on the type of material (α) and the total number of clusters (N_{points}) [96]:

$$\sigma_{abs} = \frac{C}{\sqrt{N_{point}}} \left(\frac{dE}{dx}\right)^{\alpha}, \tag{4.4}$$

where α is about 0.5 for the VTPCs and about 0.7 for the MTPCs, and for the combined energy loss measurements from all TPCs it is about 0.625. The parameter C is about 0.4 resulting for example in a relative sigma about 4% for a typical track length of 100 points and a dE/dx (normalized to minimum ionization) of 1.2 [96]. A distribution of the truncated mean of a given particle is parametrized by an asymmetric Gaussian:

$$f(x; C, x_0, \sigma, \delta) = \frac{C}{\sigma\sqrt{2\pi}} \exp\left[-\frac{1}{2}\left(\frac{x - x_0}{(1 \pm \delta)\sigma}\right)^2\right]. \tag{4.5}$$

The asymmetry parameter δ determines the difference between the width of left and right halves of the Gaussian.

In order to improve the resolution of the track-by-track measurements of the specific energy loss the measurements from different TPCs are combined to a single dE/dx value for each track. The main TPCs and vertex TPCs have different gas-compositions and the read-out properties thus the energy loss measurements are different. The VTPC dE/dx measurements are scaled to the MTPC dE/dx, using the ratio of the parametrized dE/dx (equation 4.1) in the Vertex and Main TPCs.

The cluster charges are corrected for many experimental biases. They included drift length dependent charge losses due to electron absorption and effects related with high track density in Pb+Pb collisions [77].

Chapter 5

Data analysis

In this chapter data, selection cuts and analysis methods are described. The used data set is introduced in section 5.1. The event and particle selection criteria are presented in section 5.2. The methods of analysis are explained in section 5.3. The Monte Carlo simulations of K^* and $\bar{K}^*$ signals and their reconstruction are given in section 5.4. The reconstruction efficiency of K^* and $\bar{K}^*$ is presented in section 5.5. Systematic and statistic uncertainties are discussed in section 5.6.

5.1 Data set

This analysis is based on a high statistics data set which contains approximately three million collisions of $158A$ GeV Pb ions in a Pb target of 337 mg/cm^2 (approximately 1.5% interaction probability for Pb ion) recorded by the NA49 experiment in 2000. The trigger selected the 23.5% most central Pb+Pb collisions. The corresponding mean number of wounded nucleons N_w was calculated using the Venus model [97] to be $\langle N_w \rangle = 262 \pm 1$(stat) ± 5(sys) [98]. The data set is reconstructed by the NA49 reconstruction chain version `01I` [1]. The analysis is based on the ROOT `miniDST`. It is summarized in Table 5.1.

System	Beam energy	Magnetic field	σ/σ_{tot} [%]	N_{event}	$\langle N_w \rangle$	version
Pb+Pb	158A GeV	STD+	23.5%	2968504	$262 \pm 1 \pm 5$	00I

Table 5.1: Data set on Pb+Pb collisions used for study of $K^*(892)$ and $\bar{K}^*(892)$ production.

[1] The standard field configuration are called STD+ and STD-; the STD- configuration is field up, and the STD+ configuration has the inverse polarity. STD+ sends negatives into MTPC-R, STD- sends positives into MTPC-R.

5.2 Event and particle selection criteria

The event selection criteria are introduced in order to exclude non-target interactions. The track selection criteria aim to select well reconstructed tracks which originate from target interactions. In the following subsections the event and track cuts are discussed in details.

5.2.1 Event selection

The Beam Position Detectors (BPDs) measure x and y coordinates of a beam nucleus at the z positions of the detectors. This data allow to predict the position of a hypothetical interaction point in the target. In this prediction the surveyed z coordinate of the target is used, $z = -581.4$ cm. The interaction point reconstructed using the BPD data is called the BPD vertex. In addition, the interaction point can be reconstructed by a backward extrapolation of the TPC reconstructed tracks. The interaction point reconstructed using the TPC data is called the FIT(ed) vertex. Proper FIT vertex reconstruction is signalled by the value of FIT vertex $iflag$ equal to zero. Only events with $iflag = 0$ are selected for the analysis. Fig. 5.1 shows distributions of coordinates of the BPD vertex, the FIT vertex and the difference between them. Statistical uncertainties lead to smearing of the difference distributions ($\sigma_x = 0.21$ cm, $\sigma_y = 0.15$ cm, $\sigma_z = 1.3$ cm). Systematic biases (e.g. imperfect residual corrections) can cause shifts of the vertex position. The event selection cuts are as follows:

$$-0.3 < x_{BPD} < 0.3 \quad \text{[cm]},$$

$$-0.3 < y_{BPD} < 0.3 \quad \text{[cm]},$$

and

$$-0.3 < x_{FIT} < 0.3 \quad \text{[cm]},$$

$$-0.3 < y_{FIT} < 0.3 \quad \text{[cm]}.$$

The cut in z coordinate is:

$$-582 < z_{FIT} < -580 \quad \text{[cm]}.$$

Red vertical lines in Fig. 5.1 indicate applied events cuts. Finally, only events with the reconstructed charged track multiplicity in the range are selected:

$$400 < N_{ch} < 1600.$$

Distributions of multiplicity and Veto energy for accepted events are shown in Fig. 5.2. Fig. 5.3 shows the two dimensional histogram illustrates correlation between the energy deposited in Veto calorimeter and the multiplicity of charged particle.

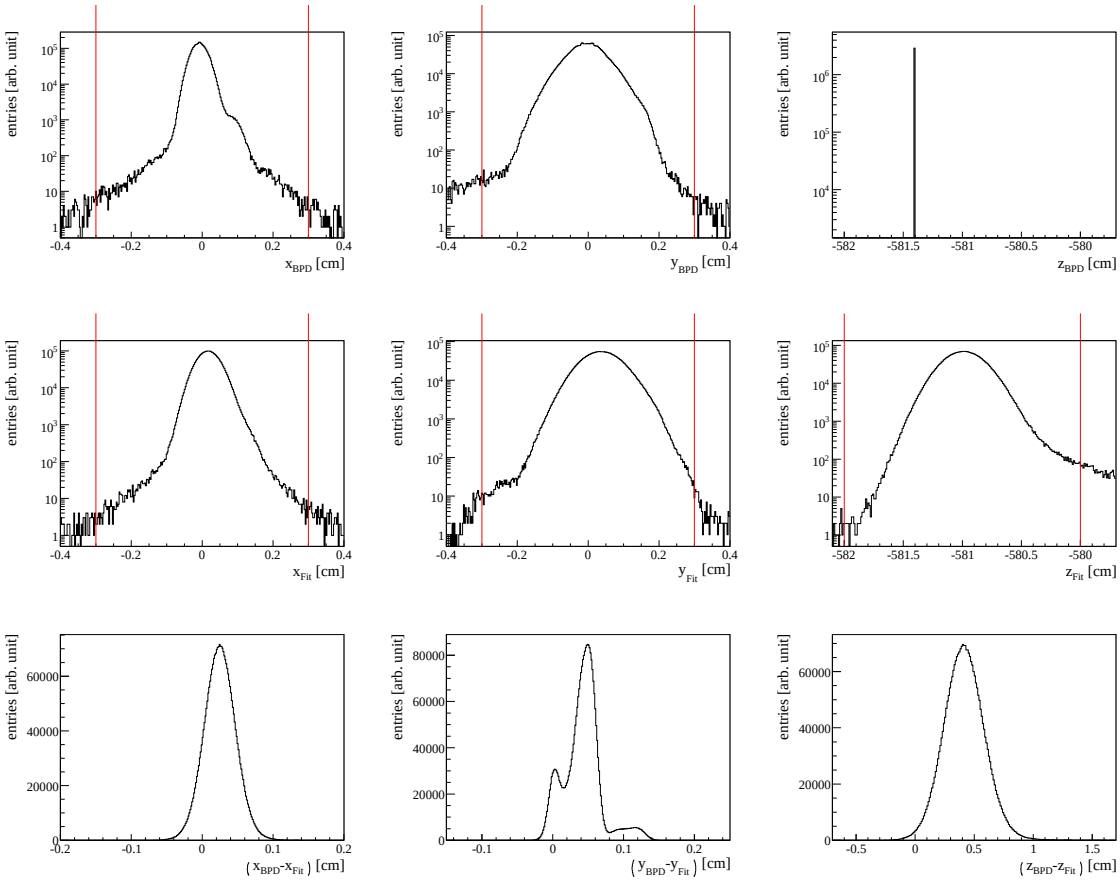

Figure 5.1: The distribution of x, y, z coordinates of the main vertex position (23% central Pb+Pb collisions at 158A GeV). First raw of plots shows distributions coming from the beam position detectors (BPDs). Middle raw of plots shows the vertex fit distributions. Bottom raw of plots shows differences between the vertex of the beam position detectors (BPDs) and the vertex fit ($2.9 \cdot 10^6$ events).

5.2.2 Track selection

Charged particle tracks were reconstructed from the charge clusters left in the TPCs using the global tracking scheme which combines track segments that belong to the same physical particle

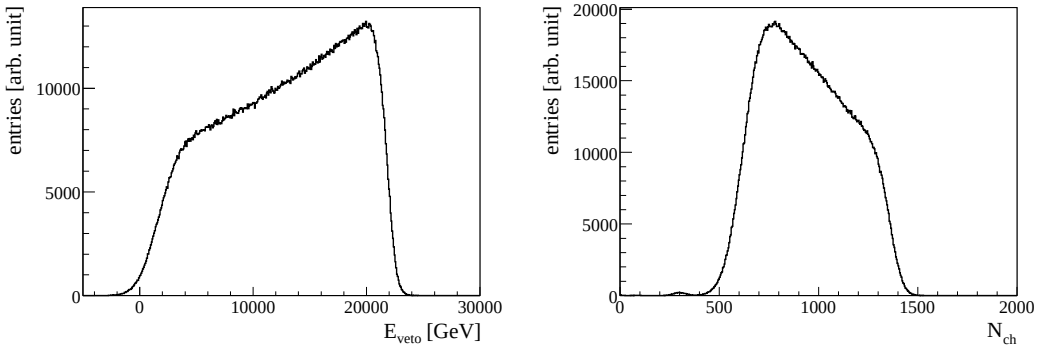

Figure 5.2: Left: veto energy distribution at 158A GeV. Right: multiplicity distribution of charged particles at 158A GeV ($2.9 \cdot 10^6$ events).

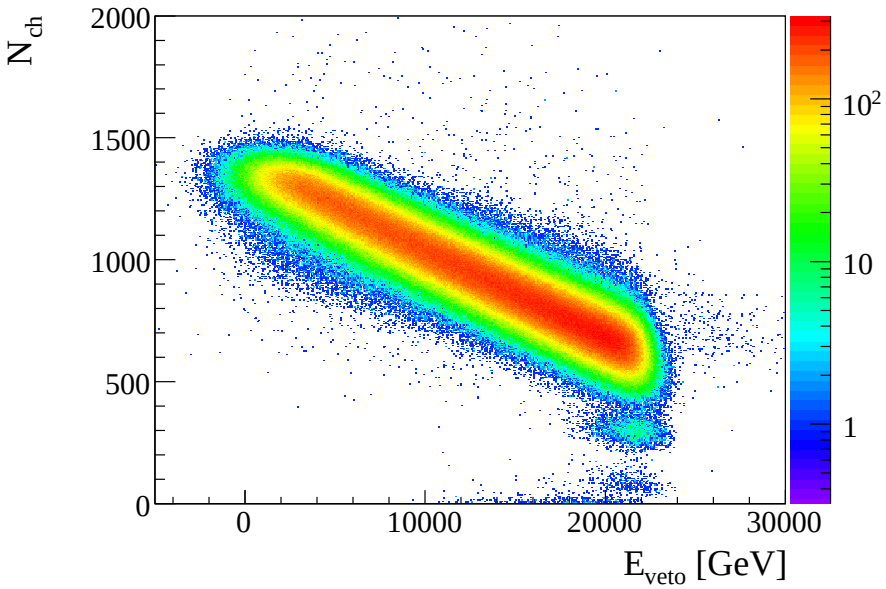

Figure 5.3: Two dimensional distribution of multiplicity versus veto energy of charged particles produced in central Pb+Pb collisions at 158A GeV.

but were detected in different TPCs. In order to select well reconstructed tracks from the target interactions and minimize contribution of non-target tracks (from weak decays, secondary interactions, delta electrons), track selection cuts are applied. During the track selection procedure, the track properties such as the number of points on the track or impact parameter at the target plane are analysed for all tracks. The track impact parameter is defined as a difference between primary vertex position and the track impact point at the target plane calculated by the track backward extrapolation in the magnetic field. In order to remove tracks which do not originate from the primary vertex, the cuts are defined as:

$$-5 < b_x < 5 \quad \text{[cm]},$$

$$-3 < b_y < 3 \quad \text{[cm]},$$

where b_x and b_y are track impact parameters in x and y coordinates respectively. Fig. 5.4 shows track impact parameter distributions. Red lines indicate applied cuts.

Only tracks with the total momentum in the range $3 < p < 100$ GeV/c and more than 25 measured TPC points are selected for this analysis. Furthermore, only tracks with the ratio on the measured points to the maximum possible number of TPC points, calculated for each track, larger than 0.5 are accepted. Fig. 5.5 shows a distribution of the measured TPC points on tracks and the point ratio distribution.

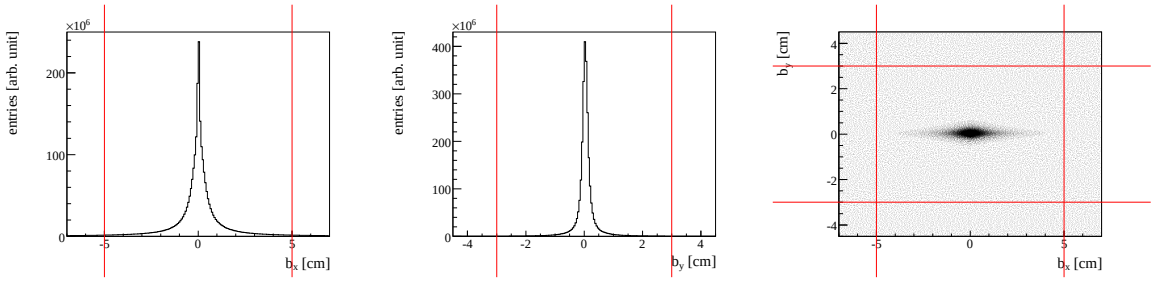

Figure 5.4: Track impact parameter distributions, b_x (left), b_y (middle) and b_x versus b_y (right) for 23% central Pb+Pb collisions at 158A GeV.

5.2.3 dE/dx particle identification cuts

Particle identification is based on measurements of truncated mean energy loss dE/dx in the TPCs which provide up to 234 charge samples on a track. The uncertainty of dE/dx measurement for a specific track depends on its visible length and the number of associated charged

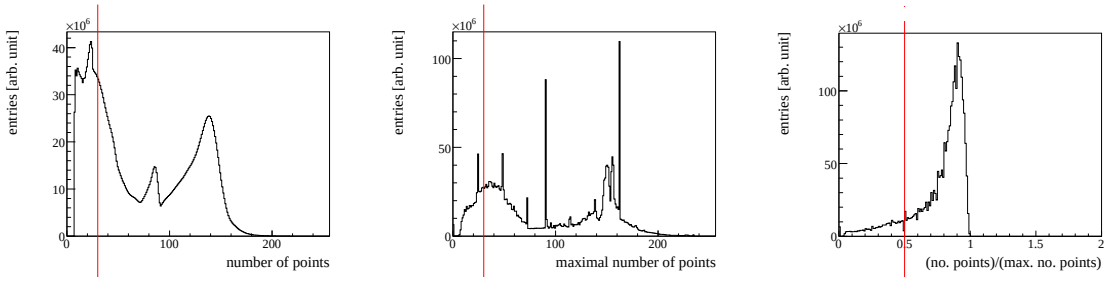

Figure 5.5: Distribution of the number of TPC points (left), maximum number of TPC points (middle) and their ratio (right) for central Pb+Pb collisions at 158A GeV.

clusters. Fig. 5.6 shows two dimensional plots of the specific energy loss in the TPC gas versus total momentum for positively (left) and negatively (right) charged particles. The details of the NA49 procedure on calibration and extraction of the specific energy loss information can be found in reference [96]. In this analysis the measurements of dE/dx was performed using global tracks. The specific energy loss depends on a particle total momentum and mass. As the momentum information can be obtained from track trajectory and the energy loss measurement allows to extract information on the particle mass. The mean energy loss as a function of particle momentum and mass is given by the Bethe-Bloch function [90, 91]. The Bethe-Bloch curves are shown in Fig. 5.7 for different particle species. The width of the specific energy loss distribution at a fixed momentum, as measured by the NA49, is about 5% of the mean value. Particles inside a band of ± 0.125 around the pion mean value have been defined as pion candidates. Particles inside a band of ± 0.15 around the kaon mean value have been defined as kaon candidates. These selections correspond to about 2.5 and 3Δ ($\Delta = 0.05$ MIP[2]) cuts and thus the expected losses of pions and kaons are small ($< 2\%$). Furthermore, it was checked by

[2]Minimum Ionizing Particle.

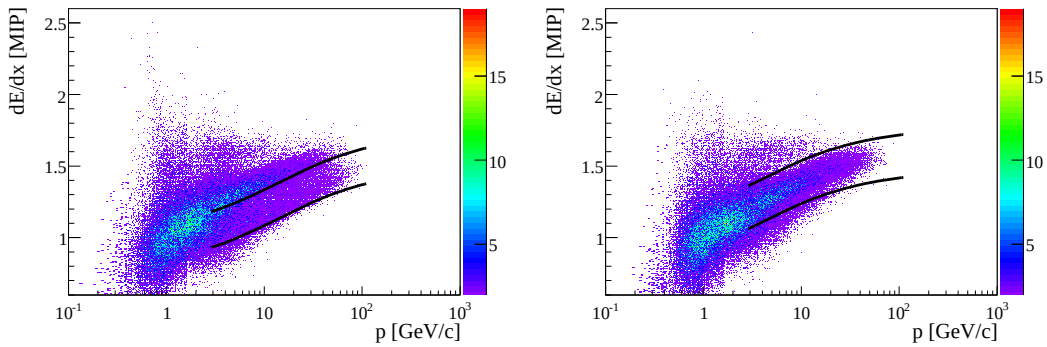

Figure 5.6: The dependence of the mean energy loss on momentum (p) of the particles (500 events from Pb+Pb collision at 158A GeV).

the Gaussian fits to the pion peak that the used Bethe-Bloch parametrization describes the data within 2%. Possible systematic bias is thus smaller than 5%. The black lines in Fig. 5.6 indicate the bands of accepted kaon and pion candidates.

Figs 5.8 and 5.9 presents the kaon (top) and pion (bottom) candidates selected for this analysis.

The dE/dx resolution for the tracks selected for this analysis was checked in the relevant momentum region by the following procedure. Narrow momentum bins in the range $3 < p < 100$ GeV$/c$ were selected. In each bin the Gaussian distribution was fitted to the pion peak. The resulting σ parameter plotted as a function of total momentum is shown in Fig. 5.10. It is about 0.05 in the momentum range where the most of the tracks are located, at the edges of the distribution for tracks with a low number of measured points it is about 0.07.

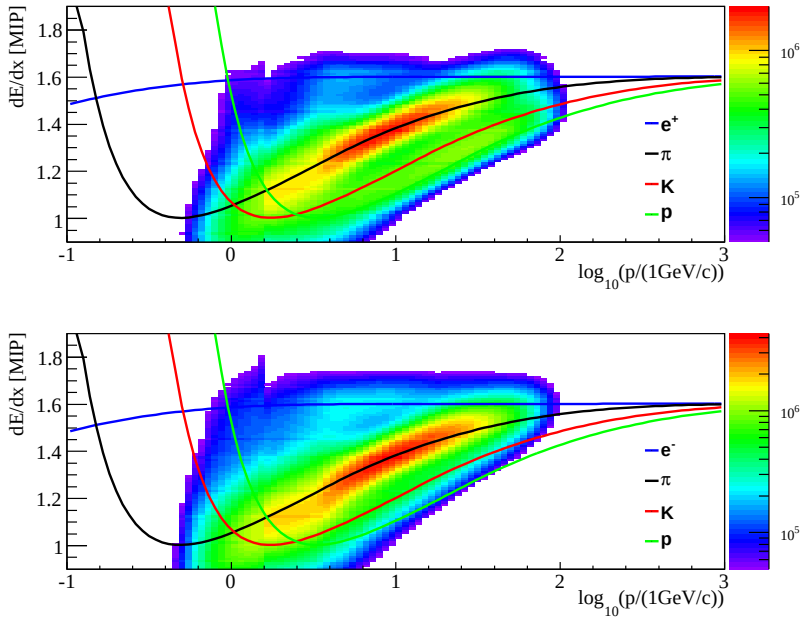

Figure 5.7: Dependence of the mean energy loss on $log_{10}(p)$ of the particle (Full statistic: $2.9 \cdot 10^6$ events from Pb+Pb collision at 158A GeV))

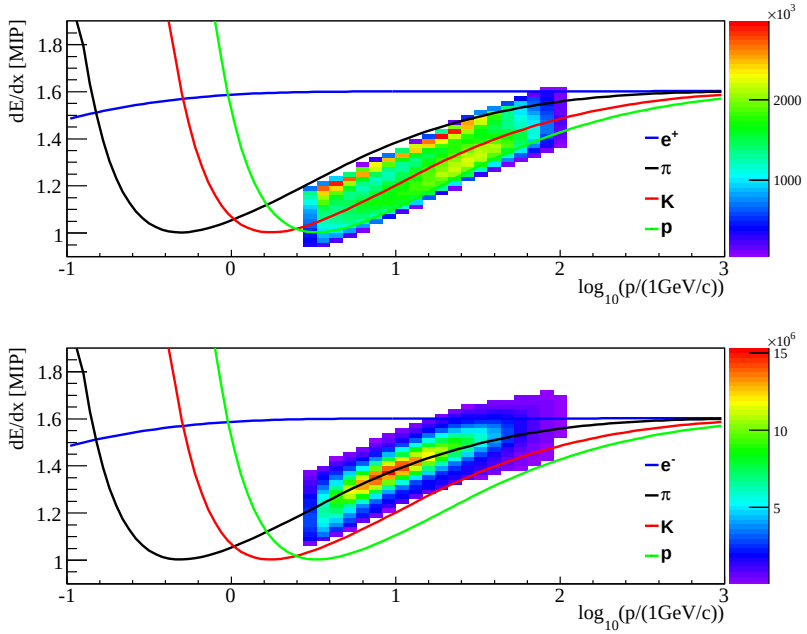

Figure 5.8: Selected K^+ and π^- candidates in the dE/dx vs. momentum plane.

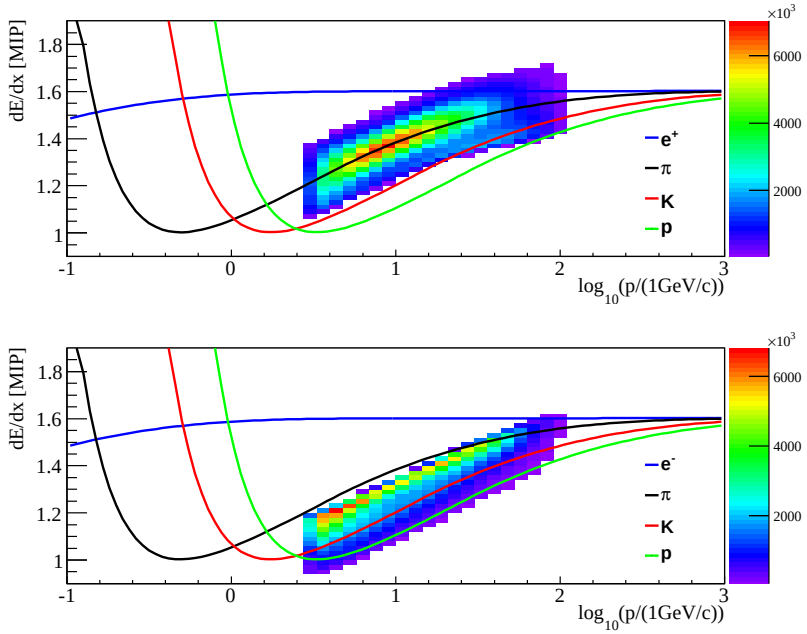

Figure 5.9: Selected K^- and π^+ candidates in the dE/dx vs. momentum plane.

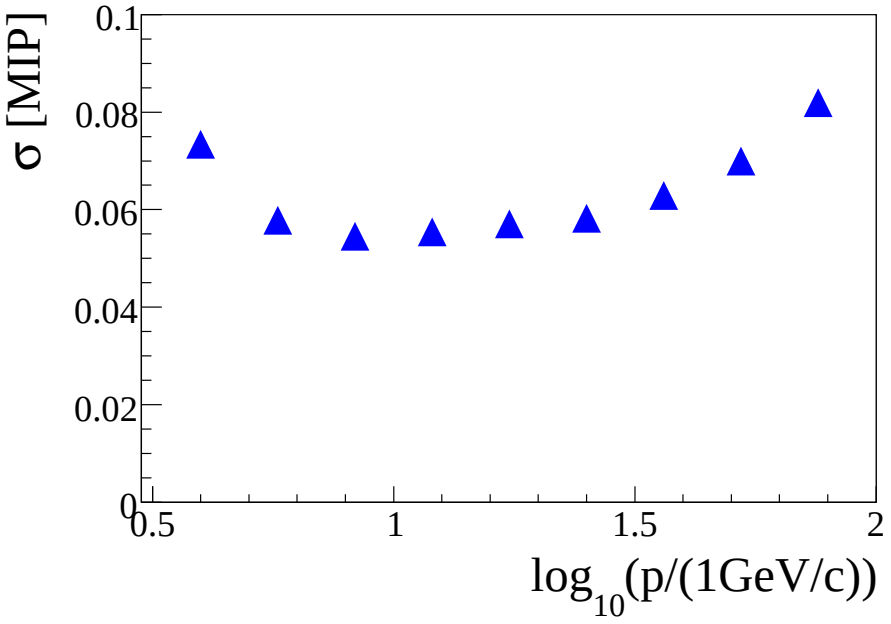

Figure 5.10: The dependencies of σ versus total momentum in the interesting region of dE/dx distribution.

5.3 Invariant mass spectra

Production properties of strongly decaying particles as $K^*(892)^0$, $\bar{K}^*(892)^0$, $\phi(1020)$, $\rho(770)^0$ and other resonances can be reconstructed using the invariant mass technique (see chapter 2). The invariant mass is calculated for all decay product candidates, e.g. in the case of K^* decay for all pairs of K^+ and π^- candidates. The pairs which come from K^* decay yield the invariant mass values close to the K^* mass, whereas the pairs which do not originate from the K^* decays form a broad background distribution in the invariant mass. Fig. 5.11 shows the schematic view of construction of invariant mass spectra. The basic kinematic variables are defined in Appendix A.

Momentum of a $K\pi$ pair is calculated as:

$$|p| = \sqrt{(p_{xK} + p_{x\pi})^2 + (p_{yK} + p_{y\pi})^2 + (p_{zK} + p_{z\pi})^2}. \tag{5.1}$$

Invariant mass of a pair is given by:

$$m_{inv} = \sqrt{(E_K + E_\pi)^2 - |p|^2}. \tag{5.2}$$

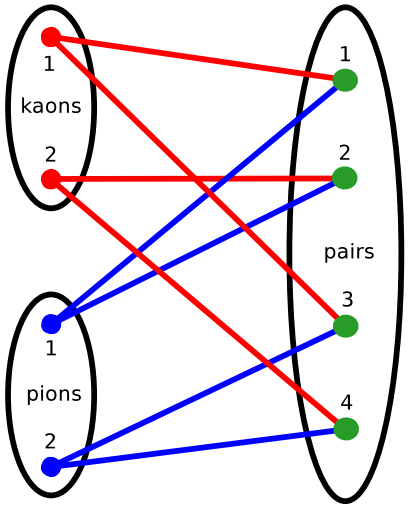

Figure 5.11: Sketch illustrating how pairs of pion and kaon candidates (right) are constructed from sets of pion and kaon candidates (left).

5.3.1 Signal distributions

In this section the $K^*(892)^0$ and $\bar{K}^*(892)^0$ invariant mass spectra are presented. The branching ratio of the observed channels $K^*(892)^0 \rightarrow K^+\pi^-$ and $\bar{K}^*(892)^0 \rightarrow K^-\pi^+$ is $2/3$. Figs 5.12 and 5.13 show the invariant mass spectra of $K^+\pi^-$ candidate pairs and Figs 5.14 and 5.15 show the invariant mass spectra of $K^-\pi^+$ candidate pairs. For each pair its rapidity and transverse momentum was calculated and the spectra are plotted in intervals of y and p_T. Figs 5.16 and 5.18 show the m_{inv} spectra in 5 rapidity intervals for K^* and $\bar{K}^*$ hypotheses, respectively. Figs 5.17 and 5.19 show the m_{inv} spectra in four p_T intervals in the y window $(0.43 < y < 1.78)$ for K^* and $\bar{K}^*$ hypotheses, respectively. Due to high background the K^* and $\bar{K}^*$ peaks are not seen. The signal can be seen only after the background subtraction. The two step procedure is used. First, the background calculated using the mixed event technique is subtracted. Second, the background estimated using a polynomial fit was taken into account.

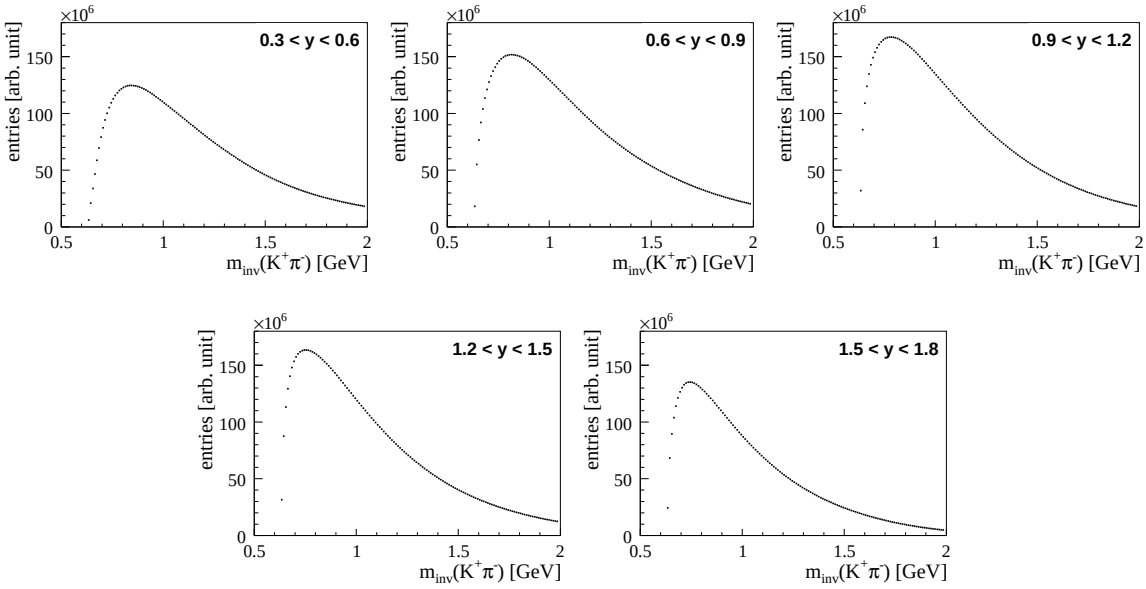

Figure 5.12: The invariant mass spectra for $K^+\pi^-$ candidate pairs in rapidity intervals.

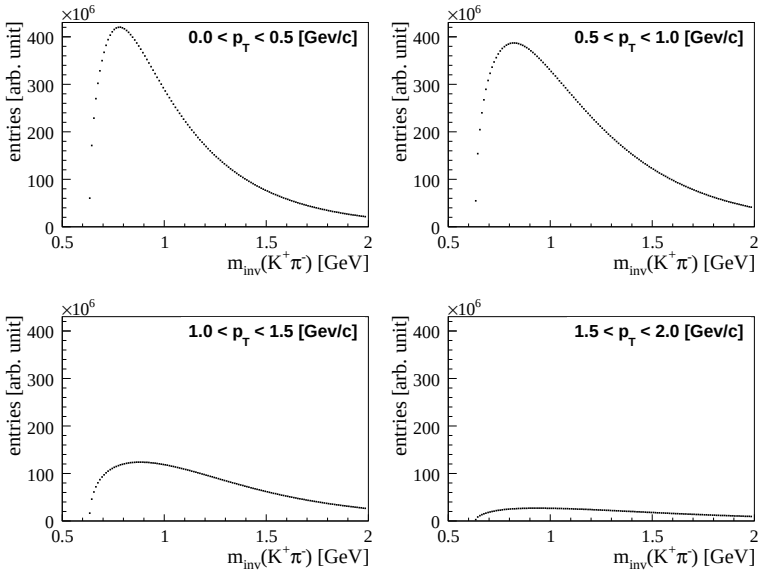

Figure 5.13: The invariant mass spectra for $K^+\pi^-$ candidate pairs in transverse momentum intervals.

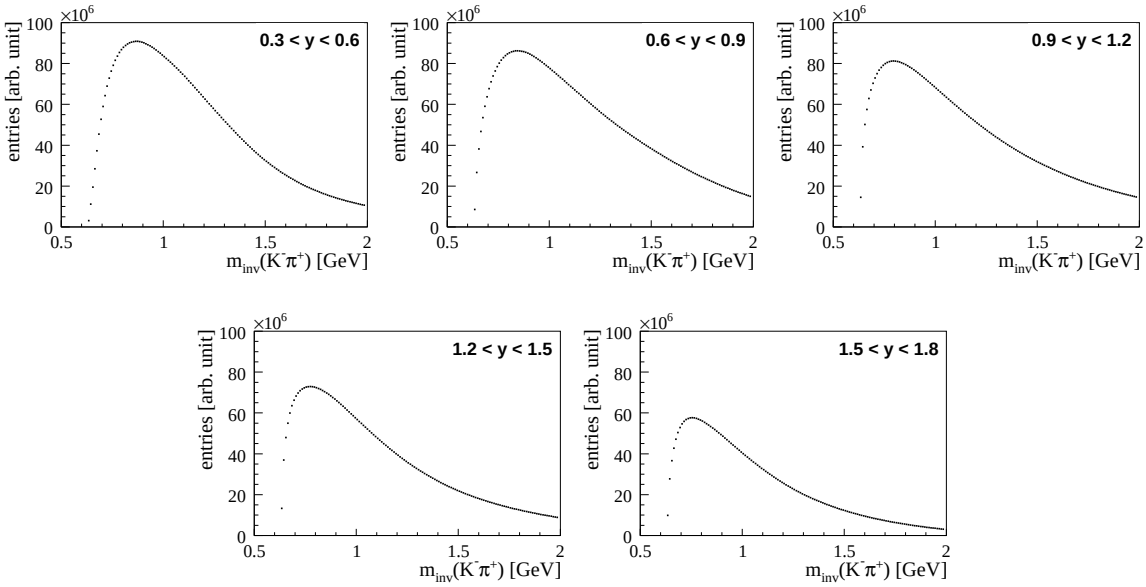

Figure 5.14: The invariant mass spectra for $K^-\pi^+$ candidate pairs in rapidity intervals.

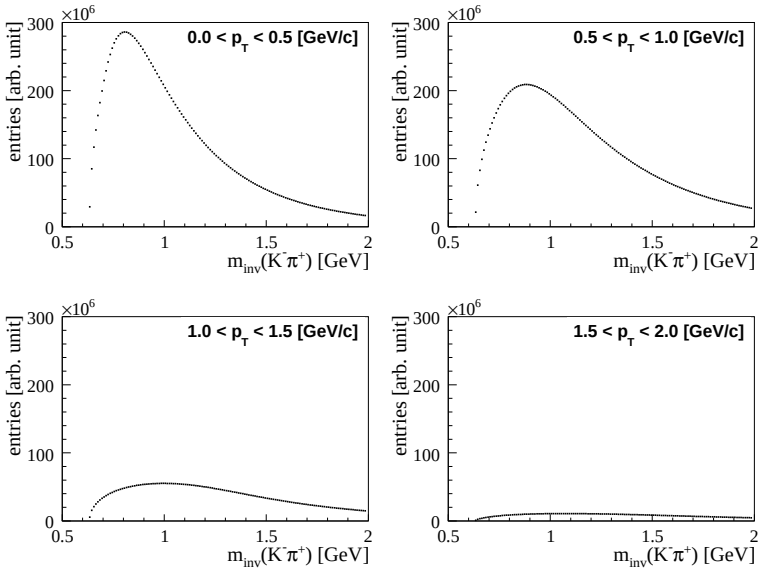

Figure 5.15: The invariant mass spectra for $K^-\pi^+$ candidate pairs in transverse momentum intervals.

5.3.2 Mixed event spectra

The mixed event invariant mass spectra were calculated as follows. Events and tracks which pass all selection cuts were selected. The measured multiplicity distribution was obtained. The artificial events with the same multiplicity distribution were created by a random selection of tracks such that opposite charged tracks in an artificial event come from different real events. Furthermore, only events with similar multiplicity were used for an artificial event creation. A new class has been developed (`T49ANA::T49MultiMixer` class) for this analysis. This class was added to T49 library (See Appendix B for details).

The mixing procedure destroys all correlations between pairs of particle (including pairs of resonance daughters), which is needed to produce a background distribution.

Figs 5.16, 5.17 5.18 and 5.19 show the invariant mass spectra for K^* and $\bar{K}^*$ hypothesis after subtraction of the mixed event background using the narrow multiplicity bins.

5.3.3 Fits to invariant mass spectra

The invariant mass spectra obtained after subtraction of the mixed event background are used to extract the yields of K^* and $\bar{K}^*$ resonances. The spectra are fitted by the analytical parametrization of the shape in the vicinity of the expected signal. This parametrisation includes the contributions from the signal (K^* or $\bar{K}^*$) and from the residual background. The signal is parametrized by the Breit-Wigner resonance shape with three parameters the resonance mass (m_0), the width of the signal (Γ) and its magnitude (C):

$$\frac{dN}{dm} = C \cdot \frac{\Gamma}{\pi\left(\left(m - m_0\right)^2 + \Gamma^2\right)}. \tag{5.3}$$

The mixed event background is parametrized by the polynomial. The fitted function is a sum of polynomial shape and Breit-Wigner functions. In general, the order of polynomial depends on the background shape. In this analysis polynomials up to second order are used. Thus the fit has up to six parameters. The fitting region is from 0.78 GeV to 1.1 GeV. The fitted curves to all considered invariant mass spectra are shown in Figs 5.16, 5.17, 5.18 and 5.19 by solid green lines.

The obtained parameters are summarized in Tables 5.2 and 5.3. The mass and Γ are approximately independent of rapidity and transverse momentum (Figs 6.1, 6.3). Thus for extracting raw yields these parameters are fixed as $m_0 = 896.1$ MeV and $\Gamma = 51$ MeV. Fitted mass values

are somewhat smaller then the world average. Fitted width agrees well with the world average which is in Ref. [100]. Possible systematic bias due to assumed fixed values of m_0 and Γ is discussed at the end of this chapter.

$K^*(892)^0$	y	m [GeV]	Γ [GeV]	C parameter	χ^2/ndf
$K^+(2\Delta)$	0.3-0.6	891 ± 1	36 ± 5	5933 ± 784	1.13
$\pi^-(3\Delta)$	0.6-0.9	885 ± 1	47 ± 5	10654 ± 1141	1.639
	0.9-1.2	888 ± 2	40 ± 6	8259 ± 1279	1.071
	1.2-1.5	889 ± 2	43 ± 7	8181 ± 1377	1.275
	1.5-1.8	890 ± 2	55 ± 12	9706 ± 2310	1.267
$K^+(2.5\Delta)$	0.3-0.6	891 ± 2	33 ± 6	5529 ± 870	1.132
$\pi^-(3\Delta)$	0.6-0.9	886 ± 2	49 ± 6	11311 ± 1483	1.202
	0.9-1.2	889 ± 2	42 ± 7	8924 ± 1559	0.929
	1.2-1.5	889 ± 2	40 ± 7	7940 ± 1472	0.962
	1.5-1.8	890 ± 2	54 ± 12	9977 ± 2606	1.236
$K^+(3\Delta)$	0.3-0.6	891 ± 2	30 ± 6	4962 ± 891	0.99
$\pi^-(3\Delta)$	0.6-0.9	888 ± 2	46 ± 7	10750 ± 1666	1.348
	0.9-1.2	887 ± 2	36 ± 7	8256 ± 1526	0.933
	1.2-1.5	887 ± 2	44 ± 8	8724 ± 1744	0.898
	1.5-1.8	889 ± 3	68 ± 13	13636 ± 3308	1.076
$K^*(892)^0$	p_T	m [GeV]	Γ [GeV]	C parameter	χ^2/ndf
$K^+(2\Delta)$	0.0-0.5	888 ± 2	44 ± 6	13269 ± 1982	1.143
$\pi^-(3\Delta)$	0.5-1.0	888 ± 1	43 ± 5	23253 ± 2590	0.923
	1.0-1.5	888 ± 1	47 ± 4	12858 ± 1129	0.958
	1.5-2.0	889 ± 2	56 ± 8	4364 ± 625	0.981
$K^+(2.5\Delta)$	0.0-0.5	888 ± 2	38 ± 6	11111 ± 1832	1.166
$\pi^-(3\Delta)$	0.5-1.0	888 ± 1	49 ± 5	27931 ± 2927	0.971
	1.0-1.5	889 ± 1	51 ± 5	15122 ± 1437	1.064
	1.5-2.0	890 ± 2	55 ± 8	4496 ± 687	0.906
$K^+(3\Delta)$	0.0-0.5	887 ± 6	57 ± 20	5654 ± 2296	1.595
$\pi^-(3\Delta)$	0.5-1.0	890 ± 1	31 ± 6	8275 ± 1452	0.832
	1.0-1.5	890 ± 2	58 ± 9	8506 ± 1243	1.382
	1.5-2.0	893 ± 3	57 ± 16	2128 ± 585	1.216

Table 5.2: Parameters of the fits to the invariant mass spectra, for details see the text and Appendix C.

5.3.4 Raw yields of $K^*(892)$ and $\bar{K}^*(892)$

The raw yields of $K^*(892)$ and $\bar{K}^*(892)$ were extracted in center-of-mass rapidity range $0.3 < y < 1.8$ and transverse momentum range $0 < p_T < 2$ GeV/c. They are calculated as integrals of the Breit-Wigner function fitted with the fixed mass and width parameters (see Tables 5.4

and 5.5). The invariant mass interval in which the integrals were calculated is 0.8-1.0 GeV. The normalization factor for mixed events was calculated in interval 1.1-2.0 GeV. The spectra and the fits were shown in Figs 5.16, 5.17, 5.18 and 5.19. The peaks due to the $K^*(892)^0$ and $\bar{K}^*(892)^0$ resonance states are clearly seen above a strongly mass dependent residual background.

$\bar{K}^*(892)^0$	y	m [GeV]	Γ [GeV]	C parameter	χ^2/ndf
$K^-(2\Delta)$	0.3-0.6	890 ± 3	52 ± 11	4577 ± 967	1.575
$\pi^+(3\Delta)$	0.6-0.9	893 ± 2	54 ± 7	7296 ± 946	1.229
	0.9-1.2	892 ± 2	38 ± 8	4158 ± 868	1.037
	1.2-1.5	894 ± 4	56 ± 17	3783 ± 1368	1.216
$K^-(2.5\Delta)$	0.3-0.6	888 ± 3	51 ± 15	4750 ± 1301	1.151
$\pi^+(3\Delta)$	0.6-0.9	891 ± 2	51 ± 7	8031 ± 1082	1.046
	0.9-1.2	893 ± 3	45 ± 13	4628 ± 1499	1.405
	1.2-1.5	899 ± 4	58 ± 20	4462 ± 1754	0.631
$K^-(3\Delta)$	0.3-0.6	887 ± 4	48 ± 15	4249 ± 1301	0.863
$\pi^+(3\Delta)$	0.6-0.9	891 ± 3	50 ± 9	7308 ± 1262	1.054
	0.9-1.2	892 ± 5	46 ± 25	5176 ± 3138	1.363
	1.2-1.5	900 ± 5	53 ± 23	3651 ± 1791	0.858
$\bar{K}^*(892)^0$	p_T	m [GeV]	Γ [GeV]	C parameter	χ^2/ndf
$K^-(2\Delta)$	0.0-0.5	895 ± 2	24 ± 8	3641 ± 994	1.654
$\pi^+(3\Delta)$	0.5-1.0	891 ± 2	49 ± 11	10683 ± 2710	0.898
	1.0-1.5	890 ± 2	48 ± 6	5553 ± 693	0.805
	1.5-2.0	899 ± 2	35 ± 8	1084 ± 205	1.165
$K^-(2.5\Delta)$	0.0-0.5	896 ± 2	24 ± 9	3454 ± 1126	1.486
$\pi^+(3\Delta)$	0.5-1.0	891 ± 2	51 ± 9	12248 ± 2287	0.757
	1.0-1.5	892 ± 2	58 ± 8	7862 ± 1068	0.594
	1.5-2.0	900 ± 3	41 ± 9	1456 ± 292	1.197
$K^-(3\Delta)$	0.0-0.5	870 ± 0	7 ± 8	1544 ± 988	2.05
$\pi^+(3\Delta)$	0.5-1.0	892 ± 2	51 ± 10	13135 ± 2864	0.842
	1.0-1.5	891 ± 2	57 ± 8	8917 ± 1289	0.925
	1.5-2.0	901 ± 3	48 ± 12	1797 ± 411	1.246

Table 5.3: Parameters of the fits to the invariant mass spectra, for details see the text and Appendix C.

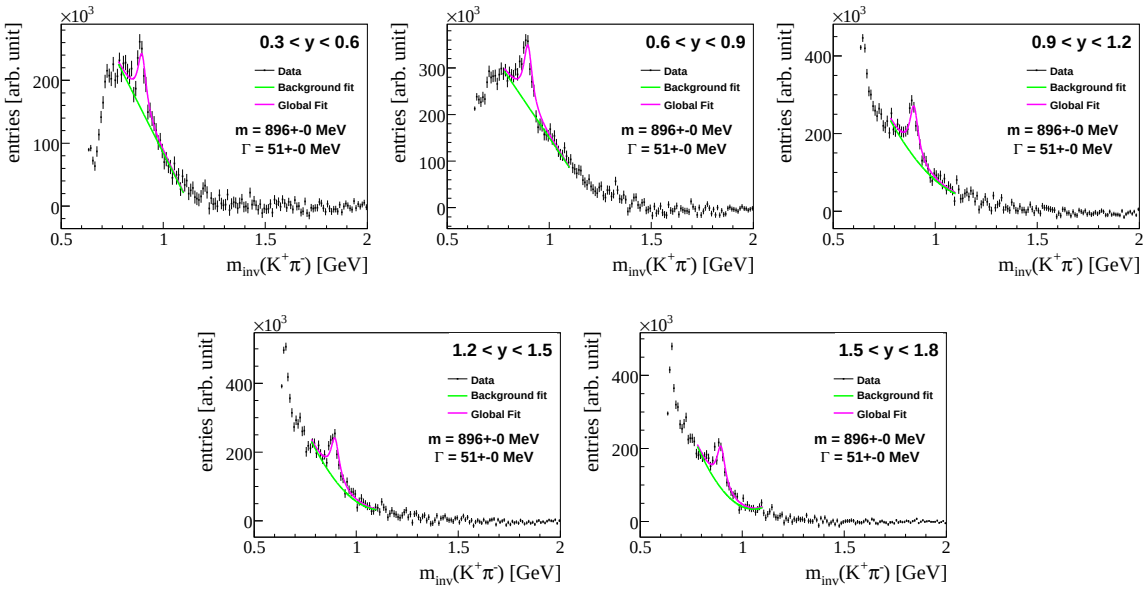

Figure 5.16: The invariant mass spectra in five different rapidity intervals (K^+: $\pm 2.5\Delta$, and π^-: $\pm 3\Delta$).

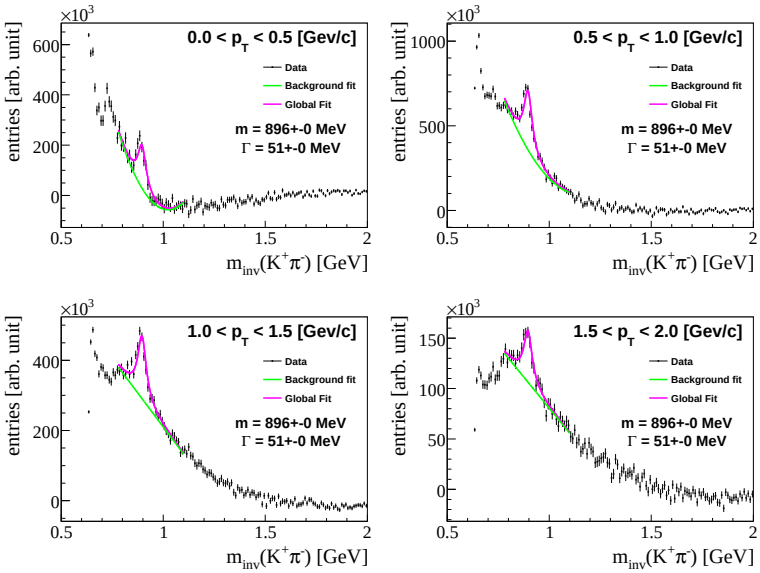

Figure 5.17: The invariant mass spectra in transverse momenta intervals (K^+: $\pm 2.5\Delta$, π^-: $\pm 3\Delta$). Rapidity interval 0.43 < y < 1.78 was selected.

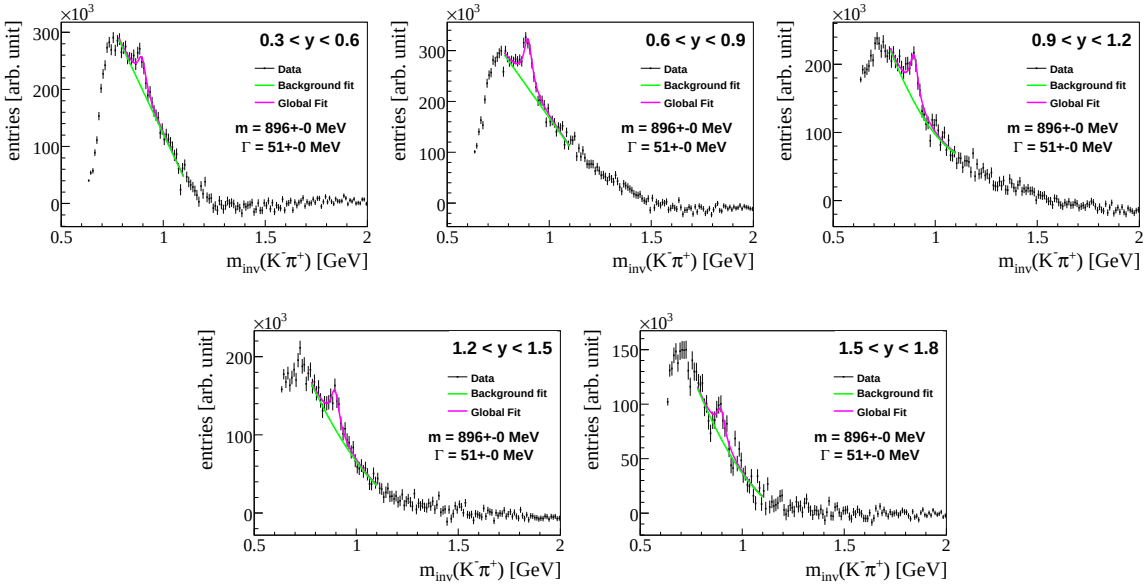

Figure 5.18: The invariant mass spectra in five different rapidity intervals (K^-: $\pm 2.5\Delta$, and π^+: $\pm 3\Delta$).

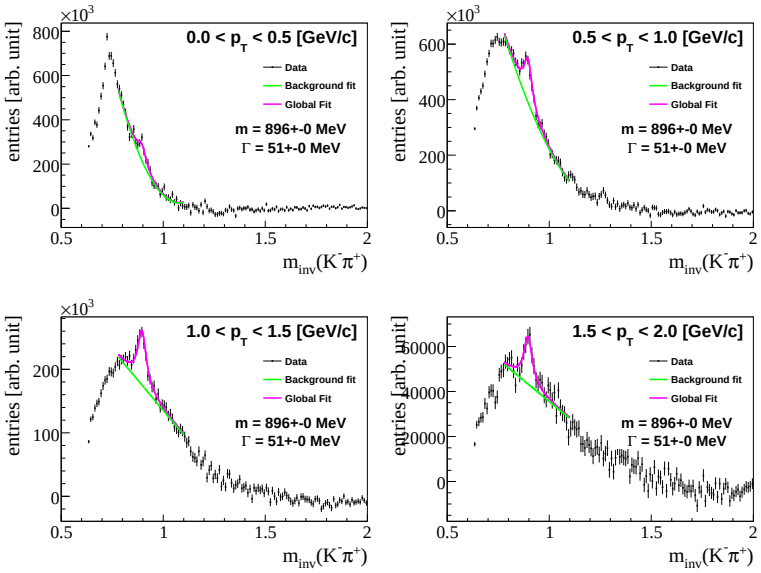

Figure 5.19: The invariant mass spectra in transverse momenta intervals (K^-: $\pm 2.5\Delta$ and π^+: $\pm 3\Delta$). Rapidity interval 0.43 < y < 1.78 was selected.

$K^*(892)^0$	y	dN_{raw}/dy	C parameter	χ^2/ndf
$K^+(2\Delta)$	0.3-0.6	633867 ± 45942	7536 ± 570	1.485
$\pi^-(3\Delta)$	0.6-0.9	851772 ± 50713	10126 ± 629	3.395
	0.9-1.2	835735 ± 52871	9936 ± 770	1.805
	1.2-1.5	794064 ± 51338	9440 ± 799	1.825
	1.5-1.8	731446 ± 45816	8696 ± 657	1.561
$K^+(2.5\Delta)$	0.3-0.6	607961 ± 53799	7228 ± 666	1.411
$\pi^-(3\Delta)$	0.6-0.9	880618 ± 58902	10469 ± 730	2.342
	0.9-1.2	882908 ± 60799	10496 ± 883	1.315
	1.2-1.5	821134 ± 58393	9762 ± 890	1.441
	1.5-1.8	770384 ± 51260	9159 ± 737	1.579
$K^+(3\Delta)$	0.3-0.6	579630 ± 62805	6891 ± 781	1.24
$\pi^-(3\Delta)$	0.6-0.9	917389 ± 68411	10906 ± 852	1.889
	0.9-1.2	910320 ± 69301	10822 ± 1036	1.556
	1.2-1.5	803561 ± 65135	9553 ± 942	1.473
	1.5-1.8	811329 ± 55962	9645 ± 808	1.48
$K^*(892)^0$	p_T	dN_{raw}/dp_T	C parameter	χ^2/ndf
$K^+(2\Delta)$	0.0-0.5	1192469 ± 79678	14177 ± 1164	1.793
$\pi^-(3\Delta)$	0.5-1.0	2227425 ± 83085	26481 ± 1324	3.018
	1.0-1.5	1088429 ± 48938	12940 ± 604	2.485
	1.5-2.0	322158 ± 22948	3830 ± 282	1.333
$K^+(2.5\Delta)$	0.0-0.5	1152370 ± 93176	13700 ± 1332	1.622
$\pi^-(3\Delta)$	0.5-1.0	2344886 ± 94087	27877 ± 1364	2.581
	1.0-1.5	1202520 ± 54247	14296 ± 669	2.113
	1.5-2.0	342098 ± 25252	4067 ± 310	1.127
$K^+(3\Delta)$	0.0-0.5	410343 ± 71186	4878 ± 1016	1.557
$\pi^-(3\Delta)$	0.5-1.0	1055507 ± 69170	12548 ± 1126	1.601
	1.0-1.5	614965 ± 38686	7311 ± 477	1.688
	1.5-2.0	158884 ± 17780	1889 ± 219	1.16

Table 5.4: Raw yield, normalization factor and χ^2/ndf for K^* peak in the rapidity and the transverse momentum intervals. Fixed parameters $m_0 = 896.1$ MeV and $\Gamma = 51$ MeV were assumed.

$\bar{K}^*(892)^0$	y	dN_{raw}/dy	C parameter	χ^2/ndf
$K^-(2\Delta)$	0.3 -0.6	359132 ± 37759	4270 ± 465	1.635
$\pi^+(3\Delta)$	0.6-0.9	570544 ± 35911	6783 ± 444	1.26
	0.9-1.2	455348 ± 34172	5413 ± 509	1.2
	1.2-1.5	297447 ± 31933	3536 ± 463	1.144
	1.5-1.8	197872 ± 27929	2352 ± 401	1.141
$K^-(2.5\Delta)$	0.3-0.6	369371 ± 46233	4391 ± 571	1.284
$\pi^+(3\Delta)$	0.6-0.9	649851 ± 44897	7726 ± 555	1.171
	0.9-1.2	460446 ± 42785	5474 ± 651	1.362
	1.2-1.5	331160 ± 39836	3937 ± 582	0.616
	1.5-1.8	181280 ± 34290	2155 ± 492	1.865
$K^-(3\Delta)$	0.3-0.6	43506 ± 56824	4084 ± 704	0.936
$\pi^+(3\Delta)$	0.6-0.9	605325 ± 56836	7196 ± 704	1.115
	0.9-1.2	472054 ± 53916	5612 ± 781	1.324
	1.2-1.5	287128 ± 49068	3414 ± 707	0.823
	1.5-1.8	186237 ± 41023	2214 ± 588	1.829
$\bar{K}^*(892)^0$	p_T	dN_{raw}/dp_T	C parameter	χ^2/ndf
$K^-(2\Delta)$	0.0-0.5	541567 ± 63076	6438 ± 907	1.708
$\pi^+(3\Delta)$	0.5-1.0	988109 ± 57995	11747 ± 979	1.048
	1.0-1.5	470104 ± 30310	5589 ± 373	1.233
	1.5-2.0	118157 ± 13399	1405 ± 164	1.238
$K^-(2.5\Delta)$	0.0-0.5	503218 ± 78320	5982 ± 1133	1.537
$\pi^+(3\Delta)$	0.5-1.0	1057053 ± 70164	12567 ± 1244	0.935
	1.0-1.5	578363 ± 35708	6876 ± 437	0.773
	1.5-2.0	142696 ± 15516	1696 ± 190	1.203
$K^-(3.0\Delta)$	0.0-0.5	159362 ± 95917	1895 ± 2924	1.804
$\pi^+(3.0\Delta)$	0.5-1.0	1096696 ± 83904	13038 ± 1226	0.881
	1.0-1.5	659997 ± 41389	7846 ± 507	1.182
	1.5-2.0	155048 ± 17580	1843 ± 215	1.262

Table 5.5: Raw yield, normalization factor and χ^2/ndf of $\bar{K}^*$ peak in the rapidity and the transverse momentum intervals. Fixed parameters $m_0 = 896.1$ MeV and $\Gamma = 51$ MeV were assumed.

5.4 Simulation of $K^*(892)$ and $\bar{K}^*(892)$

The correction factors for acceptance and reconstruction efficiency were derived from Monte Carlo simulations. K^* and $\bar{K}^*$ were generated with realistic distribution in transverse momentum and rapidity and then passed through the NA49 simulation chain based on GEANT 3.21 and the NA49 TPC signal simulation software. Additionally, these signals were then embedded into real events. The resulting raw data were reconstructed and analysed like original events. A matching procedure associates the reconstructed tracks with the originally generated tracks. A simple particle generator was used to create the input particle distributions. The generator assumes the K^* and $\bar{K}^*$ mass and width which are equal to the PDG values, $m_{K^*} = 896.1$ MeV and $\Gamma = 50.7$ MeV. The momentum spectrum of K^* and $\bar{K}^*$ is generated assuming the following parametrizations of the rapidity, transverse momentum and azimuthal angle spectra. The rapidity spectrum y is taken to be Gaussian with the mean equal to the c.m.s. rapidity, i.e. in the laboratory frame $y_{mid} = 2.92$ and the width of the rapidity distribution is assumed to be $\sigma = 1.2$ taken as $\sigma_y(K^+) \approx \sigma_y(\phi)$ [28]:

$$\frac{dn}{dy} \sim \frac{1}{\sigma\sqrt{2\pi}} e^{-\frac{(y-y_{mid})^2}{2\sigma^2}}. \tag{5.4}$$

The transverse momentum distribution is taken to be:

$$\frac{dn}{dp_T} \sim p_T e^{-\frac{\sqrt{m_0^2+p_T^2}}{T}}, \tag{5.5}$$

where the inverse slope parameter is equal to $T = 260$ MeV. The inverse slope parameter is arithmetical mean of $T(K^+) = 220$ MeV and $T(\phi) = 300$ MeV [101]. The simulation assumption of inverse slope parameter is not similar to reconstructed parameter from data. The azimuthal angle distribution is an isotropic one. The selected parameterization is inspired by the systematics established from the existing data on hadron production in central Pb+Pb collisions at 158A GeV [28]. The coordinates of the momentum vector are then calculated as:

$$(p_x, p_y, p_z) = \left(p_T \cdot \cos(\phi), p_T \cdot \sin(\phi), \sqrt{m_0^2 + p_T^2} \cdot \sinh(y)\right). \tag{5.6}$$

Fig. 5.20 shows the momentum vector distribution of simulated resonances. The simulated particles are tracked through the NA49 experiment by the GNA49 software [99], which is based on the GEANT 3.21 package. Taking into account the detector geometry, magnetic field, particle

decays and interactions with the detector material, the GNA49 yields simulated events consisting of track trajectories. The used GNA49 version decays K^* and $\bar{K}^*$ resonances into pions and kaons assuming 100% branching ratio into charged decay mode. The GNA49 output is translated into detector signals by MTSIM program [27]. The MTSIM generates raw TPC data in the digitized format produced by the TPC read-out electronics. Simulated raw data can be embedded to the real raw data (embedding procedure). The simulated events are reconstructed using standard NA49 reconstruction chain and the GNA49 points and tracks are matched to the reconstructed points and tracks. Finally, the output is converted from DSPACK format to ROOT `mini-DSTs`. The analysis programs are based on the ROOT framework [87] and use the T49 library [27].

Two simulation procedures were used. In the first one only $10K^*$ or $\bar{K}^*$ particles were simulated and reconstructed. This method is referred as ”empty simulation”. In the second one the raw data obtained from the simulation of $10K^*$ or $\bar{K}^*$ were embedded to the raw data from a real event. This method is referred as ”simulation with embedding”. Comparison between corrections resulting from the two methods allows to estimate an inefficiency due to high track density in central Pb+Pb collisions at 158A GeV.

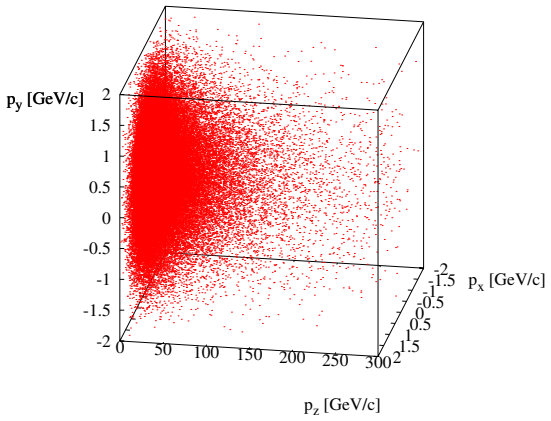

Figure 5.20: The Monte Carlo simulation. There is a visualisation of "single K^*" momentum vectors. 10^4 events were proceed. Ten K^* were defined in each event.

5.4.1 Empty simulation

Ten K^* or $\bar{K}^*$ in each event were simulated using the Monte Carlo parametrization which was described above. In this method the background is low and only simulated resonances

are present in the reconstructed events. Thus, the same procedure as used for the experimental data can be applied for the signal extraction. Fig. 5.21 shows the invariant mass distributions in the rapidity intervals and Fig. 5.22 present the invariant mass distributions in the transverse momentum intervals. The signal of K^* is well visible and the background is approximately flat. The values of m and Γ resulting from the fit are printed inside the panels in Figs 5.21 and 5.22. They are consistent with the corresponding values assumed in the simulation. The background of the invariant mass spectra is parametrized by the polynomial function.

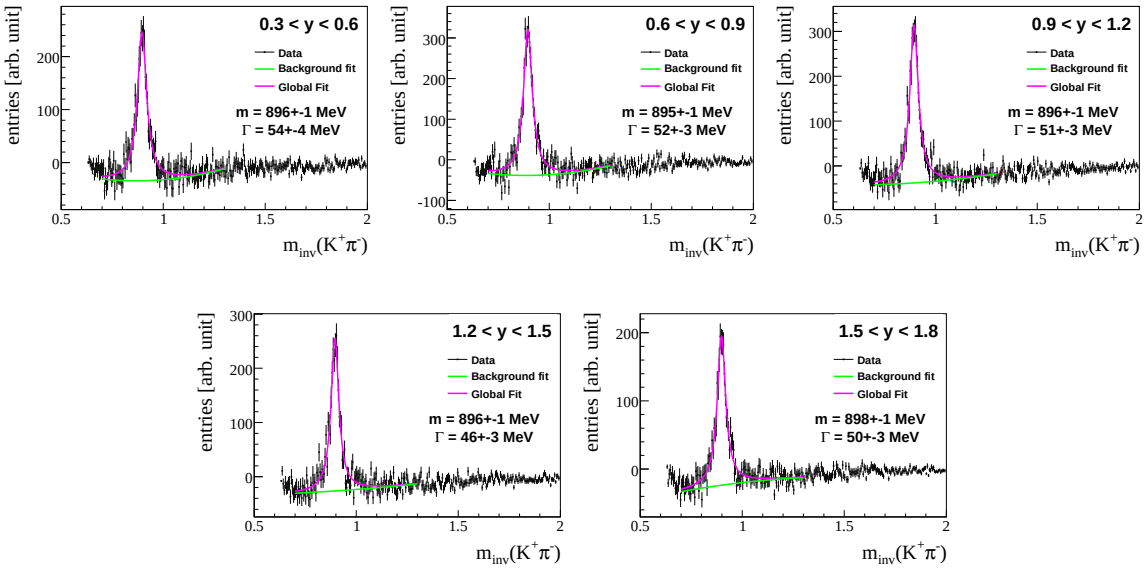

Figure 5.21: The invariant mass spectra in rapidity intervals for empty simulation of K^*.

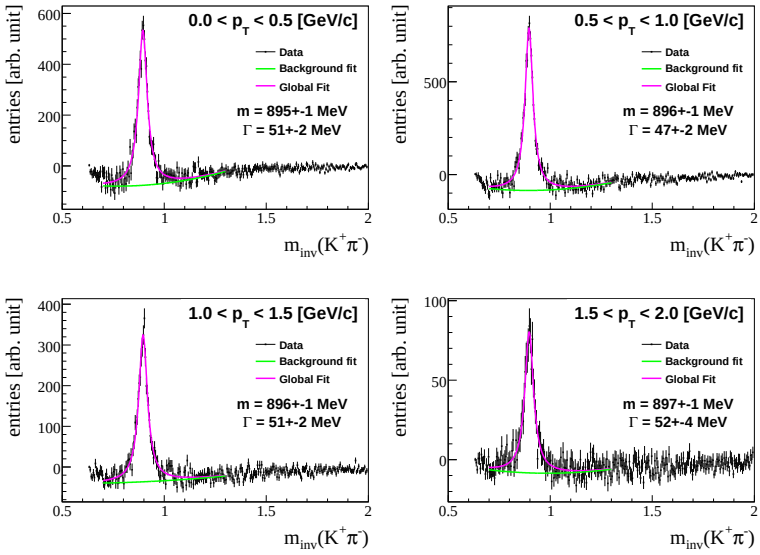

Figure 5.22: The invariant mass spectra in transverse momenta intervals for empty simulation of K^*.

5.4.2 Results from embedding procedure

In order to reproduce high track density environment of real events the raw data from the simulated K^* $(\bar{K}^*)$ decay products were embedded into the raw data from the real events. The number of simulated tracks in each event must comprise a small fraction of the number of tracks in the experimental events. In this analysis $10 \cdot K^*$ or $10 \cdot \bar{K}^*$ were simulated in each event. Reconstruction chain reconstructs both simulated and real tracks. Furthermore, the real events contain decay products of the real K^* or $\bar{K}^*$. Thus the simulated K^* $(\bar{K}^*)$ signal must be extracted from the events after reconstruction. This is done by use of the matching procedure. First, the MC points are matched to the reconstructed TPC points. This is done by a correlating point positions over a predefined search area in the pad row plane. The search area is a square of 0.5 x 0.5 cm^2, which is large enough to ensure matching a point even when a relatively large displacement occurs due to the cluster merging. This large search area can result in multiple matches between MC and reconstructed points. Second, all matches are recorded in linked lists and ambiguities are resolved at the track matching level [27]. Usually the track matching algorithm matches each MC track to a single reconstructed track. There are also cases in which a single MC track is matched to two or more reconstructed tracks (`T49ParticleMCRoot::GetNPriMatched()` function). The analysis software resolves unambiguous matches by choosing the reconstructed track which has a maximal number of matched points. The information about number of reconstructed points on a track (`T49ParticleRoot::GetNPoint()` function) allows to construct the ratio of matched points to reconstructed points. Only matches with the $N_{points}^{MATCH}/N_{points}^{REC} > 0.85$ are accepted. The invariant mass spectra are constructed using reconstructed matched tracks only. Fig. 5.23, 5.24, 5.25 and 5.26 show the invariant masses spectra of the K^* and $\bar{K}^*$ simulated signal obtained using simulation with embedding. As can be expected from the procedure there is essentially no background. The fitted signal parameters are close to the assumed ones.

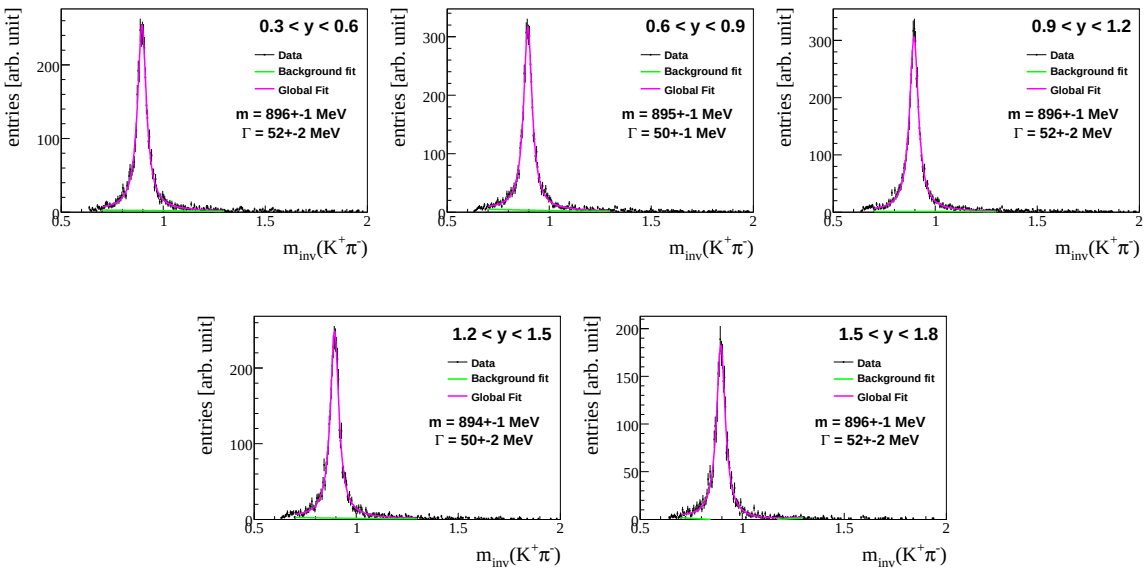

Figure 5.23: The invariant mass spectra in rapidity intervals for simulation with embedding of $K^{-}*$.

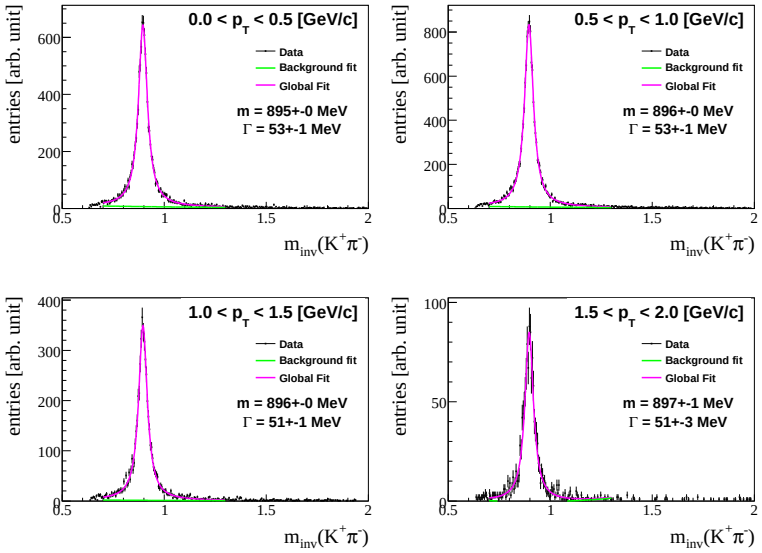

Figure 5.24: The invariant mass spectra in transverse momenta intervals for simulation with embedding of $K^{-}*$.

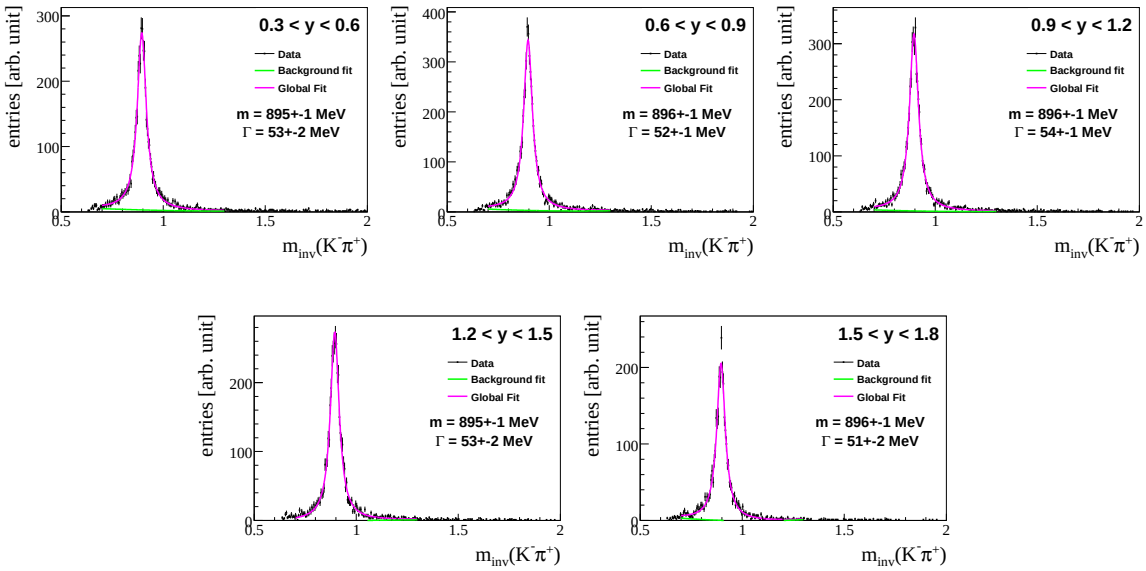

Figure 5.25: The invariant mass spectra in rapidity intervals for simulation with embedding of $\bar{K}^{*}$.

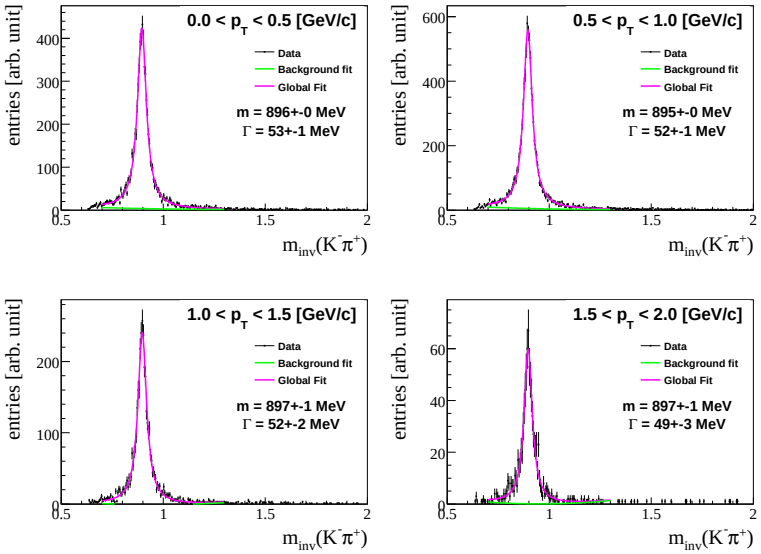

Figure 5.26: The invariant mass spectra in transverse momenta intervals for for simulation with embedding of $\bar{K}^{*}$.

5.5 Corrections

Correction factors were obtained by comparing the K^* and $\bar{K}^*$ yield extracted from the reconstructed events to the generated yield. The registration efficiency resulting from the limited geometrical acceptance, reconstruction efficiency, and losses due to the analysis cuts were calculated as:

$$efficiency = \frac{N_{REC}}{N_{MC}}, \tag{5.7}$$

where N_{REC} and N_{MC} are the numbers of reconstructed and simulated K^* or $\bar{K}^*$ resonances, respectively. As an example the results of the simulation with embedding for K^* are plotted in Fig. 5.27 in two dimensional space y-p_T. The top left and right panels show the distributions of N_{MC} and N_{REC}, respectively. The bottom panels show the distribution of the $efficiency$.

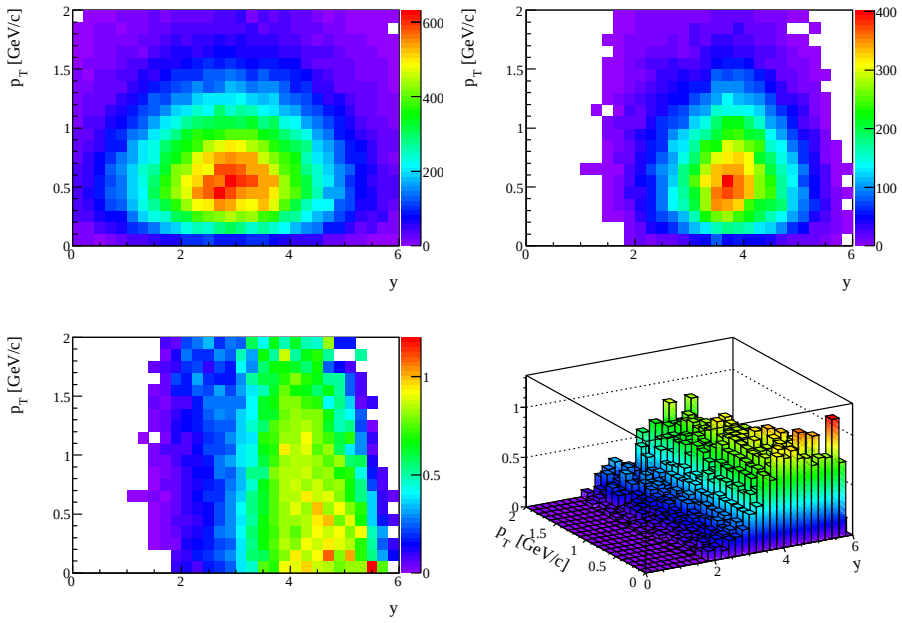

Figure 5.27: Results of the simulation with embedding for K^*. The distributions in rapidity and transverse momentum of the number of simulated K^* (top left), the number of reconstructed K^* (top right) and the ratio N_{REC}/N_{MC}.

In order to correct the experimental results the $efficiency$ was calculated in the rapidity and p_T bins used for the data analysis. The calculations were done separately for the empty simulation and the simulation with embedding. The results are presented in Figs 5.28 and 5.29. The $efficiency$ from the empty simulation is somewhat larger than in case of the embedded events. This is because the loss due to high track density are taken into account in the simulation

with embedding. In the studied intervals the efficiency is only weakly dependent on rapidity and transverse momentum.

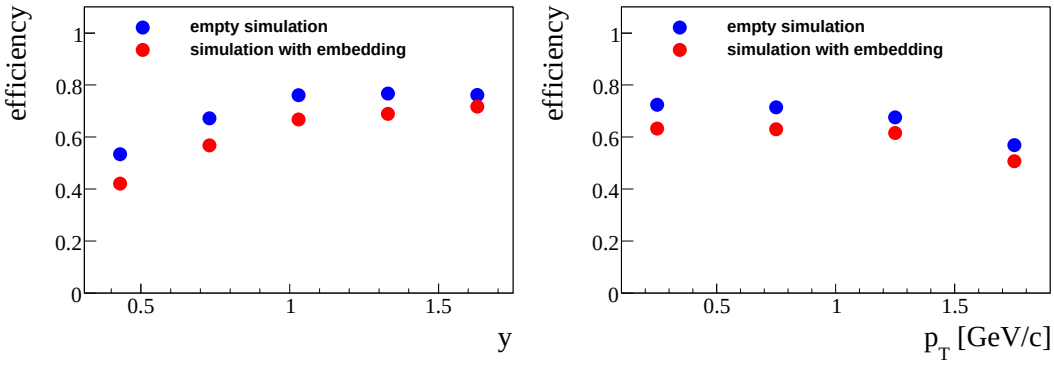

Figure 5.28: The K^* registration efficiency as a function of y (left) and p_T (right) for the empty simulation and simulation with embedding.

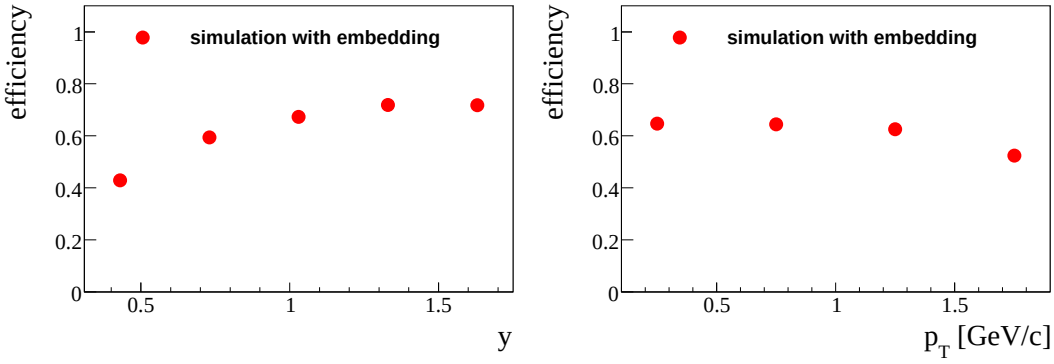

Figure 5.29: The $\bar{K}^*$ registration efficiency as a function of y (left) and p_T (right) for the empty simulation and simulation with embedding.

The original simulations were performed assuming the inverse slope parameter of the transverse momentum spectrum to be $T = 260$ MeV. The results presented in the following chapter yield $T = 339$ MeV for K^* and $T = 329$ MeV for $\bar{K}^*$. Based on these results the $efficiency$ was recalculated. The original simulation results were weighted by the factor:

$$\omega_i\left(p_T\right) = \frac{\rho_2\left(p_T\right)}{\rho_1\left(p_T\right)}, \tag{5.8}$$

where:

$$\rho_1\left(p_T\right) = C_1 \cdot p_T e^{-m_T/T_1} \qquad \rho_2\left(p_T\right) = C_2 \cdot p_T e^{-m_T/T_2}, \tag{5.9}$$

with $T_1 = 260$ MeV and $T_2 = 339$ MeV and the coefficients C_1 and C_2 were obtained from the

normalization conditions:

$$\int \rho_1 (p_T)\, dp_T = 1, \qquad \int \rho_2 (p_T)\, dp_T = 1. \tag{5.10}$$

Finally, the original $efficiency$ was replaced by the corrected $efficiency$ as:

$$C_{eff.}(\Delta p_T) = \frac{K^*_{REC}(\Delta p_T)}{K^*_{MC}(\Delta p_T)} \quad \rightarrow \quad C_{eff.}(\Delta p_T) = \frac{\sum_{i=1}^{REC} \omega_i (p_T)}{\sum_{i=1}^{MC} \omega_i (p_T)}. \tag{5.11}$$

Comparison of the original and corrected $efficiencies$ for K^* is presented in Fig. 5.30 and for $\bar{K}^*$ is presented in Fig. 5.31. The two $efficiencies$ are very similar, which reflects the fact that the $efficiency$ is only weakly dependent on p_T and consequently on the shape of the p_T distribution.

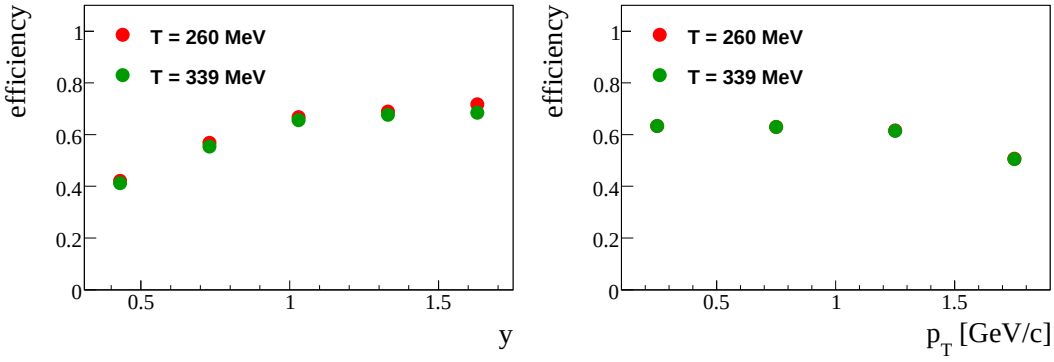

Figure 5.30: Comparison between $efficiencies$ calculated with $T = 260$ MeV and $T = 339$ MeV for K^* and the simulation with embedding. Efficiency versus transverse momentum with the center-of-mass rapidity interval $0.43 < y < 1.78$ (right).

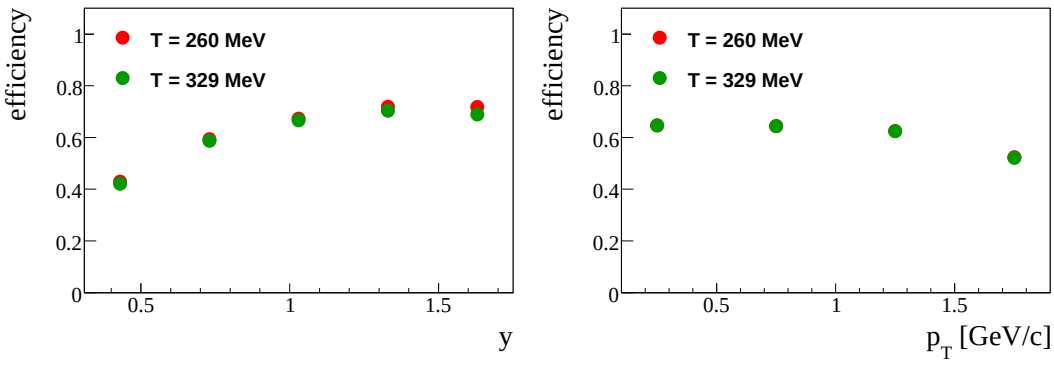

Figure 5.31: Comparison between $efficiencies$ calculated with $T = 260$ MeV and $T = 329$ MeV for $\bar{K}^*$ and the simulation with embedding. Efficiency versus transverse momentum with the center-of-mass rapidity interval $0.43 < y < 1.78$ (right).

The final correction applied to the experimental results was calculated as $1/efficiency$,

where $efficiency$ was calculated for embedding simulation with $T = 339$ MeV.

5.6 Statistical and systematic errors

In this section the statistical and systematic uncertainties are discussed.

5.6.1 Statistical uncertainties

Statistical error on the extracted K^* and $\bar{K}^*$ signal in rapidity and transverse momentum bins was calculated as follows. First, the statistical errors of the bin content, N_i^{real} and N_i^{mixed}, of the invariant mass spectra in real and mixed events were calculated as $\sqrt{N_i^{real}}$ and $\sqrt{N_i^{mixed}}$, respectively. Second, the statistical errors of the bin content, N_i^{sub} of the subtracted invariant mass spectrum were calculated as

$$\sigma(N_i^{sub}) = \sqrt{\sigma(N_i^{real})^2 + c\sigma(N_i^{mixed})^2},$$

where c is the normalization factor used for the mixed events. Third, these errors were used in the fit procedure which yields the statistical error of the signal normalization factor C. Finally, the statistical errors on the corrected rapidity and transverse momentum spectra, dn/dx, were calculated as

$$\sigma(dn/dx) = dn/dx\sigma(C)/C.$$

Another source of the statistical error is a statistical uncertainty of the correction for the detection inefficiency. The efficiency is defined as:

$$efficiency = \frac{N_{REC}}{N_{MC}}. \tag{5.12}$$

The probability to detect N_{REC} K^* resonances out of N_{MC} simulated ones is given by the binomial distribution:

$$p\left(N_{REC}\right) = \binom{N_{MC}}{N_{REC}} \cdot \epsilon^{N_{REC}} \cdot (1-\epsilon)^{N_{MC}-N_{REC}}, \tag{5.13}$$

where ϵ stands for $efficiency$. The corresponding variance is,

$$Var\left(N_{REC}\right) = N_{MC} \cdot \epsilon \cdot (1-\epsilon)\,, \tag{5.14}$$

and consequently the statistical error of N_{REC} is:

$$\sigma\left(N_{REC}\right) = \sqrt{Var\left(N_{REC}\right)}. \tag{5.15}$$

The corresponding statistical error of $efficiency$ reads:

$$\sigma\left(\epsilon\right) = \frac{\sigma\left(N_{REC}\right)}{N_{MC}} = \frac{\sqrt{N_{MC} \cdot \epsilon\,(1-\epsilon)}}{N_{MC}} = \frac{\sqrt{\epsilon \cdot (1-\epsilon)}}{\sqrt{N_{MC}}}. \tag{5.16}$$

The resulting statistical errors of $efficiency$ are below 3%. They are significantly smaller than the statistical errors due to data statistics (about 10-20%). They were not taken into account in calculations of the statistical errors of the final results.

5.6.2 Systematic uncertainties

Systematic errors are calculated by checking the stability of the results with respect to changes of the track selection cuts and parameters of the signal extraction procedure.

First, the yields were obtained using different dE/dx cuts to select kaon candidates. Three bands with the width of $\pm 2\Delta$, $\pm 2.5\Delta$, and $\pm 3\Delta$ around the mean kaon dE/dx were used and the yield was extracted assuming fixed mass and width of the K^* and $\bar{K}^*$ signal (see Appendix C for details). Free parameters of Breit-Wigner fit of the resonance signal are presented for 2.5Δ. Table 5.6 presents numerical values of differential $K^*\,(892)^0$ and $\bar{K}^*\,(892)^0$ yields in rapidity bins. The errors in the table are the statistical errors only. Results are shown also in Fig. 5.32. The same procedure was used for systematic error estimate in transverse momentum bins. The corresponding results for K^* and $\bar{K}^*$ are given in Table 5.7 and are shown in Fig. 5.33.

Second, the yields were obtained performing the fits to the invariant mass spectra in three m_{inv} intervals, namely 780-1100 GeV, 830-1050 GeV and 730-1150 GeV.

Third, the yields were extracted using 1st and 2nd order polynomial parametrization of the residual background. The corresponding results are presented in Tables 5.6 and 5.7.

The final systematic errors of yields in rapidity and transverse momentum bins were calcu-

lated as:

$$\sigma_{sys} = \frac{(n_{max} - n_{min})}{2}, \tag{5.17}$$

where the n_{max} and n_{min} are the maximum and the minimum yields obtained by varying the analysis cuts and parameters as described above. The mean value of systematic uncertainties of the K^* yields are about 24% in rapidity intervals and about 22% in transverse momentum bins. For $\bar{K}^*$ they are about 32% in rapidity intervals and about 28% in transverse momentum bins. The precision of the absolute scale of the NA49 magnetic field is better than 1% [67]. A possible bias in the magnetic field determination may influence on the position of the resonance signal. In order to determine the maximum systematic error due on the K^* and $\bar{K}^*$ mass determination due to the magnetic field uncertainty the analysis was repeated using momenta of the decay products scaled by $\pm 1\%$. The corresponding results are presented in Appendix D. They indicate such systematic error is smaller than 5 MeV.

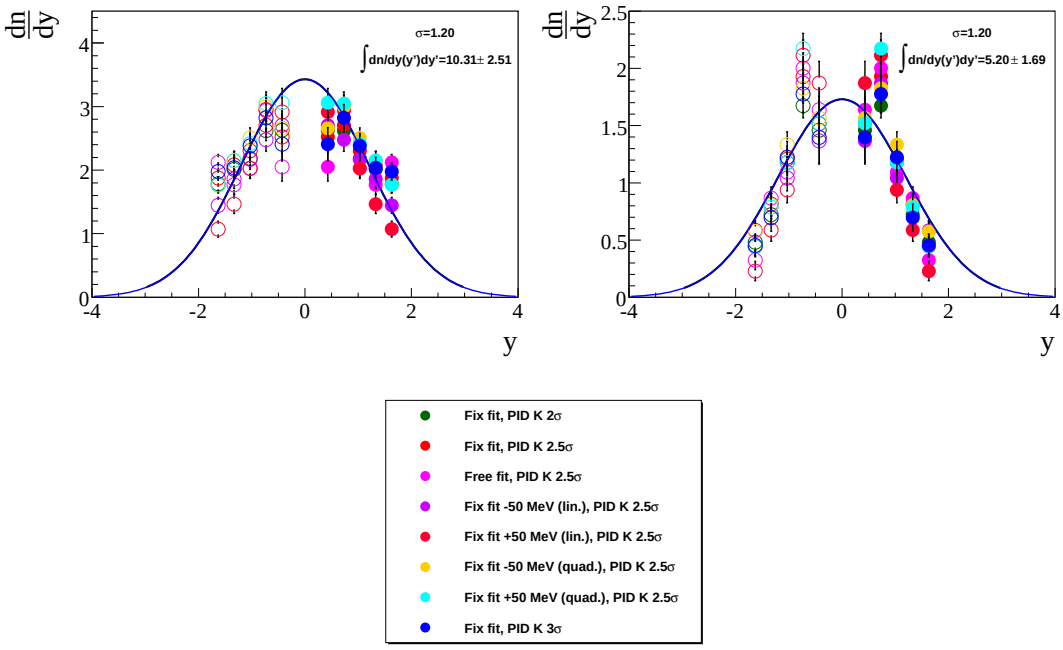

Figure 5.32: K^* (left) and $\bar{K}^*$ (right) rapidity spectra obtained for various parameters of the analysis procedure, see text for details.

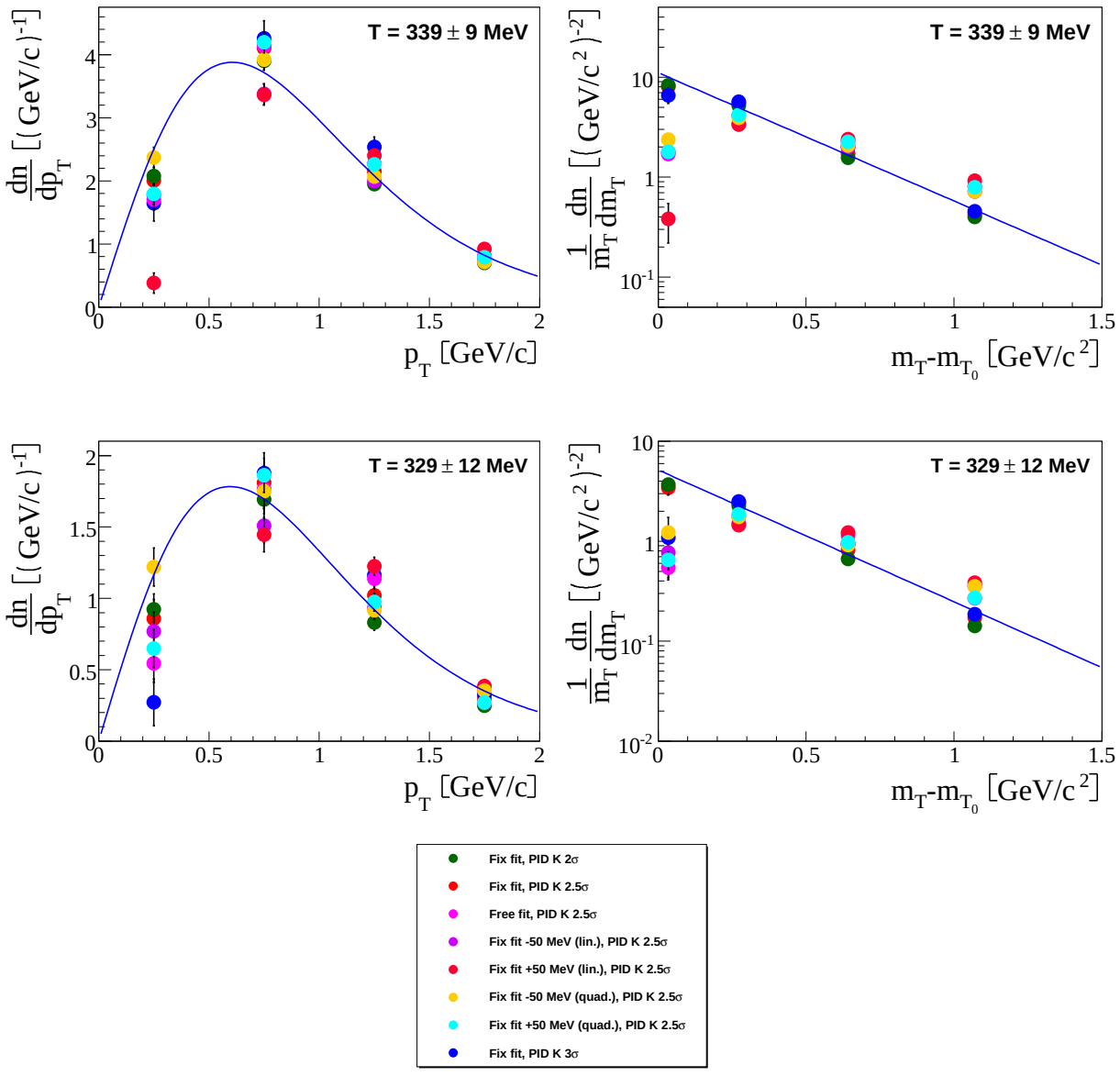

Figure 5.33: K^* (top) and $\bar{K}^*$ (bottom) transverse momentum (left) and transverse mass (right) spectra obtained for various parameters of the analysis procedure, see text for details.

y		$dn/dy(2.5\Delta)$	$dn/dy(2.5\Delta)_{free}$		$dn/dy(2.5\Delta)$	$dn/dy(2.5\Delta)_{free}$
0.3-0.6	$K^*(892)^0$	2.520 ± 0.223	2.050 ± 0.223	$\bar{K}^*(892)^0$	1.518 ± 0.190	1.639 ± 0.190
0.6-0.9		2.706 ± 0.181	2.941 ± 0.181		1.929 ± 0.133	2.003 ± 0.133
0.9-1.2		2.307 ± 0.159	2.029 ± 0.159		1.206 ± 0.112	1.092 ± 0.112
1.2-1.5		2.080 ± 0.148	1.768 ± 0.148		0.812 ± 0.098	0.866 ± 0.098
1.5-1.8		1.875 ± 0.125	2.121 ± 0.125		0.445 ± 0.084	0.324 ± 0.084
y		$dn/dy(2\Delta)$	$dn/dy(3\Delta)$		$dn/dy(2\Delta)$	$dn/dy(3\Delta)$
0.3-0.6	$K^*(892)^0$	2.630 ± 0.191	2.407 ± 0.261	$\bar{K}^*(892)^0$	1.459 ± 0.153	1.396 ± 0.231
0.6-0.9		2.620 ± 0.156	2.823 ± 0.211		1.675 ± 0.105	1.777 ± 0.167
0.9-1.2		2.185 ± 0.138	2.382 ± 0.181		1.180 ± 0.089	1.223 ± 0.140
1.2-1.5		2.013 ± 0.130	2.039 ± 0.165		0.721 ± 0.077	0.696 ± 0.119
1.5-1.8		1.782 ± 0.112	1.978 ± 0.136		0.480 ± 0.068	0.452 ± 0.100
y		$dn/dy(2.5\Delta)^{-50}_{lin}$	$dn/dy(2.5\Delta)^{+50}_{lin}$		$dn/dy(2.5\Delta)^{-50}_{lin}$	$dn/dy(2.5\Delta)^{+50}_{lin}$
0.3-0.6	$K^*(892)^0$	2.707 ± 0.223	2.916 ± 0.223	$\bar{K}^*(892)^0$	1.366 ± 0.190	1.873 ± 0.190
0.6-0.9		2.478 ± 0.181	2.954 ± 0.181		1.872 ± 0.133	2.116 ± 0.133
0.9-1.2		2.170 ± 0.159	2.026 ± 0.159		1.042 ± 0.112	0.939 ± 0.112
1.2-1.5		1.860 ± 0.148	1.466 ± 0.148		0.813 ± 0.098	0.588 ± 0.098
1.5-1.8		1.447 ± 0.125	1.073 ± 0.125		0.585 ± 0.084	0.229 ± 0.084
y		$dn/dy(2.5\Delta)^{-50}_{quad}$	$dn/dy(2.5\Delta)^{+50}_{quad}$		$dn/dy(2.5\Delta)^{-50}_{quad}$	$dn/dy(2.5\Delta)^{+50}_{quad}$
0.3-0.6	$K^*(892)^0$	2.657 ± 0.223	3.062 ± 0.223	$\bar{K}^*(892)^0$	1.566 ± 0.190	1.521 ± 0.190
0.6-0.9		3.000 ± 0.181	3.049 ± 0.181		1.827 ± 0.133	2.173 ± 0.133
0.9-1.2		2.506 ± 0.159	2.420 ± 0.159		1.334 ± 0.112	1.178 ± 0.112
1.2-1.5		2.146 ± 0.148	2.151 ± 0.148		0.806 ± 0.098	0.788 ± 0.098
1.5-1.8		1.764 ± 0.125	1.769 ± 0.125		0.574 ± 0.084	0.445 ± 0.084

Table 5.6: $K^*(892)$ and $\bar{K}^*(892)$ yields in y bins obtained for various parameters of the analysis procedure. The errors are statistical only. See text for details.

p_T		$dn/dp_T(2.5\Delta)$	$dn/dp_T(2.5\Delta_{free})$		$dn/dp_T(2.5\Delta)$	$dn/dp_T(2.5\Delta_{free})$
0.0-0.5	$K^*(892)^0$	2.006 ± 0.162	1.705 ± 0.162	$\bar{K}^*(892)^0$	0.858 ± 0.134	0.544 ± 0.134
0.5-1.0		4.102 ± 0.165	4.137 ± 0.165		1.811 ± 0.120	1.766 ± 0.12
1.0-1.5		2.151 ± 0.097	2.273 ± 0.097		1.021 ± 0.063	1.138 ± 0.063
1.5-2.0		0.744 ± 0.055	0.810 ± 0.055		0.300 ± 0.033	0.269 ± 0.033
p_T		$dn/dp_T(2\Delta)$	$dn/dp_T(3\Delta)$		$dn/dp_T(2\Delta)$	$dn/dp_T(3\Delta)$
0.0-0.5	$K^*(892)^0$	2.078 ± 0.139	1.648 ± 0.286	$\bar{K}^*(892)^0$	0.924 ± 0.108	0.271 ± 0.163
0.5-1.0		3.900 ± 0.145	4.260 ± 0.279		1.693 ± 0.099	1.877 ± 0.144
1.0-1.5		1.949 ± 0.088	2.538 ± 0.160		0.830 ± 0.054	1.164 ± 0.073
1.5-2.0		0.701 ± 0.050	0.797 ± 0.089		0.249 ± 0.028	0.326 ± 0.037
p_T		$dn/dp_T(2.5\Delta_{lin}^{-50})$	$dn/dp_T(2.5\Delta_{lin}^{+50})$		$dn/dp_T(2.5\Delta_{lin}^{-50})$	$dn/dp_T(2.5\Delta_{lin}^{+50})$
0.0-0.5	$K^*(892)^0$	1.778 ± 0.162	0.382 ± 0.162	$\bar{K}^*(892)^0$	0.769 ± 0.134	0 ± 0.134
0.5-1.0		3.378 ± 0.165	3.365 ± 0.165		1.509 ± 0.120	1.446 ± 0.120
1.0-1.5		1.993 ± 0.097	2.402 ± 0.097		0.933 ± 0.063	1.225 ± 0.063
1.5-2.0		0.719 ± 0.055	0.922 ± 0.055		0.358 ± 0.033	0.386 ± 0.033
p_T		$dn/dp_T(2.5\Delta_{quad}^{-50})$	$dn/dp_T(2.5\Delta_{quad}^{+50})$		$dn/dp_T(2.5\Delta_{quad}^{-50})$	$dn/dp_T(2.5\Delta_{quad}^{+50})$
0.0-0.5	$K^*(892)^0$	2.373 ± 0.162	1.795 ± 0.162	$\bar{K}^*(892)^0$	1.220 ± 0.134	0.649 ± 0.134
0.5-1.0		3.920 ± 0.165	4.196 ± 0.165		1.751 ± 0.120	1.862 ± 0.120
1.0-1.5		2.071 ± 0.097	2.261 ± 0.097		0.917 ± 0.063	0.974 ± 0.063
1.5-2.0		0.717 ± 0.055	0.790 ± 0.055		0.355 ± 0.033	0.271 ± 0.033

Table 5.7: $K^*(892)$ and $\bar{K}^*(892)$ yields in p_T bins obtained for various parameters of the analysis procedure. The errors are statistical only. See text for details.

Chapter 6

Results on K^* and $\bar{K}^*$ production in central Pb+Pb collisions at 158A GeV

This chapter presents final results on the K^* and $\bar{K}^*$ production properties in central Pb+Pb collisions at 158A GeV. The data on mass and width of these particles are given in section 6.1. Rapidity distributions and total mean multiplicities are presented in section 6.2. Transverse momentum and inverse slope parameters are shown in section 6.3.

6.1 K^* and $\bar{K}^*$ mass and width

The parameters of the K^* and $\bar{K}^*$ signal were obtained from fits to the background subtracted mass distribution. The signal shape was parametrized by the Breit-Wigner distribution whereas the background by first or second order polynomials. The fits were performed in five intervals of rapidity and four intervals of transverse momentum. Figs 6.1 and 6.3 show mass m and Γ of K^* and $\bar{K}^*$ as a function of rapidity and transverse momentum. The error bars indicate the statistical uncertainties only, whereas the bands show the quadratic sum of statistical and systematic uncertainties (see section 5.6 for details). For most of the points the position (mass) parameter is somewhat smaller (up to 10 MeV) then the corresponding PDG value 896.1 ± 0.27 MeV [100], but the width parameter agrees within the errors with the corresponding PDG value of 50.7 MeV [100]. The precision of the absolute scale of the NA49 magnetic field is better than 1% [67]. The scaling of the magnetic field by 1.01 results in a significant increase of the mass parameter but it is not suffcient to fully reproduce the obsereved reduction in comparison to the PDG value. Fig. 6.2 shows mass m and Γ of K^* as a function of rapidity and

transverse momentum with scaled momentum of $\pm 1\%$ to determine experimental uncertainties (see Appendix D for details).

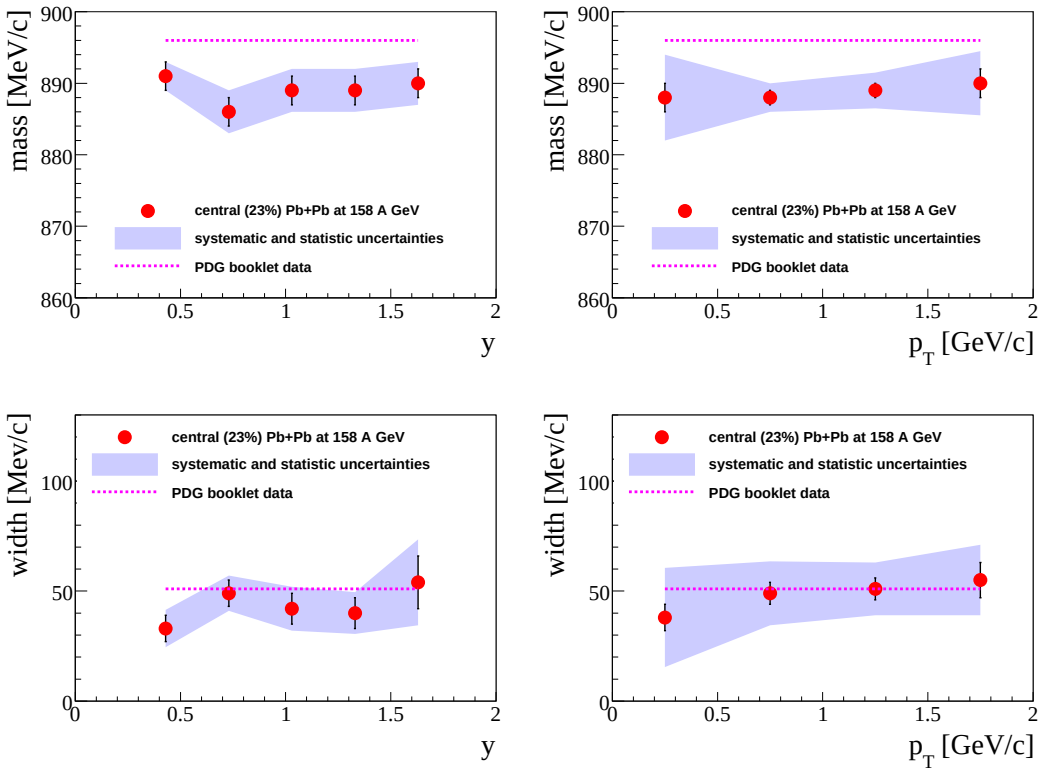

Figure 6.1: Position and width of K^* peak as a function of rapidity and p_T.

6.2 Rapidity distributions of K^* and $\bar{K}^*$

Rapidity distributions of K^* and $\bar{K}^*$ are presented in Figs 6.4 and 6.5. The results were obtained using the procedure described in section 5.3 and are fully corrected for the detection inefficiencies as well as for the branching ratio to the studied decay channel. The corrected yields were calculated as:

$$\frac{dn}{dy} = \frac{N_{raw}\left(\Delta y\right)}{N_{event} \cdot \Delta y}, \cdot \frac{\omega}{BR}, \tag{6.1}$$

where $N_{raw}\left(\Delta y\right)$ is the raw number of detected resonances, N_{event} is the number of analysed collisions, ω is a correction factor for detection inefficiency, Δy is the width of the rapidity interval and BR is a branching ratio of the observed resonance decay channel. Rapidity is given in the center-of-mass system and the yields are given in the following bins: $(0.3\text{-}0.6), (0.6\text{-}0.9), (0.9\text{-}1.2), (1.2\text{-}1.5)$, and $(1.5\text{-}1.8)$. The numerical values for the rapidity distributions of

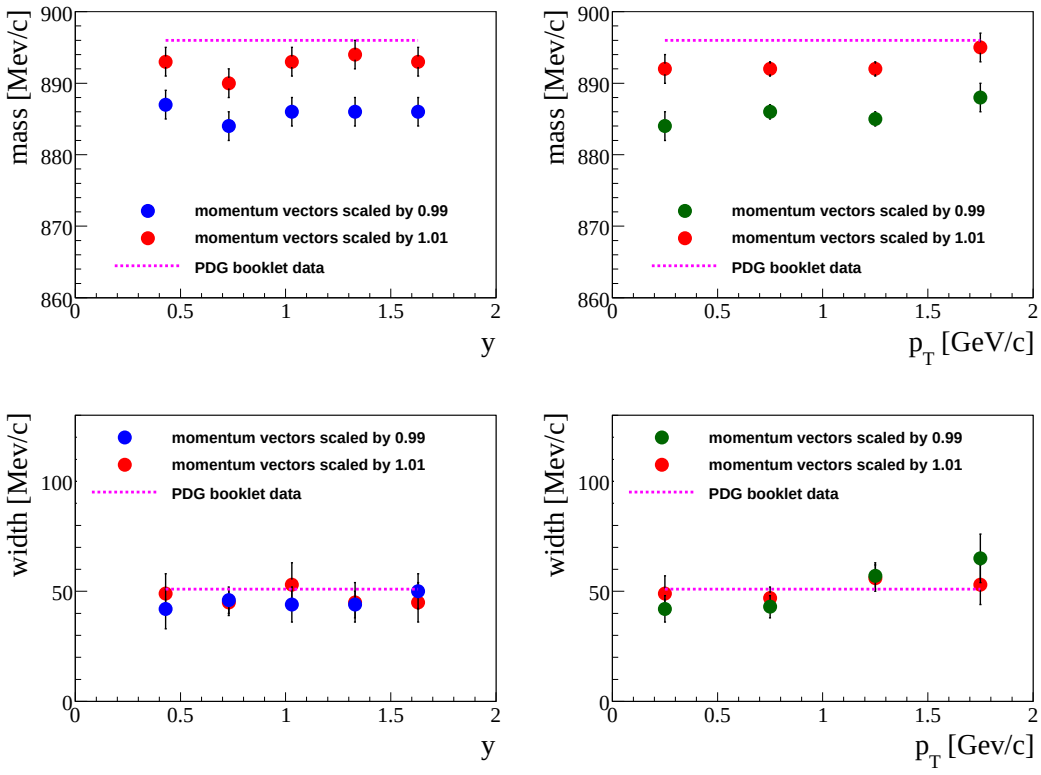

Figure 6.2: Position and width of K^* peak as a function of rapidity and p_T with scaled momentum $\pm 1\%$ to determine experimental uncertainties (see Appendix D for details).

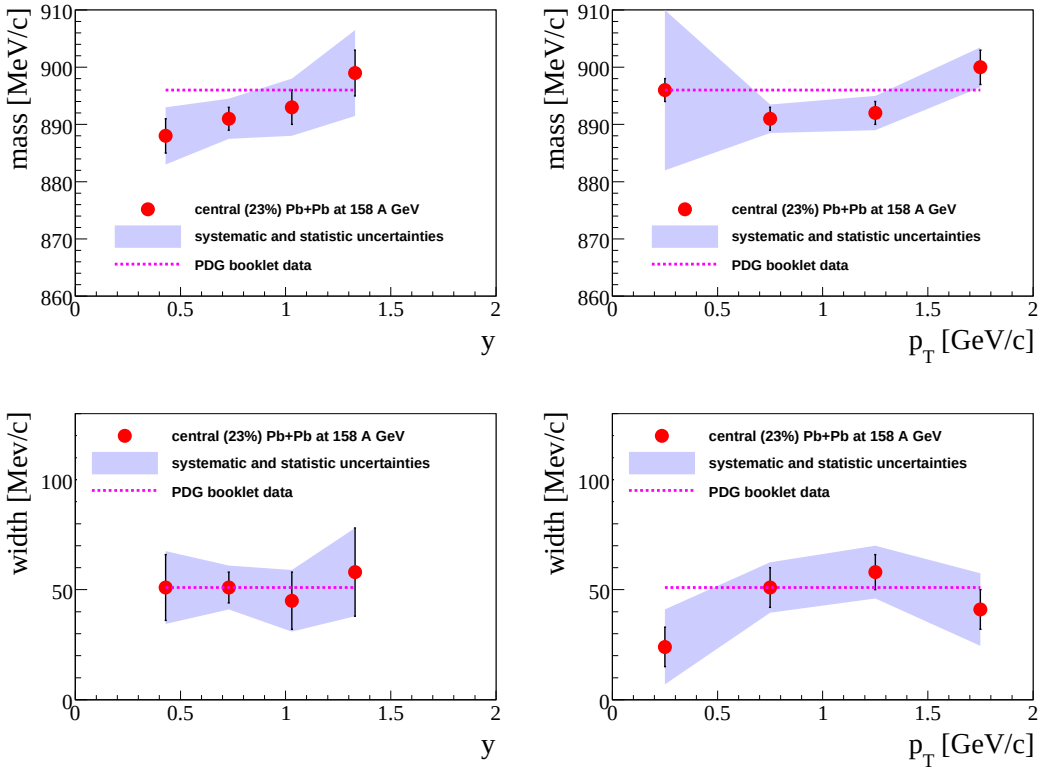

Figure 6.3: Position and width of $\bar{K}^*$ peak as a function of rapidity and p_T.

K^* and $\bar{K}^*$ are given in the Table 6.1. Gauss function was fitted to the measured rapidity distri-

	y bin	dn/dy
$K^*(892)^0$	0.3-0.6	$2.520 \pm 0.223 \pm 0.729$
	0.6-0.9	$2.706 \pm 0.181 \pm 0.466$
	0.9-1.2	$2.307 \pm 0.159 \pm 0.398$
	1.2-1.5	$2.080 \pm 0.148 \pm 0.491$
	1.5-1.8	$1.875 \pm 0.125 \pm 0.649$
$\bar{K}^*(892)^0$	0.3-0.6	$1.518 \pm 0.190 \pm 0.449$
	0.6-0.9	$1.929 \pm 0.133 \pm 0.369$
	0.9-1.2	$1.206 \pm 0.112 \pm 0.310$
	1.2-1.5	$0.812 \pm 0.098 \pm 0.237$
	1.5-1.8	$0.445 \pm 0.084 \pm 0.262$

Table 6.1: Rapidity distributions of $K^*(892)^0$ and $\bar{K}^*(892)^0$. Both statistical (first) and systematic (second) errors are given.

butions. The width parameter, σ_y, was assumed to be $\sigma_y = 1.2$ close to the width of the rapidity distribution of K^+ and $\phi(1020)$ mesons measured in the same reaction [101]. Similar width of the rapidity distribution is predicted for K^* and $\bar{K}^*$ mesons by the UrQMD model (for details see section 7.2). Mean multiplicity of K^* was extracted by integrating the Gauss function. The numerical values are given in Table 6.2. The total errors were used in the fit and thus the quoted error on the mean represents the total error.

Pb+Pb at 158A GeV	$K^*(892)^0$	$\bar{K}^*(892)^0$
multiplicity	10.31 ± 1.58	5.20 ± 0.99

Table 6.2: Mean multiplicity of $K^*(892)^0$ and $\bar{K}^*(892)^0$ mesons produced in central Pb+Pb collisions at 158A GeV. The error refers to the total uncertainty.

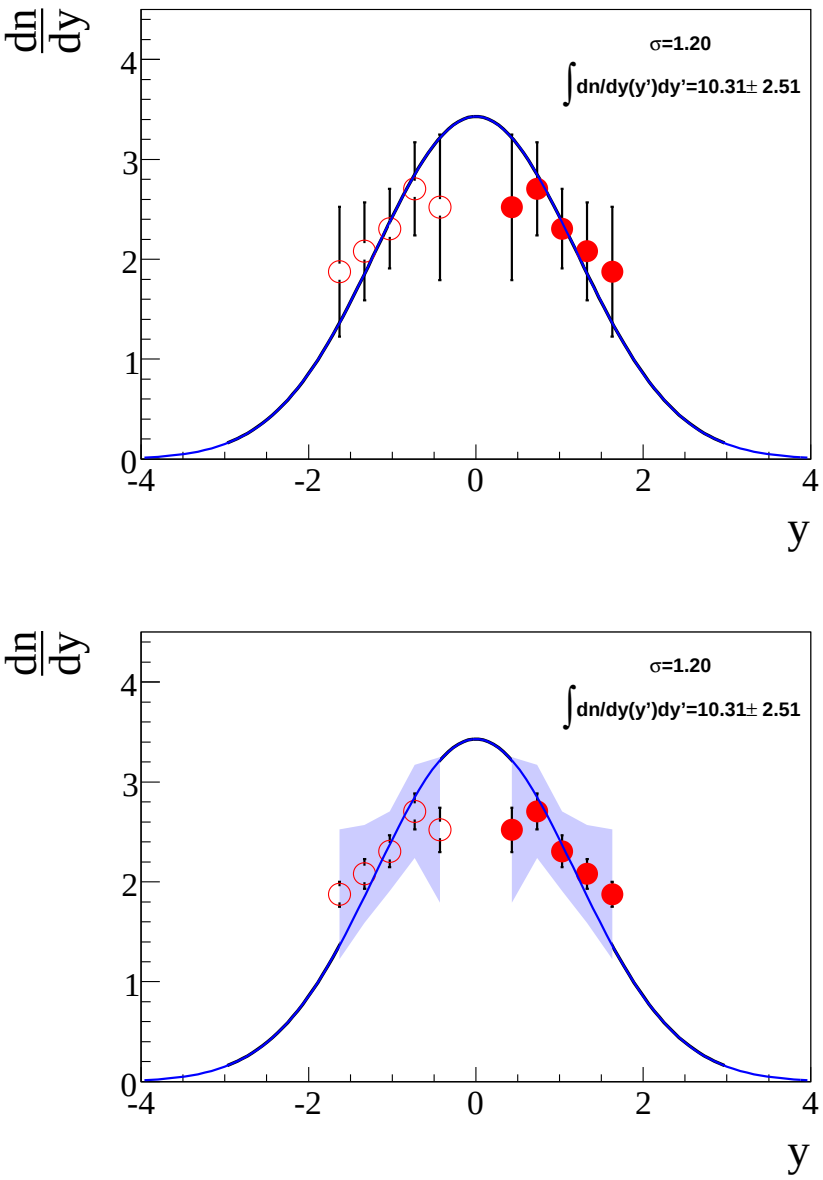

Figure 6.4: Rapidity distribution of $K^*(892)^0$ in central Pb+Pb collisions at 158A GeV. Full symbols represent the measurements, open symbols were obtained by reflection around mid-rapidity. The top plot shows the quadratic sum of statistical and systematic errors. The bars show statistical errors, the bands indicate the quadratic sum of statistical and systematic errors (bottom).

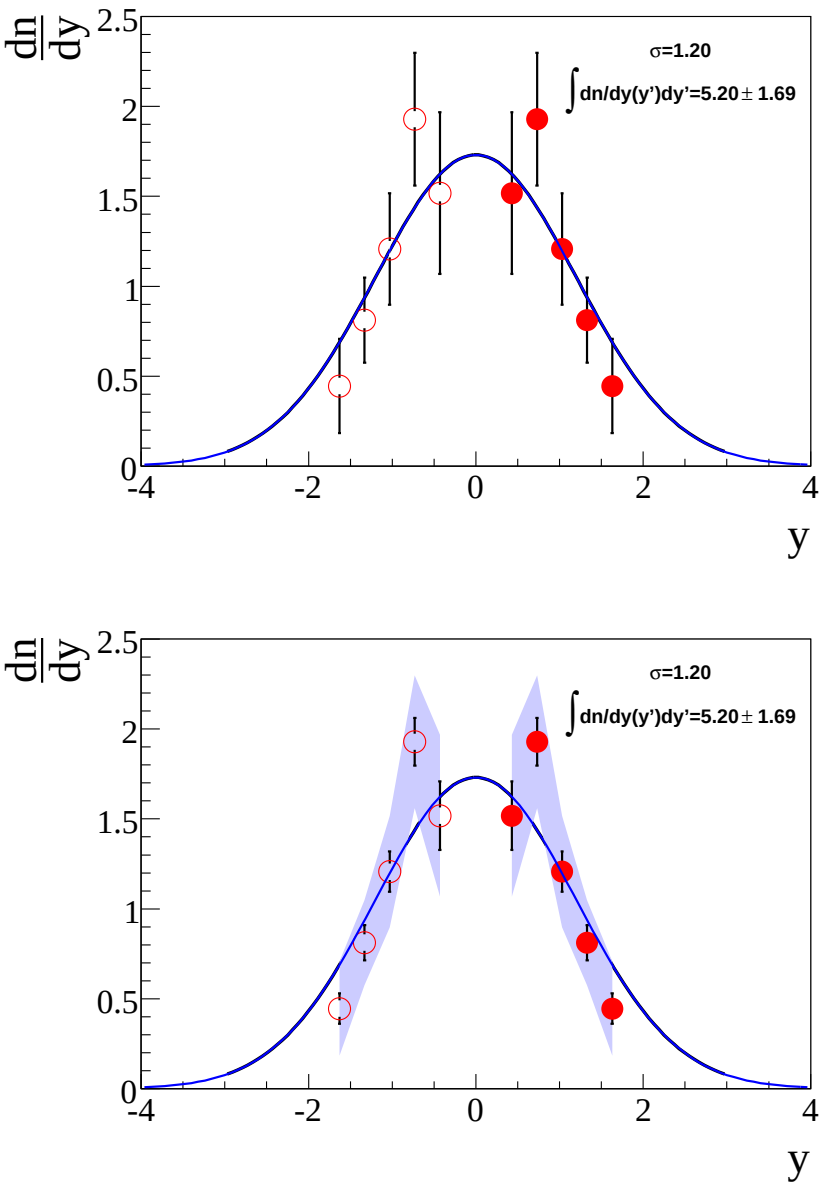

Figure 6.5: Rapidity distribution of $\bar{K}^*(892)^0$ in central Pb+Pb collisions at 158A GeV. Full symbols represent the measurements, open symbols were obtained by reflection around mid-rapidity. The top plot shows the quadratic sum of statistical and systematic errors. The bars show statistical errors, the bands indicate the quadratic sum of statistical and systematic errors (bottom).

6.3 Transverse momentum and transverse mass spectra

Transverse momentum and transverse mass spectra of K^* and $\bar{K}^*$ in the rapidity interval $0.43 < y < 1.78$ are presented in Figs 6.6 and 6.7, respectively. The results were obtained using procedure described in section 5.3 and are fully corrected for the detection inefficiencies as well as for the branching ratio to the studied decay channel. The corrected yields in p_T bins were calculated as:

$$\frac{dn}{dp_T} = \frac{N_{raw}\left(\Delta p_T\right)}{N_{event} \cdot \Delta p_T} \cdot \frac{\omega}{BR}, \tag{6.2}$$

where $N_{raw}\left(\Delta p_T\right)$ is the raw number of detected resonances, N_{event} is the number of analysed collisions, ω is a correction factor for detection inefficiency, Δp_T is the width of the p_T interval and BR is a branching ratio of the observed resonance decay channel. The yields are obtained in the following bins: (0.-0.5), (0.5-1.0), (1.0-1.5), and (1.5-2.0) GeV/c. The numerical values for the p_T spectra of K^* and $\bar{K}^*$ are given in Table 6.3, respectively. Figures. 6.6 and 6.7 show dn/dp_T spectra The mean value of systematic and statistical errors is about 22% for K^* and 28% for $\bar{K}^*$.

	p_T bin	$m_T - m_0$	$dn/dp_T[\text{GeV}/c^{-1}]$	$1/m_T dn/dm_T dy[(\text{GeV}/c^2)^{-2}]$
$K^*(892)^0$	0.0-0.5	0.034	$2.006 \pm 0.162 \pm 0.887$	$8.025 \pm 0.649 \pm 3.348$
	0.5-1.0	0.272	$4.102 \pm 0.165 \pm 0.505$	$5.469 \pm 0.219 \pm 0.673$
	1.0-1.5	0.642	$2.151 \pm 0.097 \pm 0.418$	$1.721 \pm 0.078 \pm 0.334$
	1.5-2.0	1.070	$0.744 \pm 0.055 \pm 0.117$	$0.425 \pm 0.031 \pm 0.067$
$\bar{K}^*(892)^0$	0.0-0.5	0.034	$0.858 \pm 0.134 \pm 0.462$	$3.432 \pm 0.534 \pm 1.848$
	0.5-1.0	0.272	$1.811 \pm 0.120 \pm 0.227$	$2.414 \pm 0.160 \pm 0.303$
	1.0-1.5	0.642	$1.021 \pm 0.063 \pm 0.230$	$0.817 \pm 0.050 \pm 0.184$
	1.5-2.0	1.070	$0.300 \pm 0.033 \pm 0.071$	$0.172 \pm 0.019 \pm 0.041$

Table 6.3: Transverse momentum spectrum of $K^*(892)^0$ and $\bar{K}^*(892)^0$ in the rapidity interval $0.43 < y < 1.78$. Both statistical (first) and systematic (second) errors are given.

From the measured p_T spectra the invariant yield as a function of m_T was calculated as:

$$\frac{d^2n}{m_T dm_T dy} = \frac{d^2n}{p_T dp_T dy},$$

where $m_T = \sqrt{m_0^2 + p_T^2}$. The m_T spectra are shown in Figs 6.6, 6.7 and the corresponding numerical values are given in Table 6.3.

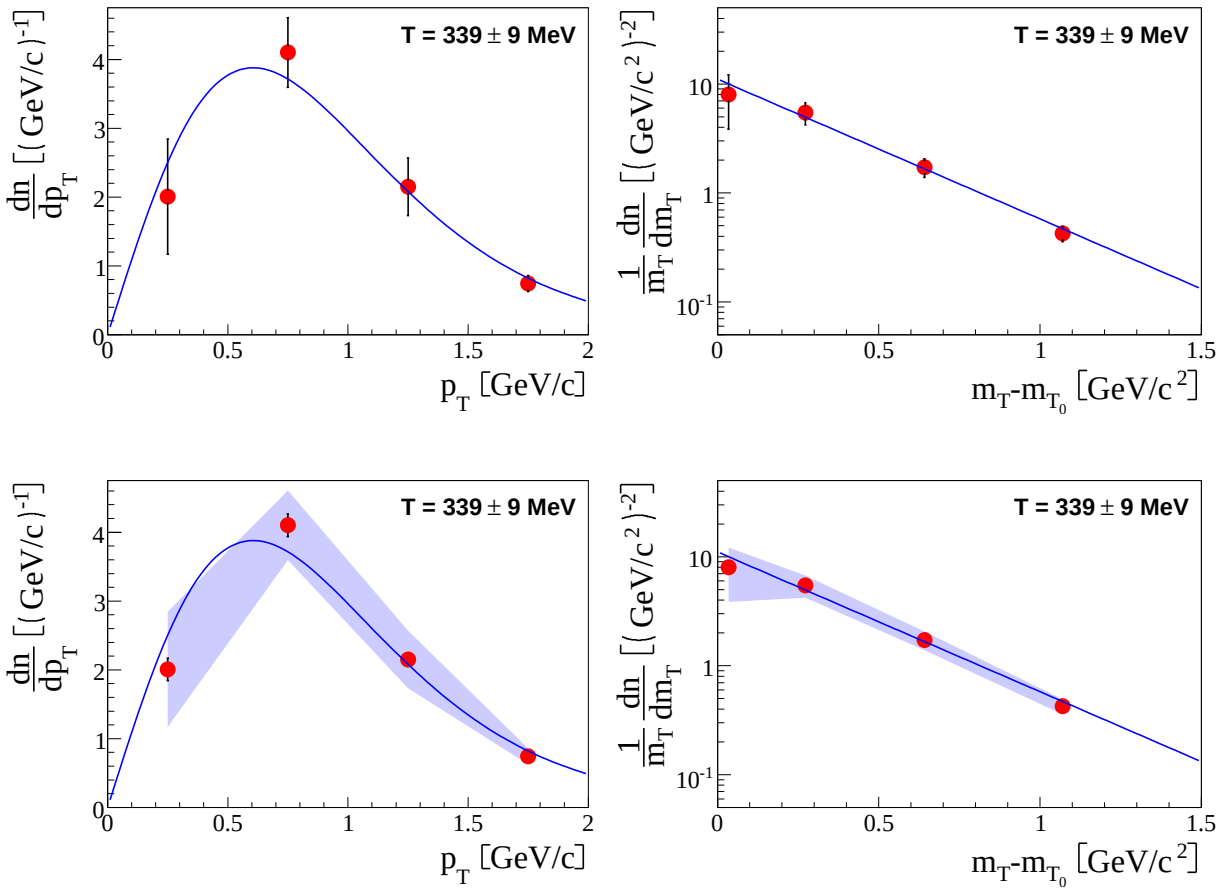

Figure 6.6: Transverse momentum p_T (left) and transverse mass m_T (right) spectra of $K^*(892)^0$ mesons produced in central Pb+Pb collisions at 158A GeV. The spectra are obtained in the rapidity interval $0.43 < y < 1.78$. The bars in the upper panel the quadratic sum of statistical and systematic errors (top). The bars in the lower panel show statistical errors and the bands indicate the quadratic sum of statistical and systematic errors (bottom).

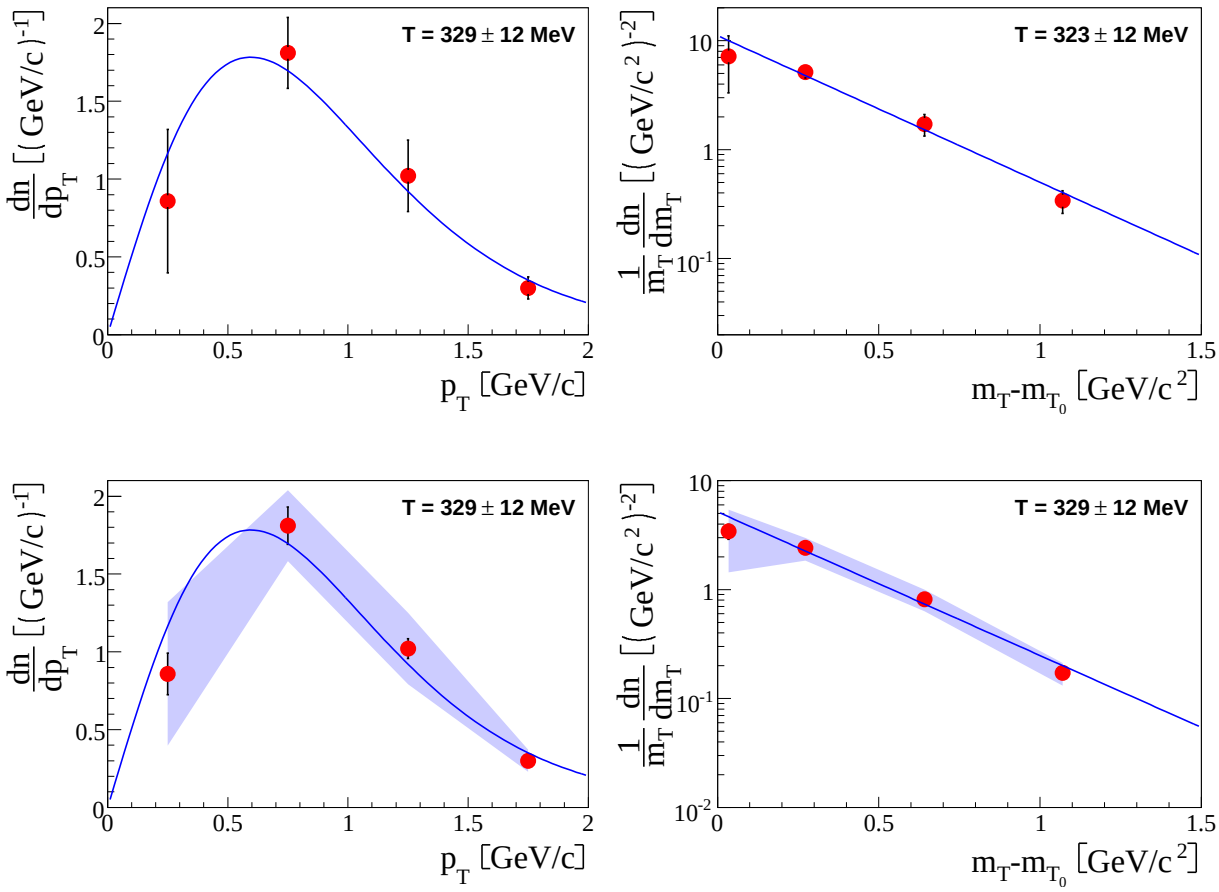

Figure 6.7: Transverse momentum p_T (left) and transverse mass m_T (right) spectra of $\bar{K}^*(892)^0$ mesons produced in central Pb+Pb collisions at 158A GeV. The spectra are obtained in the rapidity interval $0.43 < y < 1.78$. The bars in the upper panel show the quadratic sum of statistical and systematic errors (top). The bars in the lower panel show statistical errors and the bands indicate the quadratic sum of statistical and systematic errors (bottom).

The spectra were fitted by the "thermal" function:

$$\frac{dn}{dp_T dy} = C \cdot p_T \cdot e^{-\frac{\sqrt{m^2+p_T^2}}{T}}, \tag{6.3}$$

and

$$\frac{d^2n}{m_T dm_T dy} = C \cdot e^{-\frac{m_T}{T}}, \tag{6.4}$$

where C and T are fit parameters. The resulting values of the T parameter are given in Table 6.4. The total errors were used in the fit and thus the T errors refer to the total uncertainty. The fit was performed using two methods. In the first one, the value of the fitted function calculated in the middle of the bin was compared to the experimental yield. In the second method the integral of the fitted function over the bin was compared to measured yield. The obtained values of the T parameter differ by less than 5 MeV. The numerical values presented here refer to the first method.

Pb+Pb at 158A GeV	$K^*(892)^0$	$\bar{K}^*(892)^0$
T (MeV)	337 ± 8 MeV	323 ± 12 MeV

Table 6.4: Inverse slope parameter for $K^*(892)^0$ and $\bar{K}^*(892)^0$ The errors refer to the total uncertainty.

Chapter 7

Discussion and comparisons with models and with other experiments

In this chapter the results on the $K^*(892)^0$ and $\bar{K}^*(892)^0$ production in central Pb+Pb collisions at 158A GeV are compared to other experimental results on resonance production. Furthermore, the data are compared to predictions of the string hadronic model UrQMD [29, 30] and to the Hadron Gas Model (HGM) [102].

7.1 Comparison with other measurements

7.1.1 Mass and width

The comparison of the NA49 data with the STAR results [64, 70] on mass and width of K^* is shown in Fig. 7.1 as a function of K^* transverse momentum. Both experiments do not observe any evidence for the width modifications. The K^* mass is lower by about 10 MeV than the PDG value for NA49 and STAR at $p_T < 0.8$ GeV/c. At $p_T > 0.8$ GeV/c the NA49 data show the same reduction of the mass as at $p_T < 0.8$ GeV/c, whereas the STAR results are consistent with the PDG value. STAR observes the reduction of mass with decreasing p_T also for other resonances: $\phi(1020)$, $\Delta^{++}(1232)$ and $\rho(770)$ [64].

Numerical values of measured mass (m) and width (Γ) for central Pb+Pb (Au+Au) collisions at different energies are summarized in Table 7.1.

p_T	$m_{NA49}^{17.3GeV}$	m_{STAR}^{62GeV}	m_{STAR}^{200GeV}	$\Gamma_{NA49}^{17.3GeV}$	Γ_{STAR}^{62GeV}	Γ_{STAR}^{200GeV}
0.5 - 1.0	888 ± 1	889 ± 3.75	889.6 ± 4	49 ± 5	53 ± 7	58 ± 28
1.0 - 1.5	889 ± 1	894.75 ± 2.75	894 ± 3	51 ± 5	53.75 ± 8	40 ± 15
1.5 - 2.0	890 ± 2	890.5 ± 3	893.9 ± 3	55 ± 5	55 ± 5	39 ± 25

Table 7.1: Comparison of the results on mass and width of K^* measured by NA49 and STAR experiments [64, 70] in central Pb+Pb (Au+Au) collisions. Only statistical errors are given.

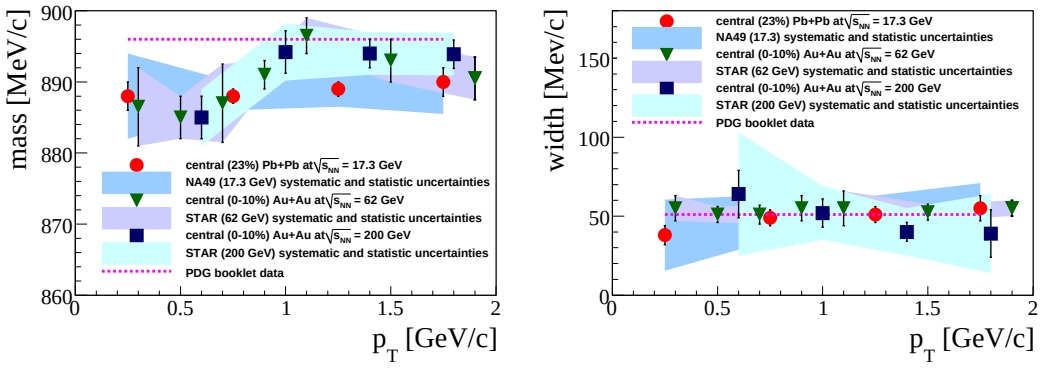

Figure 7.1: The position and the width of the K^* peak as a function of its transverse momentum in central Pb+Pb (Au+Au) collisions measured by NA49 and STAR. Statistical errors are indicated by vertical bars and systematic errors by bands [64, 70].

7.1.2 System size dependence

Preliminary NA49 results on $K^*(892)^0$ and $\bar{K}^*(892)^0$ production in minimum bias p+p and in central C+C and Si+Si collisions at 158A GeV were obtained in [80] and resulting mean multiplicities are listed in Table 7.2.

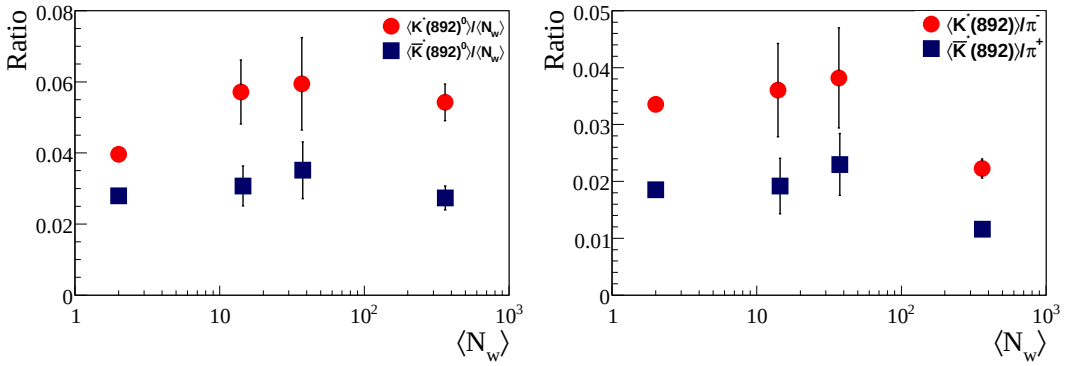

Figure 7.2: The $\langle K^* \rangle / \langle N_w \rangle$, $\left\langle \bar{K}^* \right\rangle / \langle N_w \rangle$ (left panel), and $\langle K^* \rangle / \langle \pi^- \rangle$, $\left\langle \bar{K}^* \right\rangle / \langle \pi^+ \rangle$ ratios (right panel) as a function of the number of wounded nucleons [80].

Obviously, the mean multiplicity of resonances grows with increasing system size (number of wounded nucleons). The ratio of the mean multiplicity of $K^*(892)^0$ and $\bar{K}^*(892)^0$ to number

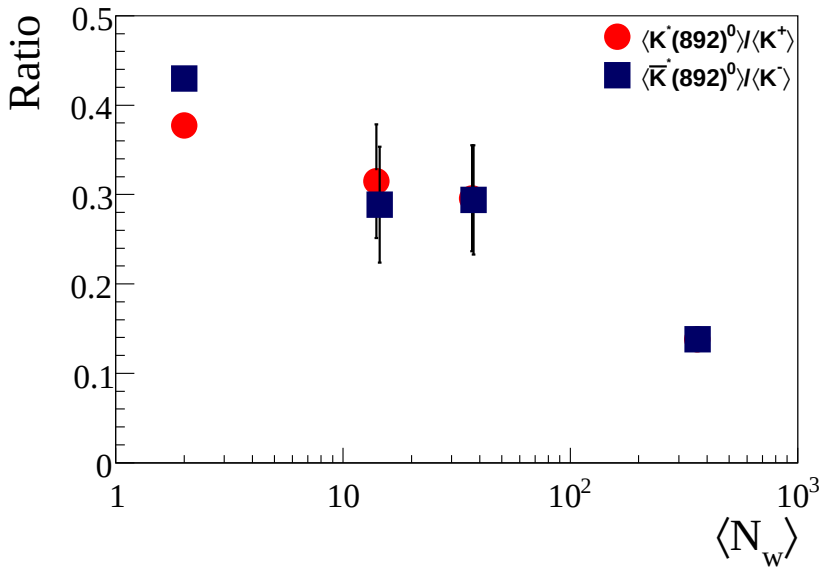

Figure 7.3: The $\langle K^* \rangle / \langle K^+ \rangle$, and $\left\langle \bar{K}^* \right\rangle / \langle K^- \rangle$ ratios in nucleus-nucleus collisions at 158A GeV as a function of the number of wounded nucleons [80].

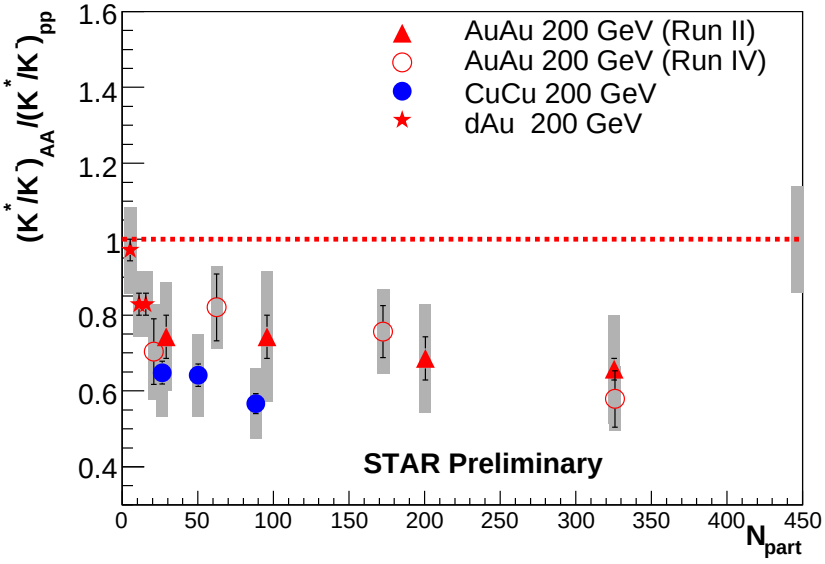

Figure 7.4: The K^*/K^- ratio in nucleus-nucleus collisions normalized by the corresponding ratio in p+p interactions at RHIC (200 GeV) as a function of participant number. The error bars correspond to statistical errors whereas the error bands are systematic uncertainties. Figure taken from [72].

of wounded is presented in Fig. 7.2 (left) as a function of N_W. The ratio is approximately independent of N_W. The ratio in central Pb+Pb collisions is lower than in p+p interactions by a factor of about 1.5 in agreement with the observations at RHIC [72]. But the validity of this conclusion is limited by large errors.

The ratios $\langle K^*(892)^0\rangle/\langle\pi^-\rangle$ and $\langle\bar{K}^*(892)^0\rangle/\langle\pi^+\rangle$ are shown in Fig. 7.2 (right) as a function of N_W. Here a significant decrease of the ratios when going from p+p to Pb+Pb collisions is observed. The reduction of the relative yield of resonances in central Pb+Pb collisions is even stronger when the ratios $\langle K^*(892)^0\rangle/\langle K^+\rangle$ and $\langle\bar{K}^*(892)^0\rangle/\langle K^-\rangle$ are considered, see Fig. 7.3.

These ratios seem to be the most relevant for physics interpretation. Both, kaons and kaon resonances are strange hadrons, and thus they are expected to be sensitive to strange quark production in a similar way. The effect of strangeness enhancement in heavy ion collisions should approximately cancel in the $\langle K^*(892)^0\rangle/\langle K^+\rangle$ and $\langle\bar{K}^*(892)^0\rangle/\langle K^-\rangle$ ratios. Consequently, a system size dependence of these ratios should be mostly sensitive to interactions in the hadronic phase of collisions. The role of these interactions is expected to increase with an increasing system size, what might explain the lower ratio in central Pb+Pb collisions.

Similar suppression of the $K^*(892)^0$ and $\bar{K}^*(892)^0$ relative yields in heavy ion collisions is observed also at RHIC. The recent results are shown in Fig. 7.4.

	p+p	**C+C**	**Si+Si**	**Pb+Pb**
$\langle N_{part}\rangle$	2	16.3 ± 1	41.4 ± 2	262.3 ± 5.8
$\left\langle K^*\,(892)^0\right\rangle$	0.0792 ± 0.0016	0.8 ± 0.24	2.2 ± 0.66	10.31 ± 1.58
$\left\langle \bar{K}^*\,(892)^0\right\rangle$	0.0559 ± 0.0011	0.43 ± 0.14	1.3 ± 0.4	5.2 ± 0.99
centrality	min. bias	15.3%	12.2%	23.5%

Table 7.2: The $K^*\,(892)$ and $\bar{K}^*\,(892)$ yields p+p, C+C, Si+Si system from [80] and Pb+Pb system from this analysis.

7.1.3 Energy dependence

The K^*/K^+ and $\bar{K}^*/K^-$ ratios in central Pb+Pb (Au+Au) collisions are shown as a function of collision energy in Fig. 7.5. The ratios significantly increase with increasing energy. This may be interpreted as due to higher role of the interactions in the hadronic phase at the SPS than at RHIC energies. (where the hadronic phase before freeze-out is probably shorter than at the SPS).

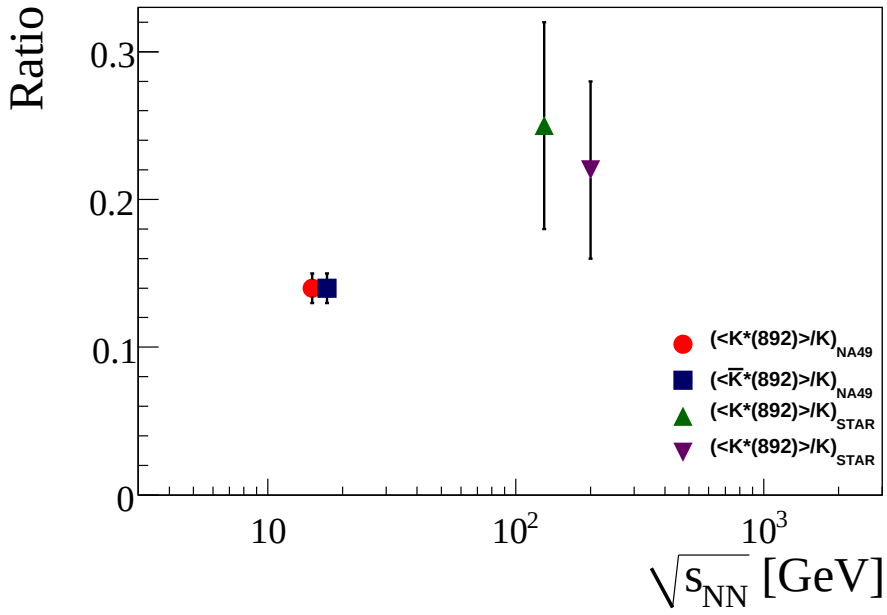

Figure 7.5: The K^*/K^+ and $\bar{K}^*/K^-$ ratios in central Pb+Pb (Au+Au) collisions as a function of collision energy. The STAR data at $\sqrt{s_{NN}} = 130$ GeV and $\sqrt{s_{NN}} = 200$ GeV [70] are used in the plot.

7.2 Comparison with string-hadronic model UrQMD

$\sqrt{s_{NN}}$	$K^*(892)^0$	$\bar{K}^*(892)^0$
17.3	10.91 ± 1.64	5.33 ± 0.80
12.3	7.93 ± 1.19	3.26 ± 0.49
8.73	5.46 ± 0.82	1.73 ± 0.26
7.62	4.54 ± 0.68	1.27 ± 0.19
6.27	3.30 ± 0.49	0.72 ± 0.11

Table 7.3: The $K^*(892)^0$ and $\bar{K}^*(892)^0$ yields as a function of collision energy within the UrQMD model [103].

The Ultra-relativistic Quantum Molecular Dynamics (UrQMD) model [29, 30] was used for comparison with the experimental data in order to trace the role of interactions in the hadronic phase. During the UrQMD simulations, new particles are produced by string excitations and decays, particle decays and particle coalescence in inelastic interactions. The space-time evolution of the system of strongly interacting particles is followed in the UrQMD simulation.

For the purpose of this work the $K^*(892)$ and $\bar{K}^*(892)$ spectra in central Pb+Pb collisions at 20A, 30A, 40A, 80A, 158A GeV were calculated [103] (see Table 7.3). The UrQMD model allows to trace back a history of resonance production and a history of resonance decay products.

Strong interactions of the decay products during the evolution of the system will change their momenta and thus the resonance can not be reconstructed using the invariant mass technique. These resonances are called the non-reconstructable resonances [99]. The effect of the interactions of decay products in the UrQMD significantly influences spectra and yields of short lived resonances [104]. For the presented comparison with the data only reconstructable resonances are selected.

Figs 7.6 and 7.7 show rapidity distributions of $K^*(892)^0$ and $\bar{K}^*(892)^0$, respectively, in central Pb+Pb collisions at the SPS energies as predicted by the UrQMD. The corresponding transverse momentum spectra are shown in Figs 7.8 and 7.9.

The mean UrQMD yields of $K^*(892)$ and $\bar{K}^*(892)$ resonances in central Pb+Pb collisions in the CERN SPS energy range are plotted as a function of collision energy in Figs 7.10 and 7.11, respectively. The resonance yield increases significantly (several times) between the lowest and the highest SPS energies. The data points at 158A GeV agree well with the model predictions.

The rapidity and transverse momentum spectra of $K^*(892)$ and $\bar{K}^*(892)$ in central Pb+Pb collisions at 158A GeV from NA49 are compared with the UrQMD distributions in Figs 7.12 and 7.13. The model agrees well with the measured rapidity distributions. However, the UrQMD transverse momentum spectra are steeper than the measured distributions. The latter difference should be taken with caution as the UrQMD spectrum was calculated in the full momentum acceptance, whereas the NA49 data refer to the NA49 midrapidity acceptance.

A fraction of non-reconstructable resonances due to the decay product interactions in the hadronic phase calculated within the UrQMD at 158A GeV increases with increasing system size. In particular, for $K^*(892)^0$ it is about 1% in p+p interactions, 10.5% in C+C, 19.4% in Si+Si and 66% in central Pb+Pb collisions [104]. The numbers for $\bar{K}^*(892)^0$ are similar [80] to those for $K^*(892)^0$. For a comparison, a fraction of $\phi(1020)$ resonances lost due to the decay product rescattering is negligible because its lifetime is ten times longer than the lifetime of $K^*(892)^0$. Furthermore, the rescattering probability of the resonance decay products depends on a cross section of the resonance decay products for interactions with hadrons in the hadronic phase [105].

As a consequence of the above arguments the agreement between the NA49 data and the UrQMD predictions is reached. The model includes resonance losses due to interactions of the decay products into account. In the UrQMD these interactions reduce the $K^*(892)^0$ and

$\bar{K}^*(892)^0$ yields by a factor of about 3. The loss probability depends on rapidity and transverse momentum. The decay products are rescattered preferentially at low transverse momenta [105]. Calculated scattering rates exhibit signs of a chemical and subsequent thermal freeze-out, giving a possibility to study a time difference between chemical and thermal freeze-outs. Furthermore, the invariant mass spectra of strongly interacting products are expected to be distorted due to the rescattering of decay products [105]. Whether this effect can, at least in part, explain the shift in the mass $K^*(892)^0$ and $\bar{K}^*(892)^0$ remains to be answered by the following studies.

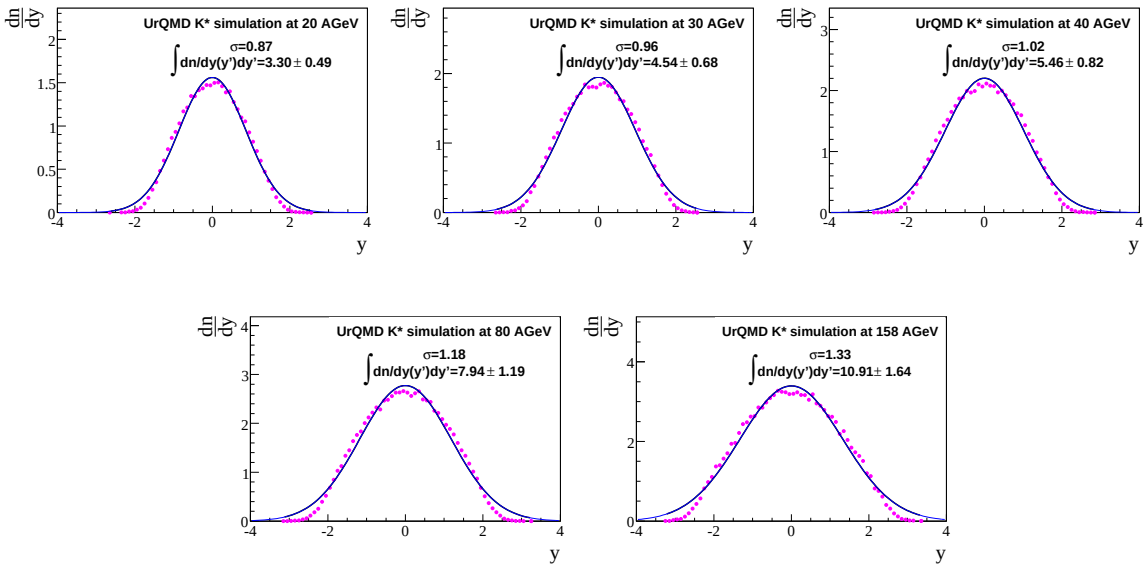

Figure 7.6: Rapidity spectra of $K^*(892)$ in central Pb+Pb collisions at 20A, 30A, 40A, 80A and 158A GeV (from top left to bottom right) calculated within the UrQMD model. The spectra are fitted with the Gauss function.

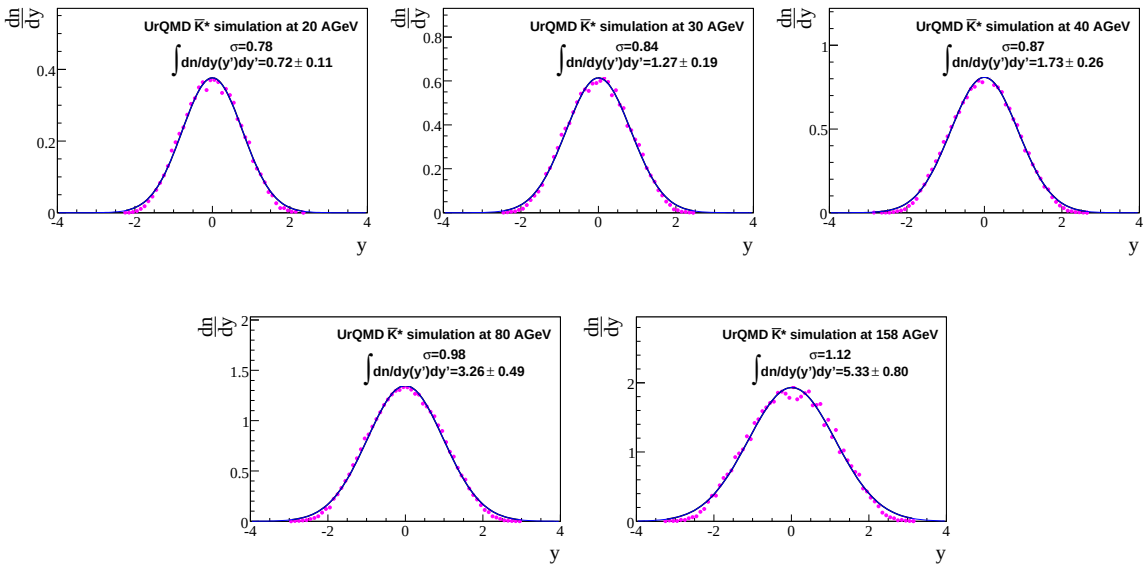

Figure 7.7: Rapidity spectra of $\bar{K}^*(892)$ in central Pb+Pb collisions at 20A, 30A, 40A, 80A and 158A GeV (from top left to bottom right) calculated within the UrQMD model. The spectra are fitted with the Gauss function.

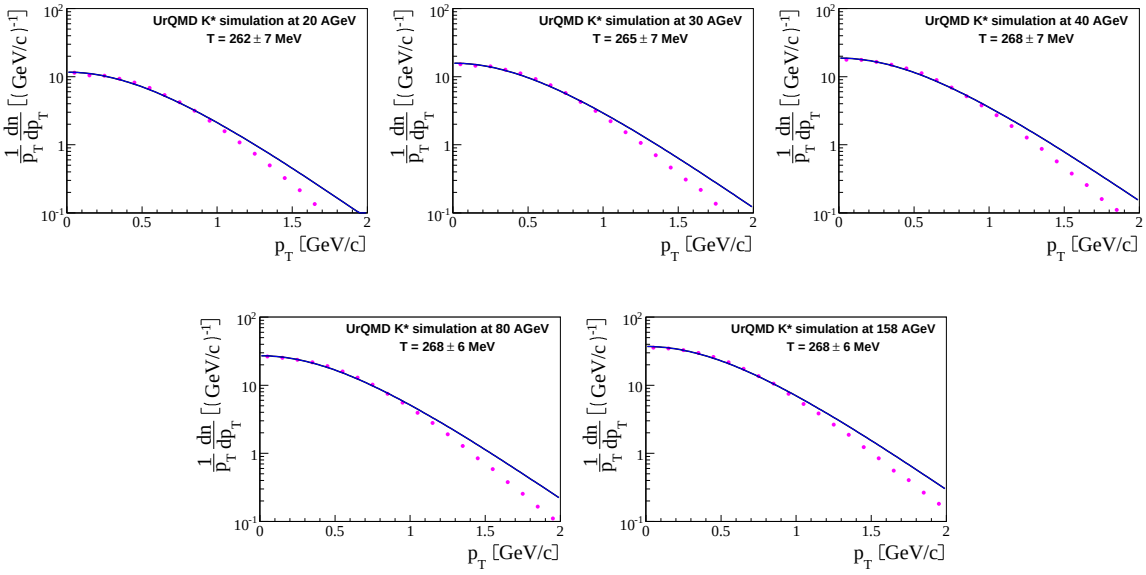

Figure 7.8: Transverse momentum spectra of $K^*(892)$ in central Pb+Pb collisions at 20A, 30A, 40A, 80A and 158A GeV (from top left to bottom right) calculated within the UrQMD model. The spectra are fitted with the Boltzmann function.

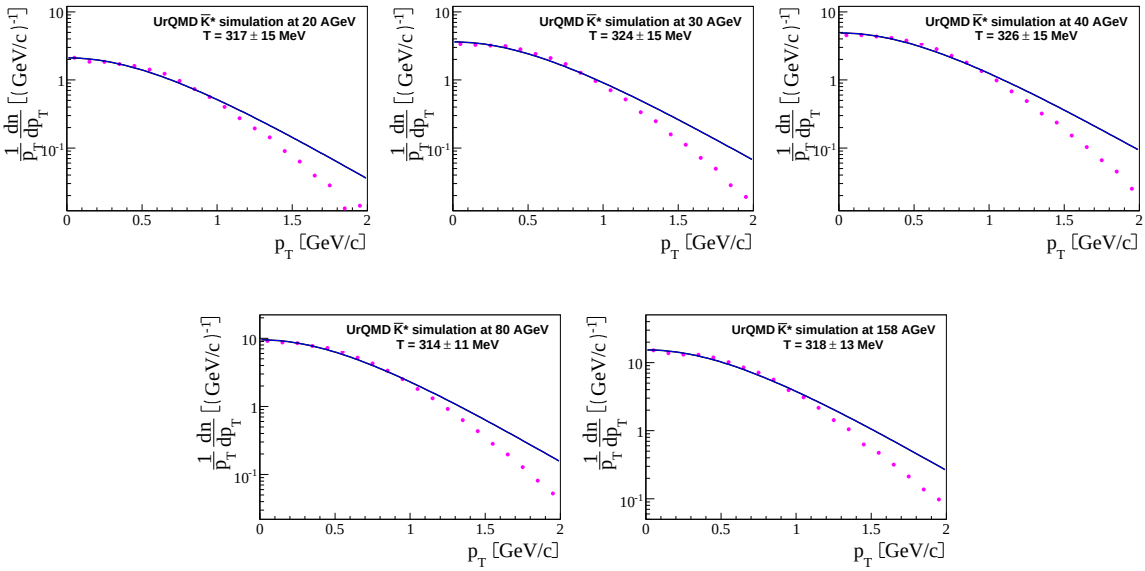

Figure 7.9: Transverse momentum spectra of $\bar{K}^*(892)$ in central Pb+Pb collisions at 20A, 30A, 40A, 80A and 158A GeV (from top left to bottom right) calculated within the UrQMD model. The spectra are fitted with the Boltzmann function.

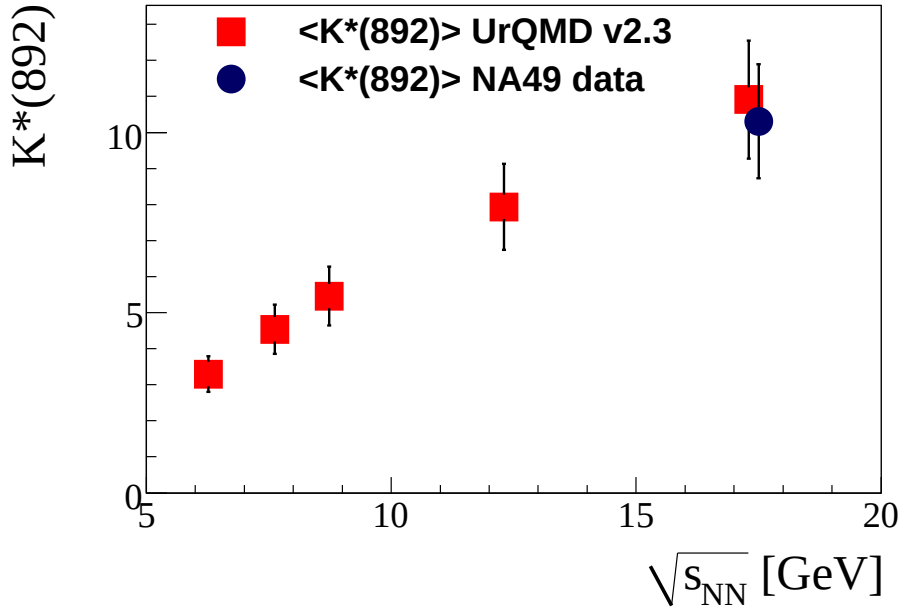

Figure 7.10: Energy dependence of $K^*(892)$ yield in central Pb+Pb collisions calculated within the UrQMD model. The NA49 data point at 158A GeV is indicated for a comparison.

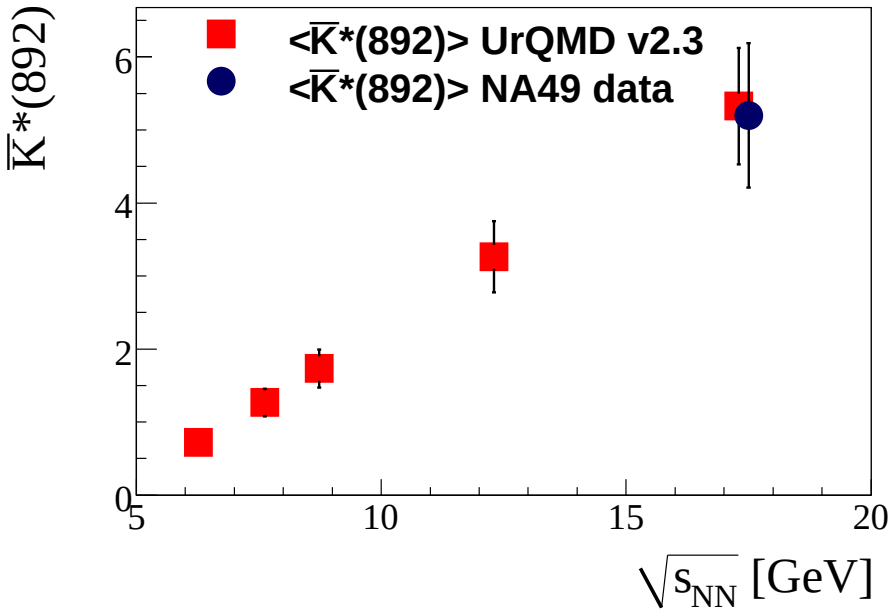

Figure 7.11: Energy dependence of $\bar{K}^*(892)$ yield in central Pb+Pb collisions calculated within the UrQMD model. The NA49 data point at 158A GeV is indicated for a comparison.

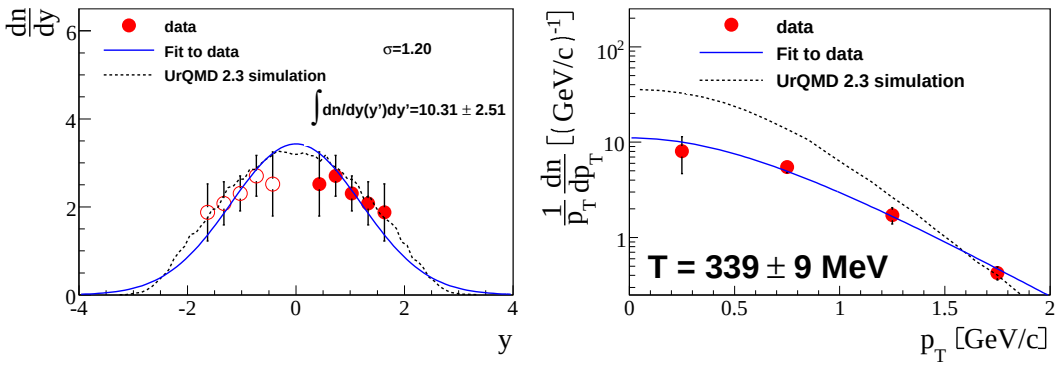

Figure 7.12: Comparison of the data and the UrQMD results of rapidity, and transverse momentum spectra for $K^*(892)$ in central Pb+Pb collisions at 158A GeV.

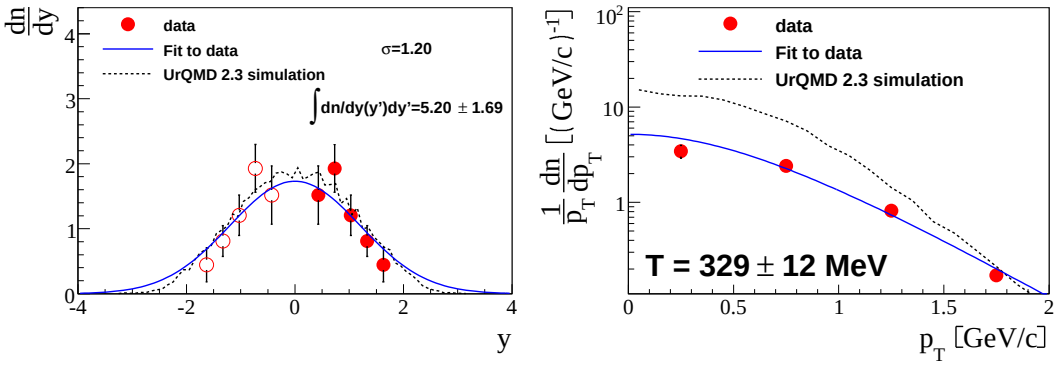

Figure 7.13: Comparison of the data and the UrQMD results of rapidity, and transverse momentum spectra for $\bar{K}^*(892)$ in central Pb+Pb collisions at 158A GeV.

7.3 Comparison with Hadron-resonance Gas Model

The statistical Hadron-resonance Gas Model (HGM) [106] has been found to provide a good description of total yields of stable hadrons produced in elementary $e^+ + e^-$, $p + p$ interactions and central nucleus+nucleus collisions using as adjustable parameters the hadronisation temperature T_{chem}, the baryochemical potential μ_B and the system volume V [106, 107].

The system volume V together with the strangeness saturation factor γ_S are introduced [106]. The comparison of the mean multiplicities of $K^*(892)$, $\bar{K}^*(892)$, $\Lambda(1520)$ and $\phi(1020)$ in central Pb+Pb collisions at 158A GeV [79, 67] with the HGM [106] is shown in Fig. 7.14. In this version of the HGM an additional non-equlibrium parameter, the strangeness saturation factor γ_s was used. The model predictions are indicated by the dashed line and are taken from Ref. [106]. Yields of all measured resonances are smaller than the corresponding HGM predictions. This is quantify in Figs 7.15 and 7.16 where the ratio of the measured yield to the HGM yield for the resonances is plotted as a function of the resonance lifetime and for $K^*(892)$, $\bar{K}^*(892)$ as a function of the number of wounded nucleons, respectively. The ratio decreases with decreasing life time and it is the lowest (≈ 0.44) for $K^*(892)$, $\bar{K}^*(892)$. These findings further support the interpretation of the observed suppression of the resonance yield in central Pb+Pb collisions as due to interactions of the decay products in the hadronic phase. The HGM model assumes that the chemical and thermal freeze-out points coincide and it does not take into account the rescattering of the decay products. As argued previously, the rescattering effect and thus the yield suppression, should increase with decreasing resonance life time and increasing system size (life time). These behaviours are in fact seen in Figs 7.15 and 7.16.

Thus, the investigation of resonances with a mean life time similar to the life time of the

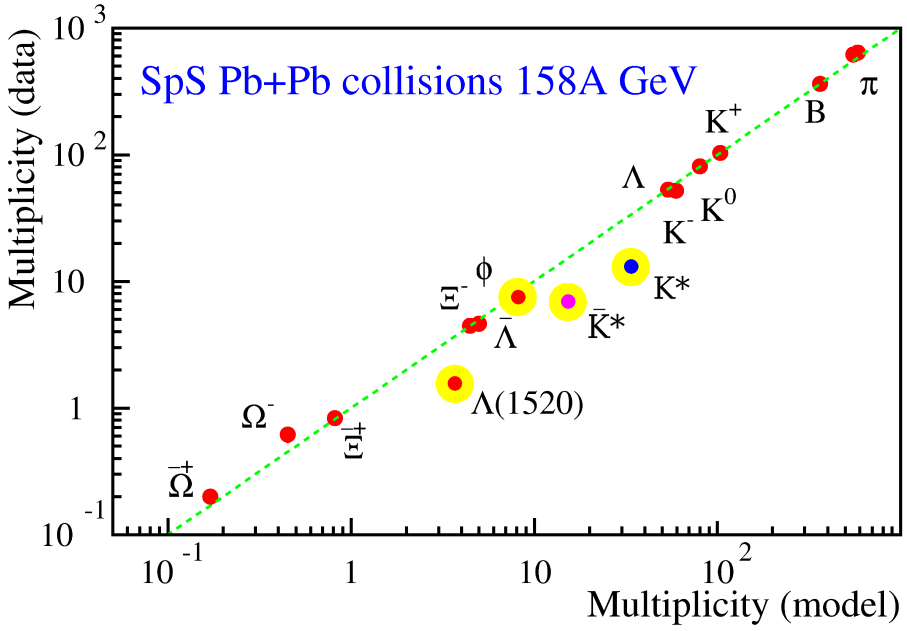

Figure 7.14: Mean hadron multiplicities in central Pb+Pb collisions at 158A GeV measured by the NA49 (closed points) and predicted by the hardron gas model (dashed line) [108].

fireball gives an evidence for creation in central Pb+Pb collisions of a long lived hadronic phase. Due to short mean lifetime, as for $K^*(892)$ with $c\tau = 3.91$ fm/c and for $\Lambda(1520)$ with $c\tau = 12.7$ fm/c, the yield of reconstructable resonances is strongly suppressed (see Table 7.4). However, $K^*(892)$ and $\bar{K}^*(892)$ (and resonances, in general) can be also regenerated from kaon and pion interactions in the hadronic phase. The data clearly indicate that the suppression due to the decay product rescattering dominates over a possible enhancement due to the regeneration (see Table 7.5).

	cτ [fm/c]	yield$_{DATA}$	yield$_{HGM}$
$K^*(892)^0$	3.91	14.23 ± 3.42	32.5
$\bar{K}^*(892)^0$	3.91	7.18 ± 2.30	15.5
$\Lambda(1520)$	12.7	1.57 ± 0.44	3.34
$\phi(1020)$	44	7.60 ± 1.10	8.59

Table 7.4: The measured resonance yield and the yield predicted by the HGM model [106] in central Pb+Pb collisions at 158A GeV versus the resonance lifetime (5% most central) [79, 67].

N_w	$K^*(892)^0_{DATA}$	K^*_{HGM}	$\bar{K}^*(892)^0_{DATA}$	$\bar{K}^*_{HGM}$
2	0.0792 ± 0.0016	0.0563	0.0559 ± 0.0011	0.0316
14	0.80 ± 0.24	0.93	0.43 ± 0.14	0.43
37	2.20 ± 0.66	2.70	1.30 ± 0.40	1.27
262.3	14.23 ± 3.42	32.5	7.18 ± 2.30	15.5

Table 7.5: The $K^*(892)^0$ and $\bar{K}^*(892)^0$ yields for data to the HGM model [106] versus the number of wounded nucleons for p+p, C+C, Si+Si interaction [80] and central Pb+Pb collisions at 158A GeV (5% most central).

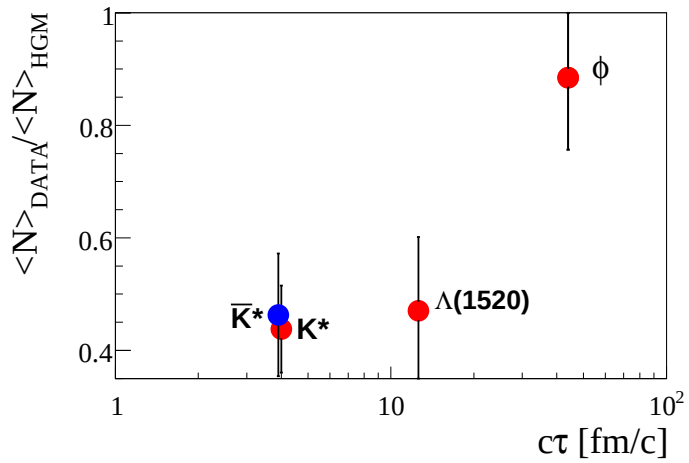

Figure 7.15: The ratio of the measured resonance yield to the yield predicted by the HGM model in central Pb+Pb collisions at 158A GeV versus the resonance lifetime.

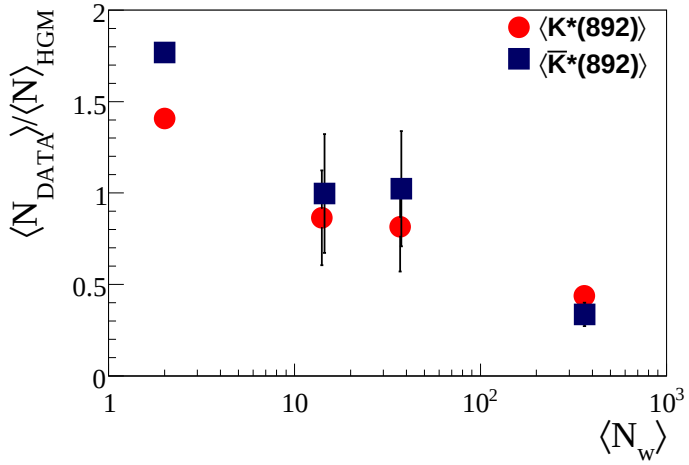

Figure 7.16: The ratio of $K^*(892)^0$ and $\bar{K}^*(892)^0$ yields of data to HGM model yields versus the number of wounded nucleons for p+p, C+C, Si+Si interactions [80] and for central Pb+Pb collisions at 158A GeV.

Chapter 8

Summary and conclusions

In this work production properties of K^* and $\bar{K}^*$ resonances in central Pb+Pb collisions at 158A GeV have been analysed. The experimental data were registered by the NA49 experiment at the CERN SPS.

The production of resonances in nucleus-nucleus collisions is expected to be sensitive to the properties of strongly interacting matter created in these collisions. In particular, the production of strange resonances like K^* and $\bar{K}^*$ may be affected by the onset of deconfinement. The K^* and $\bar{K}^*$ mesons are short lived particles. Their lifetime (c$\tau \approx 4$ fm/c) is comparable to the life time of the fireball created in collisions. They are expected to be sensitive to the strangeness production, to the properties of the hadron phase (rescattering, regeneration) and to the properties of hadrons in the dense medium (absorption). Resonances which decay into strongly interacting particles in a dense medium are less likely to be reconstructed due to the rescattering of daughter particles [71]. The regeneration effect ($K\pi \rightarrow K^* \rightarrow K\pi$) may partially compensate losses due the rescattering and absorption if the expansion of the produced matter is long (> 20 fm/c) [71]. The K^* and $\bar{K}^*$ contain strange quarks. Thus, they are expected to be sensitive to the strangeness content of the system which is established at the early stage of collision [109].

In order to investigate the properties of the K^* and $\bar{K}^*$ meson production in central Pb+Pb collisions at 158A GeV, the author of this thesis:

- extracted raw signals of K^* and $\bar{K}^*$ mesons from the invariant mass spectra in rapidity and transverse momentum bins,
- fitted the position and width of the signal distributions,

- evaluated corrections to the raw spectra for the losses due to the limited geometrical acceptance, tracking inefficiency and track quality cuts,
- obtained corrected rapidity, transverse momentum and transverse mass spectra,
- extrapolated rapidity spectra to unmeasured regions and extracted mean multiplicities of K^* and $\bar{K}^*$ resonances,
- calculated statistical and systematic errors for the above results,
- compared the results with other data on resonance production,
- compared the results with the UrQMD and HG models.

The final results on the the K^* and $\bar{K}^*$ production properties in central Pb+Pb collisions at 158A GeV can be summarized as follows:

- the position of the K^* and $\bar{K}^*$ signals is systematically lower (by about 1%) than the corresponding PDG value,
- the width of the signal is consistent with the corresponding PDG value,
- the rapidity spectra for both K^* and $\bar{K}^*$ are consistent with the Gaussian with $\sigma = 1.2$,
- the transverse momentum or equivalently transverse mass spectra agree with the Boltzmann shape in m_T with the fitted inverse slope parameter, $T = 337 \pm 8$ MeV/c and $T = 323 \pm 12$ MeV/c for K^* and $\bar{K}^*$, respectively,
- the mean multiplicities in central Pb+Pb at 158 A GeV are evaluated to be $\langle K^* \rangle = 10.31 \pm 1.58$ and $\langle \bar{K}^* \rangle = 5.20 \pm 0.99$.

The comparison with the world data on resonance production in nucleus-nucleus collisions indicates that:

- a decrease of the peak position is observed also for K^* and $\bar{K}^*$ and other resonances at RHIC,
- the K^*/K^+ and $\bar{K}^*/K^-$ ratios at 158A GeV decrease with the system size (the number of wounded nucleons) by a factor of about 4 when going from p+p interactions to central Pb+Pb collisions,

- the decrease at $158A$ GeV is two times stronger than the one measured at the top RHIC energy,
- the K^*/K^+ and $\bar{K}^*/K^-$ ratios in central Pb+Pb (Au+Au) collisions increase with increasing collision energy.

The comparison with the string-hadronic model UrQMD and the Hadron-resonance Gas Model indicates:

- the mean multiplicities of K^* and $\bar{K}^*$ are lower than the HGM predictions by a factor of about 3,
- the suppression of the resonance yield with respect to the HGM predictions increases with decreasing resonance life-time,
- the UrQMD model approximately reproduces the rapidity spectra and mean multiplicities of K^* and $\bar{K}^*$ mesons; this is because the rescattering of the decay products is introduced in the model, resulting in the yield reduction by a factor of about 3,
- the UrQMD predicts steeper than the data transverse mass spectra, suggesting that the transverse expansion of the matter in the UrQMD is not sufficient.

The encouraging results of this work motivate further studies of the resonance production in the full energy range of the CERN SPS. These systematic data may reveal features which could be attributed to the onset of deconfinement at the low SPS energies. Additionally, an analysis of the ρ resonance production, with the life-time shorter than K^* one was just started. The results should help to clarify the role of absorption, rescattering and regeneration.

Appendix A

Kinematic variables

A particle produced in a collision can be characterized by its four momentum p^{μ}.

$$p^{\mu} = \begin{pmatrix} E \\ p_x \\ p_y \\ p_z \end{pmatrix} = \begin{pmatrix} E \\ \vec{p} \end{pmatrix} = \begin{pmatrix} E \\ \vec{p_T} \\ p_z \end{pmatrix} \tag{A.1}$$

For convenience, cylindrical coordinate system is often used. In this case the momentum vector is given in terms of transverse momentum, longitudinal momentum (along the beam axis) and azimuthal angle. Longitudinal momentum is not invariant under Lorentz transformation along the beam axis, whereas transverse momentum and azimuthal angle are invariant. Transverse momentum is defined as:

$$p_T = \sqrt{p_x^2 + p_y^2} \tag{A.2}$$

azimuth angle ϕ is given by:

$$\phi = \arctan\left(\frac{p_y}{p_x}\right), \tag{A.3}$$

and total momentum is equal to:

$$p = \sqrt{p_x^2 + p_y^2 + p_z^2}\,. \tag{A.4}$$

Longitudinal motion of a particle is often quantify by its rapidity defined as:

$$y = \frac{1}{2} \ln \left(\frac{E + p_z}{E - p_z} \right) , \tag{A.5}$$

which has transformation properties similar to non-relativistic velocity. Inspired by thermodynamical models one often uses transverse mass:

$$m_T = \sqrt{p_T^2 + m^2} . \tag{A.6}$$

The energy E can be expressed as:

$$E = \sqrt{p^2 + m^2} = m_T \cosh (y) , \tag{A.7}$$

and longitudinal momentum p_z as:

$$p_z = m_T \sinh (y) . \tag{A.8}$$

Rapidity (see equation A.5) can be easily transformed from laboratory frame to center-of-mass system:

$$y_{CMS} = y_{LAB} - y_{mid} , \tag{A.9}$$

where y_{mid} is a rapidity of center-of-mass system in laboratory frame. For high momentum particles $(p >> m)$ rapidity can be approximated by pseudo-rapidity η which depends only on polar angle as:

$$\eta = - \ln \left[\tan \left(\frac{\theta}{2} \right) \right] \tag{A.10}$$

where θ is the polar angle in the laboratory rest frame. Pseudo-rapidity can be also expressed as (equation A.5):

$$\eta = \frac{1}{2} \ln \left(\frac{|p| + p_z}{|p| - p_z} \right) . \tag{A.11}$$

In terms of pseudo-rapidity, total momentum is given as:

$$p = p_T \cosh(\eta) \tag{A.12}$$

and the longitudinal momentum reads:

$$p_z = p_T \sinh(\eta) \tag{A.13}$$

Pseudorapidity is often used by experiments which do not measure particle momenta and masses.

The center-of-mass energy in elementary collision is given by:

$$\sqrt{s} = \sqrt{(E_1 + E_2)^2 - (\vec{p_1} + \vec{p_2})^2}\ , \tag{A.14}$$

where E_1, p_1 and E_2, p_2 are energy and momentum of two colliding nuclei. In fixed target experiments such as NA49 $E_2 = m$, $p_2 = 0$ and consequently:

$$\sqrt{s} = \sqrt{2m^2 + 2mE_2}\ . \tag{A.15}$$

The c.m.s. energy per nucleon-nucleon pair in collisions of two identical nuclei of fixed target experiment is:

$$\sqrt{s_{NN}} = \sqrt{2m_N^2 + 2m_N E_N}\ , \tag{A.16}$$

where m_N and E_N are mass and energy of a projectile nucleon, respectively.

Appendix B

T49MultiMixer class of the T49 analysis framework

The algorithm of invariant mass background description was briefly introduced in chapter 5 (section 5.3.2). The new approach to calculate the mixed event background was implemented for this analysis. In order to standardize the mixing procedures new class has been developed (`T49MultiMixer`). This class was add to the `T49ANA` library of the T49 analysis framework. In order to subtract a background from an invariant mass distribution resulting from data analysis, mixed events are created from uncorrelated pairs of particles. To generate mixed events the track pools are filled with a few hundred events. The mixed events are created by a random selection of tracks from a pool. It was assured that in a mixed event opposite charged tracks come from different real data events. The basic class of the mixing procedure is called `T49Mixing`.

B.1 T49MultiMixer

Inclusive particle spectra depend on multiplicity and veto energy. Consequently, a shape of the invariant mass spectrum also depends on these quantities. In order to take this effect into account mixed events were constructed using real events of similar multiplicity or veto energy. For the final analysis mixing within multiplicity bin of $\Delta N = 20$ was used. Finally, the mixed event invariant mass spectra obtained in multiplicity bins were averaged with multiplicity distribution of real events.

The `T49MultiMixer` class header is presented bellow:

```
class T49MultiMixer : public TObject {

public:

T49MultiMixer();
T49MultiMixer(Int_t multi_min, Int_t multi_max, Int_t multi_interval,
Int_t Events, Int_t character);

void Reset();
// Mulitiplicity or Eveto bins selection
Int_t MultiEvetoBins(T49EventRoot *Event,Int_t type);
// Definition type of bins selection add each event in proper T49Mixing
classes pool
void AddEvent(T49EventRoot *Event, TObjArray *P1list, TObjArray *P2list);
// Fill functions for T49ProjBASE classes with proper mixed event
void GetEvents(T49Proj2BASE *MultiSignal, T49Proj2BASE *MultiMixed);
// Write object output into outside ROOT file
void WriteEvents(TFile *OutFile,T49Proj2BASE *MultiSignal,T49Proj2BASE
*MultiMixed);

protected:

Bool_t fVerbose; // Output control flag
Int_t fType; // Type of bin selection
Float_t fPimass; // Phyical constants: pion mass
Float_t fKmass; // Phyical constants: kaon mass
Float_t fPrmass; // Phyical constants: proton mass
Int_t fNMixed; // Definition for mixing procedures
Bool_t fFirstMix; // Definition for mixing procedures

Int_t fRanges; // Range definition for custom variable
Int_t fMulti_min; // Range definition for custom variable
```

```
Int_t fMulti_max; // Range definition for custom variable
Int_t fMulti_interval; // Range definition for custom variable

Int_t fEvents; // Number of events to be processed
Int_t fEvent_counter; // Number of processed events

T49Mixing **fEventMixer; // Define the event-mixer with 10 events
in the pool

TObjArray *fMultiPosParticleList;
TObjArray *fMultiNegParticleList;
TObjArray *fMultiMixedPosParticleList;
TObjArray *fMultiMixedNegParticleList;

ClassDef(T49MultiMixer,1) // Event mixer for list of T49ParticleRoot

};
```

B.2 Example macro for T49MultiMixer

An example macro with marked important declarations is shown to illustrate how to use the `T49MultiMixer` class.

```
bold type = 1; // analysis in multiplicity bins
// For computing in multiplicity bins
const Int_t multi_min = 400;
const Int_t multi_max = 1600;
const Int_t multi_interval = 20;
type = 2; // analysis in eveto bin
const Int_t multi_min = 0;
const Int_t multi_max = 24000;
const Int_t multi_interval = 4000;
// Define the event-multi-mixer with multi minimum and maximum common
variable;
T49MultiMixer *MultiMixer = new
T49MultiMixer(multi_min,multi_max,multi _interval,nMaxEvent,type);
while ((Event = (T49EventRoot *)
Run->GetNextEvent(RunType,StartAtRun,EndAtRun)) && (nEvent < nMaxEvent))
{
/* ... */
// You must define positive and negative tracks: TObjArray *PosParticleLi
// *NegParticleList;
// You must define the event object: T49EventRoot *Event;
/* ... */
MultiMixer->AddEvent(Event,PosParticleList,NegParticleList);
//You must define: T49Proj2BASE *Signal,*Mixed
MultiMixer->GetEvents(Signal,Mixed);
/* ... */
}
```

B.3 K^* Comparison of T49Mixing and T49MultiMixer spectra

The invariant mass spectra of K^* after background subtraction obtained using the standard mixer (`T49Mixing`) and the multiplicity mixer (`T49MultiMixer`) are compared in (Fig. B.1). Clearly, the multiplicity mixer results in improved description of the background and thus allows a more precise extraction of the signal.

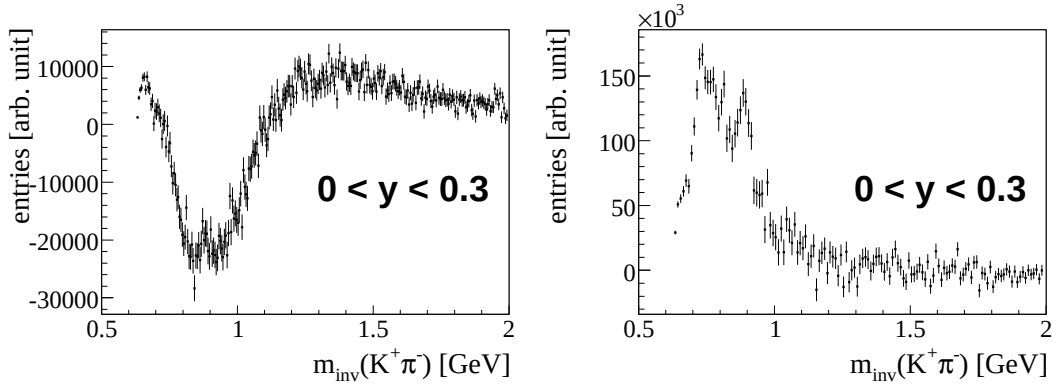

Figure B.1: The invariant mass spectra of $K^+\pi^-$ pairs after background subtraction in the center-of-mass rapidity interval $(0 < y < 0.3)$. The background was calculated using the standard mixing procedures (left), and the multiplicity mixing (right).

Appendix C

m_{inv} spectra for different dE/dx selections

In order to estimate systematic uncertainties of K^* and $\bar{K}^*$ spectra three dE/dx bands with the width of $\pm 2\Delta$, $\pm 2.5\Delta$ and $\pm 3\Delta$ around the mean kaon dE/dx value were used for selection of kaon candidates. The pion dE/dx selection band was kept unchanged and equal to $\pm 3\Delta$ around the Bethe-Bloch pion dE/dx. The parameter Δ was set to be 0.05 of the mean dE/dx for minimum ionizing particles (MIP), which for NA49 dE/dx calibration is equal to one. The invariant mass spectra calculated for $\pm 2\Delta$ and $\pm 3\Delta$ in rapidity and transverse momentum bins are shown in Figs C.1, C.2, C.3, C.4 and in Figs C.5, C.6, C.7, C.8, respectively. The spectra for $\pm 2.5\Delta$ are shown in section 5.3.

C.1 dE/dx band with width of $i \pm 2\Delta$ around the mean of kaon

C.1.1 $K^*(892)^0$ in y and p_T bins

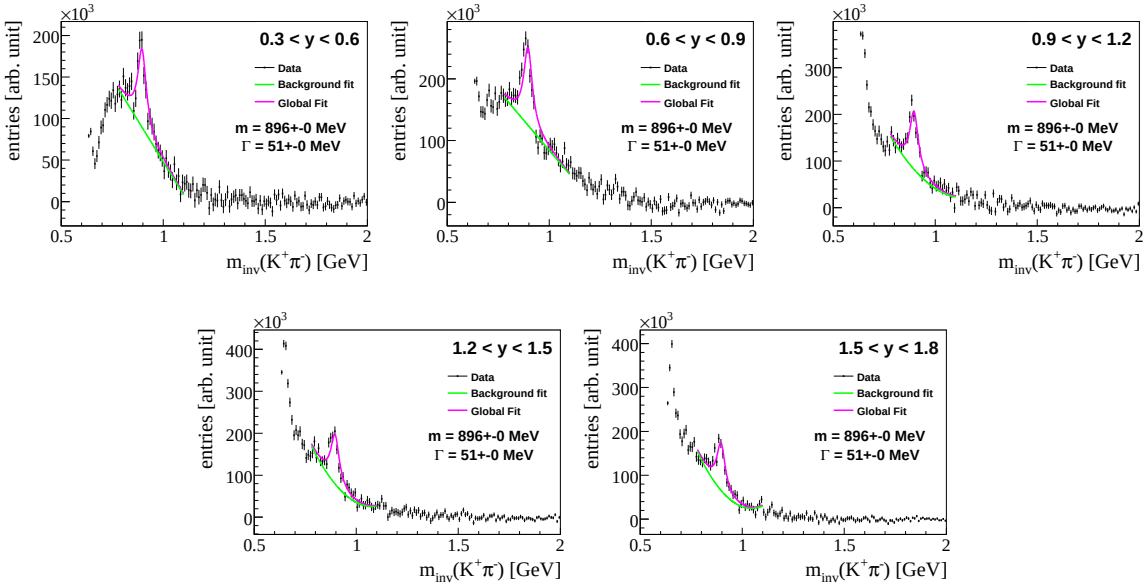

Figure C.1: The K^* invariant mass spectra in rapidity intervals for the kaon dE/dx band $\pm 2\Delta$.

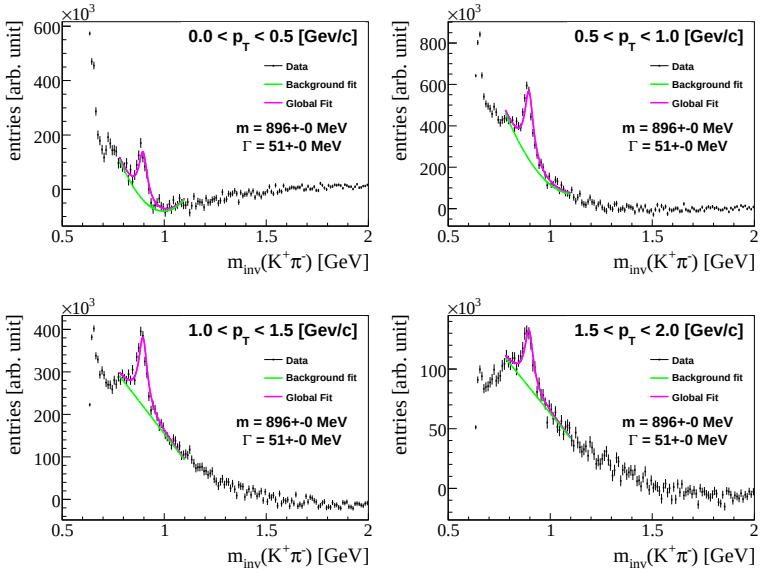

Figure C.2: The K^* invariant mass spectra in transverse momenta intervals for the kaon dE/dx band $\pm 2\Delta$ ($0.43 < y < 1.78$).

C.1.2 $\bar{K}^*(892)^0$ in y and p_T bins

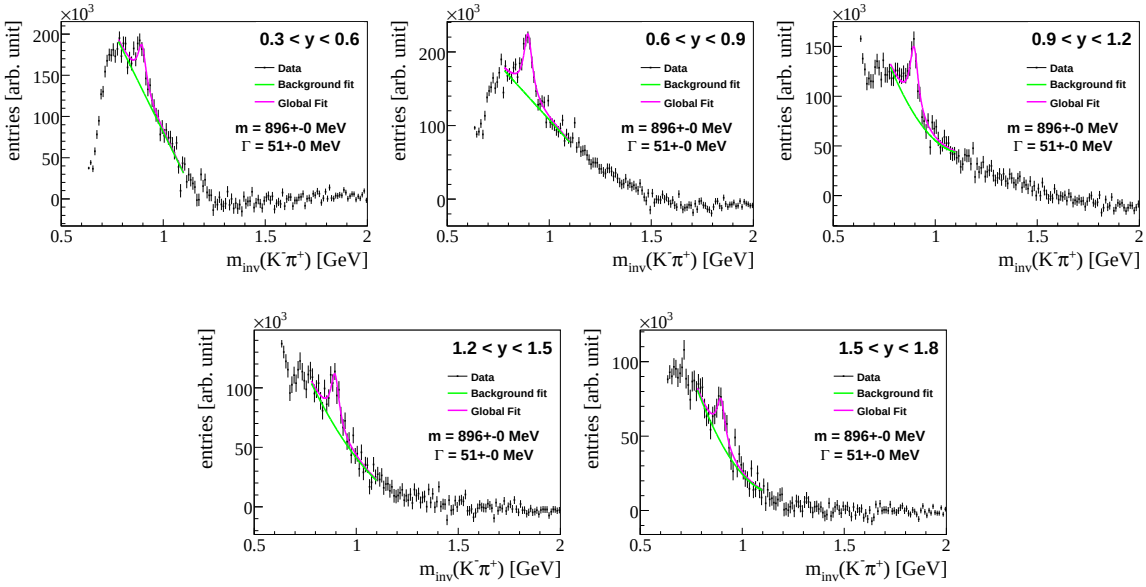

Figure C.3: The $\bar{K}^*$ invariant mass spectra in rapidity intervals for the kaon dE/dx band $\pm 2\Delta$.

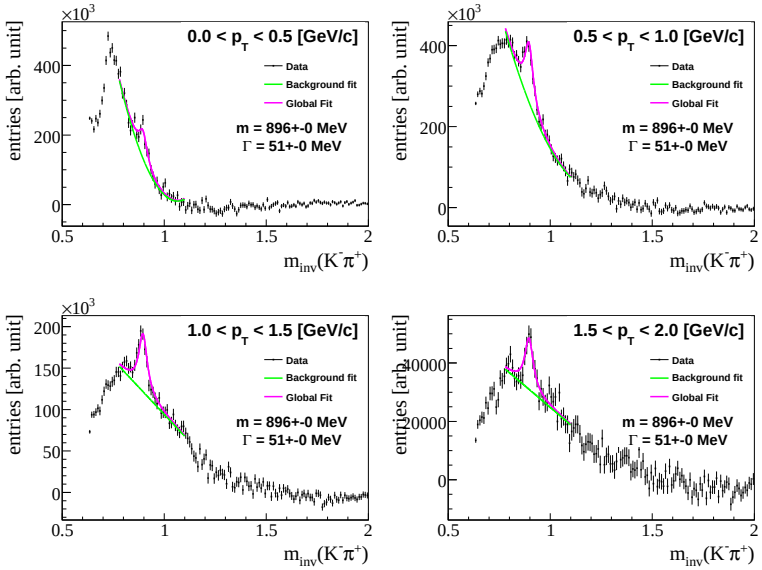

Figure C.4: The $\bar{K}^*$ invariant mass spectra in transverse momenta intervals for the kaon dE/dx band $\pm 2\Delta$ ($0.43 < y < 1.78$).

C.2 dE/dx band with width of $i \pm 3\Delta$ around the mean kaon

C.2.1 $K^*(892)^0$ in y and p_T bins

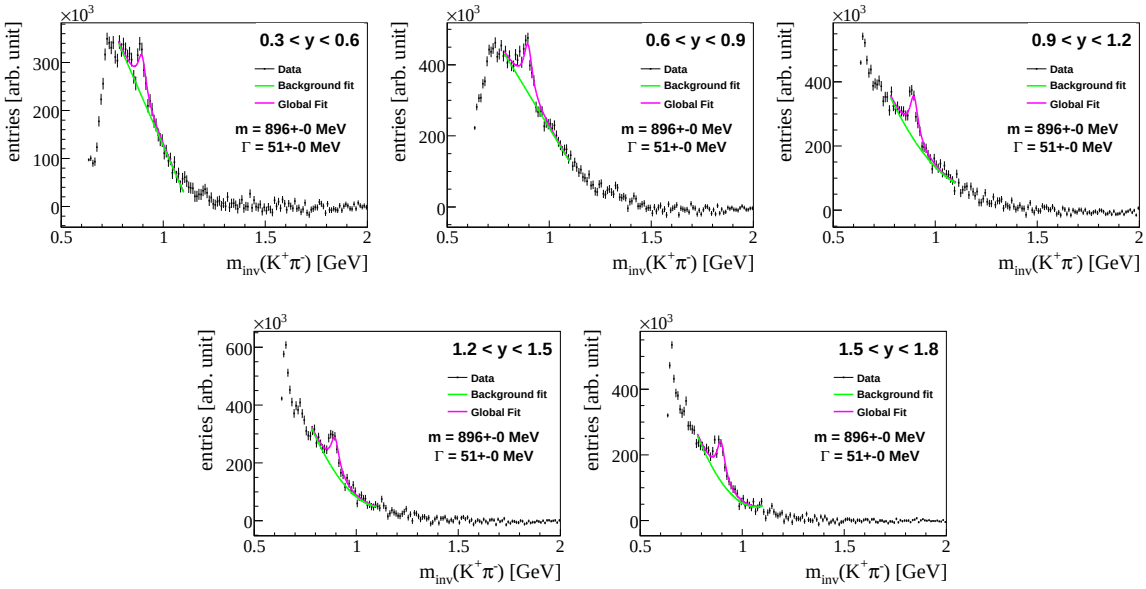

Figure C.5: The K^* invariant mass spectra in rapidity intervals for the kaon dE/dx band $\pm 3\Delta$.

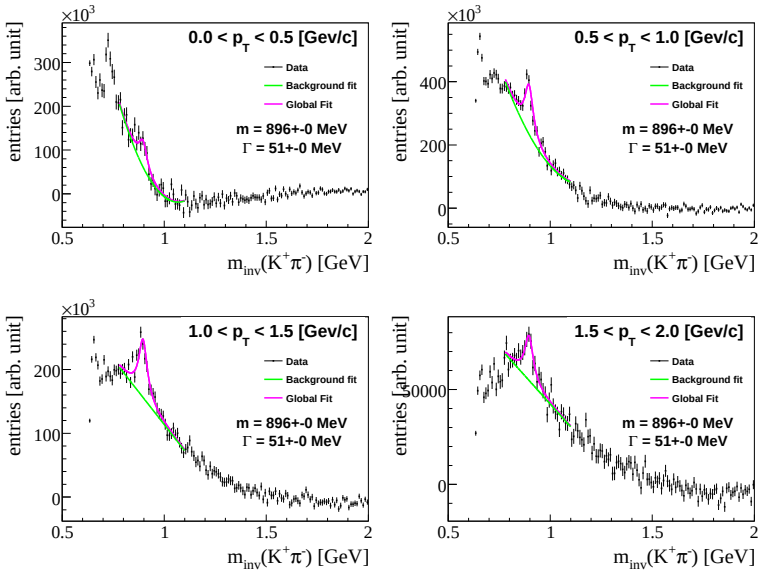

Figure C.6: The K^* invariant mass spectra in transverse momenta intervals for the kaon dE/dx band $\pm 3\Delta$ ($0.43 < y < 1.78$).

C.2.2 $\bar{K}^*(892)^0$ in y and p_T bins

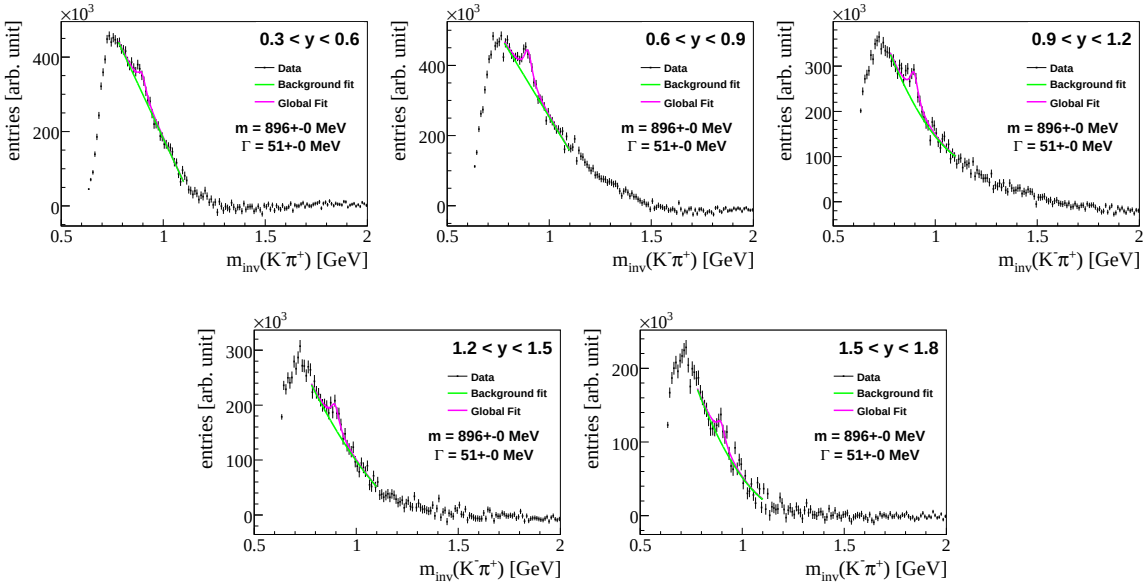

Figure C.7: The $\bar{K}^*$ invariant mass spectra in rapidity intervals for the kaon dE/dx band $\pm 3\Delta$.

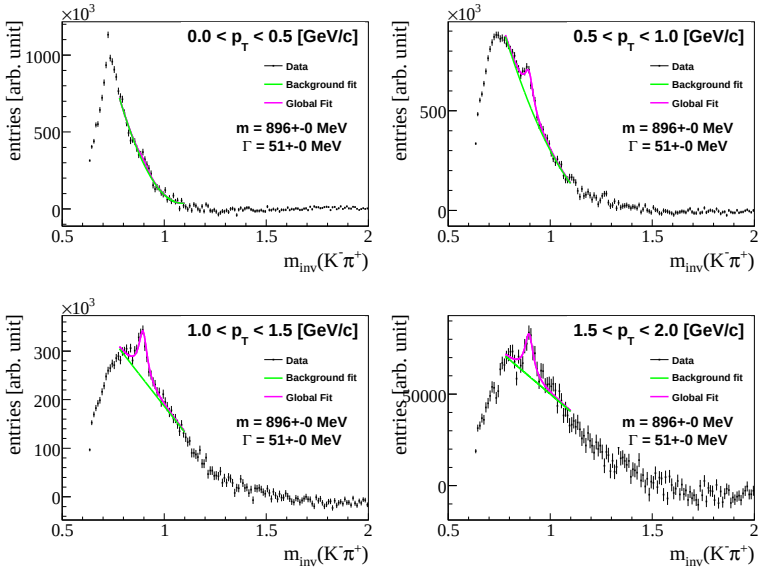

Figure C.8: The $\bar{K}^*$ invariant mass spectra in transverse momenta intervals for the kaon dE/dx band $\pm 3\Delta$ ($0.43 < y < 1.78$).

Appendix D

m_{inv} spectra with scaled momenta

In this appendix the invariant mass spectra in rapidity and transverse momentum bins calculated using scaled momenta are presented. The momentum determination in NA49 has maximum systematic error of about 1%. This bias is possible due to systematic error in the absolute normalization of the magnetic field [67]. Figs D.1 and D.2 show invariant mass spectra in the rapidity and p_T intervals calculated using momentum vectors scaled by 0.99, whereas the spectra obtained scaling momentum vectors by 1.01 are presented in Figs D.3 and D.4. The difference between the peak position extracted from the unscaled and scaled spectra is about 5 MeV.

D.1 K^* Distributions recalculated with momentum vectors scaled by factor 0.99

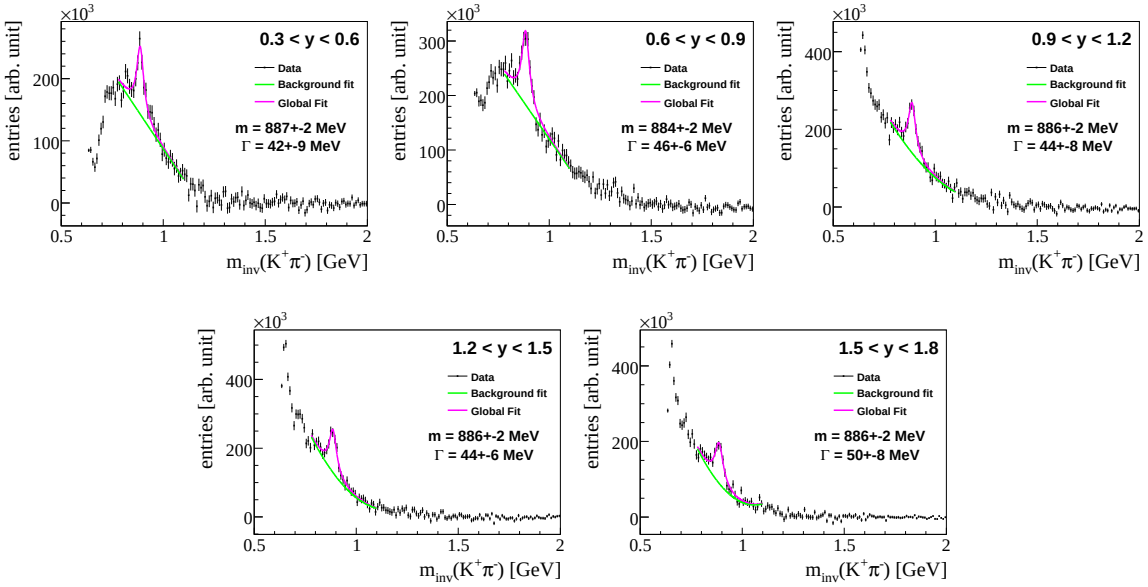

Figure D.1: The invariant mass spectra in the rapidity intervals with momentum vectors scaled by 0.99. Standard selection of particles is used.

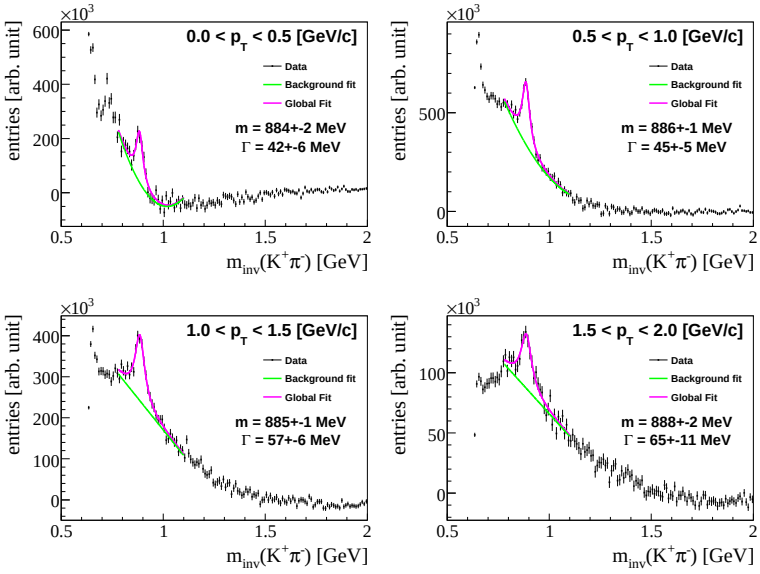

Figure D.2: The invariant mass spectra in the transverse momenta intervals with momentum vectors scaled by 0.99. Standard selection of particles is used.

D.2 Distributions recalculated with momentum vectors scaled by factor 1.01

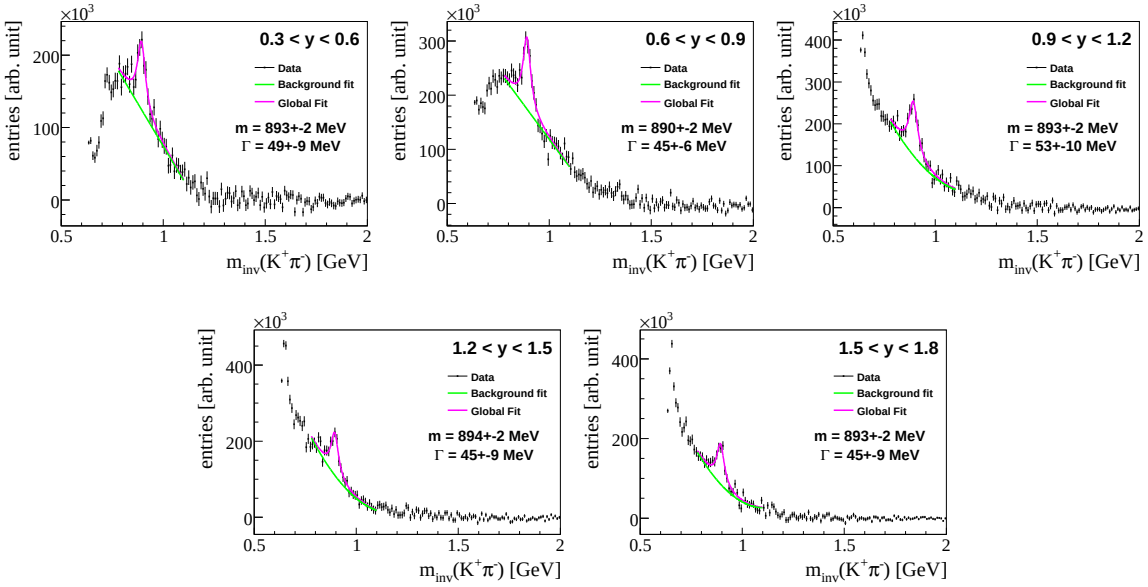

Figure D.3: The invariant mass spectra in the rapidity intervals with momentum vectors scaled by 1.01. Standard selection of particles is used.

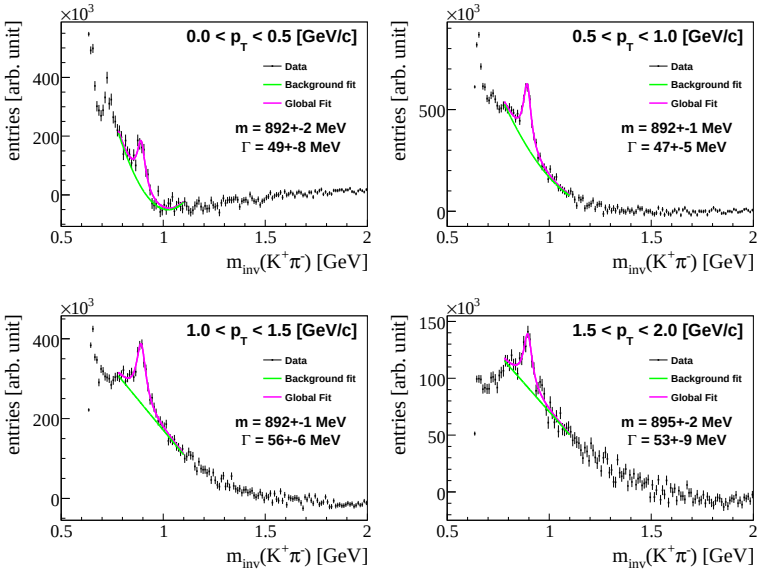

Figure D.4: The invariant mass spectra in the transverse momentum intervals with momentum vectors scaled by factor 1.01. Standard selection of particles is used.

List of Figures

List of Tables

Bibliography

[1] Gaździcki M.,*"http://na61.web.cern.ch/na61/public/physicsGoals/onsetOfDeconfiment.html"*, web site

[2] Griffiths D., *"Introduction to elementary particles",*, Weinheim, USA: Wiley-VCH ISBN 0-471-60386-4 (2008) 454 p

[3] Bromley D. A., *"Gauge Theory of Weak Interactions"*, Springer ISBN 3-540-67672-4 (2000).

[4] Kane G. L., *"Modern Elementary Particle Physics"*, Redwood city, USA: Addison-Wesley ISBN 0-201-11749-5 (1987) 344 P. (The advanced book program)

[5] Bugel L., *"http://home.fnal.gov/ bugel/smc.gif"*, web site

[6] Usai G., *"http://gruppo3.ca.infn.it/usai/cmsimple3_0/images/UniverseEvolution1.png"*, web site

[7] Collins J. C. and Perry M. J., *"Superdense Matter: Neutrons Or Asymptotically Free Quarks?,"* Phys. Rev. Lett. **34** (1975) 1353.

[8] Fachini P., *"Resonance production"*, J. Phys. G **30** (2004) S735 [arXiv:nucl-ex/0403026].

[9] Becattini F. , Gazdzicki M. and Sollfrank J., *"On chemical equilibrium in nuclear collisions"*, Eur. Phys. J. C **5** (1998) 143 [arXiv:hep-ph/9710529].

[10] Stephanov M. A., *"QCD phase diagram: An overview"*, PoS **LAT2006** (2006) 024 [arXiv:hep-lat/0701002].

[11] Fodor Z. and Katz S. D., *"Lattice determination of the critical point of QCD at finite T and μ"*, JHEP **0203** (2002) 014 [arXiv:hep-lat/0106002].

[12] Fodor Z. and Katz S. D., *"Critical point of QCD at finite T and mu, lattice results for physical quark masses"*, JHEP **0404** (2004) 050 [arXiv:hep-lat/0402006].

[13] Stephanov M. A., *"QCD phase diagram and the critical point"*, Prog. Theor. Phys. Suppl. **153** (2004) 139 [Int. J. Mod. Phys. A **20** (2005) 4387] [arXiv:hep-ph/0402115].

[14] Stephanov M. A., Rajagopal K. and Shuryak E. V., *"Signatures of the tricritical point in QCD"*, Phys. Rev. Lett. **81** (1998) 4816 [arXiv:hep-ph/9806219].

[15] Stock R., *"Relativistic nucleus nucleus collisions: From the BEVALAC to RHIC"*, J. Phys. G **30**, S633 (2004) [arXiv:nucl-ex/0405007].

[16] Y. Hatta and T. Ikeda, *"Universality, the QCD critical / tricritical point and the quark number susceptibility"*, Phys. Rev. D **67** (2003) 014028 [arXiv:hep-ph/0210284].

[17] Grebieszkow K.,et al., *"Event-by-event transverse momentum fluctuations in nuclear collisions at CERN SPS"*, PoS C **POD07** (2007) 022 [arXiv:0707.4608 [nucl-ex]].

[18] Heinz U. W., *"Early collective expansion: Relativistic hydrodynamics and the transport properties of QCD matter"*, (2009) arXiv:0901.4355 [nucl-th].

[19] P. F. Kolb, P. Huovinen, U. W. Heinz and H. Heiselberg, Phys. Lett. B **500**, 232 (2001) [arXiv:hep-ph/0012137].

[20] Teaney D., Lauret J. and Shuryak E. V., *A hydrodynamic description of heavy ion collisions at the SPS and RHIC*, (2001) arXiv:nucl-th/0110037.

[21] Slodkowski M., et al., *"The new computer program for three dimensional relativistic hydrodynamical model"*, Acta Phys. Hung. A **27** (2006) 373 [arXiv:nucl-th/0601095].

[22] Rischke D. H., Pursun Y. and Maruhn J. A., *"Relativistic hydrodynamics for heavy ion collisions. 2. Compression of nuclear matter and the phase transition to the quark - gluon plasma"*, Nucl. Phys. A **595**, 383 (1995) [Erratum-ibid. A **596**, 717 (1996)] [arXiv:nucl-th/9504021].

[23] Rischke D. H., Bernard S. and Maruhn J. A., *"Relativistic hydrodynamics for heavy ion collisions. 1. General aspects and expansion into vacuum"*, Nucl. Phys. A **595** (1995) 346 [arXiv:nucl-th/9504018].

[24] Bernard S., Maruhn J. A. , Greiner W. and Rischke D. H., *"Relativistic Hydrodynamics for Heavy–Ion Collisions: Freeze–Out and Particle Spectra"*, Nucl. Phys. A **605**, 566 (1996) [arXiv:nucl-th/9602011].

[25] Rischke D. H., *"Fluid dynamics for relativistic nuclear collisions"*, (1998) arXiv:nucl-th/9809044.

[26] Rafelski J. and Letessier J., *"Sudden hadronization in relativistic nuclear collisions"*, Phys. Rev. Lett. **85** (2000) 4695 [arXiv:hep-ph/0006200].

[27] Alt C., et al., *"http://na49info.web.cern.ch/na49info/na49"*, web site

[28] Mitrovski M. K., *"Energy And System Size Dependence Of Ξ^- And $\bar{\Xi}^+$ Production In Relativistic Heavy-Ion Collisions At The Cern Sps"*, Ph.D. thesis NA49 collaboration Wolfgang Goethe-Universität in Frankfurt am Main (2007)

[29] Bass S. A.,et al., *"Microscopic models for ultrarelativistic heavy ion collisions"*, Prog. Part. Nucl. Phys. **41** (1998) 255 [Prog. Part. Nucl. Phys. **41** (1998) 225] [arXiv:nucl-th/9803035].

[30] Bleicher M.,et al., *"Relativistic hadron hadron collisions in the ultra-relativistic quantum molecular dynamics model"*, J. Phys. G **25** (1999) 1859 [arXiv:hep-ph/9909407].

[31] Yoo I. K., *"Bose-Einstein correlation of charged kaons and pions in central Pb+Pb collisions at 158A GeV"*, Ph.D. thesis NA49 collaboration Fachbereich Phyisk der Universität, Marburg (2001)

[32] Satz H., *"The SPS heavy ion programme"*, Phys. Rept. **403-404** (2004) 33 [arXiv:hep-ph/0405051].

[33] Jalilian-Marian J., *"Theoretical status of the RHIC program"*, AIP Conf. Proc. **857** (2006) 76.

[34] Gazdzicki M., et al., [NA49-future Collaboration], *"A new SPS programme"*, PoS C **POD2006** (2006) 016 [arXiv:nucl-ex/0612007].

[35] Gaździcki M. and f. t. N. Collaboration, *"Ion Program of Na61/Shine at the CERN SPS"*, (2008) arXiv:0812.4415 [nucl-ex].

[36] Stephans G. S. F, *"critRHIC: The RHIC low energy program"*, J. Phys. G **32** (2006) S447 [arXiv:nucl-ex/0607030].

[37] Barannikova O. and f. t. S. Collaboration, *"STAR: Recent Results and Future Physics Program"*, (2009) arXiv:0901.0535 [nucl-ex].

[38] Baumann C. and f. t. P. Collaboration, *"PHENIX results on the $\sqrt{s_{\rm NN}}$ dependence of jet quenching"*, (2009) arXiv:0901.3435 [nucl-ex].

[39] Gazdzicki M. and Gorenstein M. I., *"On the early stage of nucleus nucleus collisions"*, Acta Phys. Polon. B **30** (1999) 2705 [arXiv:hep-ph/9803462].

[40] Alt C., et al., [NA49 Collaboration], *"Pion and kaon production in central Pb+Pb collisions at 20 A and 30 A GeV: Evidence for the onset of deconfinement"*, Phys. Rev. C **77**, 024903 (2008) [arXiv:0710.0118 [nucl-ex]].

[41] Gazdzicki M., et al., [NA49 Collaboration], *Report from NA49"*, J. Phys. G **30** (2004) S701 [arXiv:nucl-ex/0403023].

[42] Petersen H., Steinheimer J., Bleicher M. and Stoecker H., *"$\langle m_T \rangle$ excitation function: Freeze-out and equation of state dependence"* (2009) arXiv:0902.4866 [nucl-th].

[43] Rafelski J., Muller B., *"Strangeness Production In The Quark - Gluon Plasma"*, Phys. Rev. Lett. **48**, 1066 (1982) [Erratum-ibid. **56**, 2334 (1986)].

[44] Torrieri G., *"Phenomenology of Strangeness enhancement in heavy ion collisions"*, (2009) arXiv:0901.0221 [nucl-th].

[45] Rafelski J., *"Strangeness Enhancement: Challenges and Successes"*, Eur. Phys. J. ST **155** (2008) 139 [arXiv:0710.1931 [nucl-th]].

[46] Matsui T. and Satz H., *"J/ψ Suppression by Quark-Gluon Plasma Formation"*, Phys. Lett. B **178** (1986) 416.

[47] Kharzeev D., Lourenco C., Nardi M. and Satz H., *"A quantitative analysis of charmonium suppression in nuclear collisions"*, Z. Phys. C **74** (1997) 307 [arXiv:hep-ph/9612217].

[48] Abreu M. C.,et al. [NA50 Collaboration], *"Anomalous J/ψ suppression in Pb - Pb interactions at 158 GeV/c per nucleon"*, Phys. Lett. B **410** (1997) 337.

[49] Gazdzicki M., Gorenstein M. I., *"Evidence for statistical production of J/ψ mesons in nuclear collisions at the CERN SPS"*, Phys. Rev. Lett. **83**, 4009 (1999) [arXiv:hep-ph/9905515].

[50] Atomssa E. T. [PHENIX Collaboration], *"J/psi suppression measurements by the PHENIX experiment at RHIC"*, Prepared for 15th International Workshop on Deep-Inelastic Scattering and Related Subjects (DIS2007), Munich, Germany, 16-20 Apr 2007

[51] Shuryak E. V., *"Quark-Gluon Plasma And Hadronic Production Of Leptons, Photons And Psions"*, Phys. Lett. B **78** (1978) 150 [Sov. J. Nucl. Phys. **28** (1978 YAFIA,28,796-808.1978) 408.1978 YAFIA,28,796].

[52] Ruuskanen P. V., *"Electromagnetic probes of quark - gluon plasma in relativistic heavy ion collisions"*, Nucl. Phys. A **544** (1992) 169.

[53] Cassing W. and Bratkovskaya E. L., *"Hadronic and electromagnetic probes of hot and dense nuclear matter"*, Phys. Rept. **308** (1999) 65.

[54] Alam J., Sinha B. and Raha S., *"Electromagnetic Probes Of Quark Gluon Plasma"*, Phys. Rept. **273** (1996) 243.

[55] Yurevich S., *"Electron pair production in 158 AGeV Pb-Au collision from CERES"*, Ph.D. thesis CERES collaboration (2006).

[56] Gyulassy M. and Plumer M., *"Jet Quenching In Dense Matter"*, Phys. Lett. B **243** (1990) 432.

[57] Wang X. N. and Gyulassy M., *"Gluon shadowing and jet quenching in A + A collisions at s**(1/2) = 200-GeV"*, Phys. Rev. Lett. **68** (1992) 1480.

[58] Adams J., et al. [STAR Collaboration], *"Evidence from d + Au measurements for final-state suppression of high $p(T)$ hadrons in Au + Au collisions at RHIC"*, Phys. Rev. Lett. **91**, 072304 (2003) [arXiv:nucl-ex/0306024].

[59] Wigner E. P., *"Resonance Reactions and Anomalous Scattering"*, Phys. Rev. **70** (1946) 15.

[60] Lane A. M., Thomas R. G. and Wigner E. P., *"Giant Resonance Interpretation of the Nucleon-Nucleus Interaction"*, Phys. Rev. **98** (1955) 693.

[61] Gottfried K. and Jackson J. D., *"On the Connection between production mechanism and decay of resonances at high-energies"*, Nuovo Cim. **33** (1964) 309.

[62] Einhorn M. B. and Ellis S. D., *Hadronic Production Of The New Resonances: Probing Gluon Distributions"*, Phys. Rev. D **12** (1975) 2007.

[63] Green M. B. , Jacob M. and Landshoff P. V., *Production Of The New Resonances In Hadronic Collisions"*, Nuovo Cim. A **29** (1975) 123.

[64] Fachini P., *Overview of resonance production"*, J. Phys. G **35** (2008) 044032.

[65] Friese V. [NA49 Collaboration], *"Energy dependence of strangeness production"*, J. Phys. G **31** (2005) S911 [arXiv:nucl-ex/0412013].

[66] Markert C., *"Resonance production in heavy ion collision at STAR"*, J.Phys.G35:044029 (2008).

[67] Friese V., et al., [NA49 collaboration], *"Energy dependence of ϕ meson production in central Pb+Pb collisions at $\sqrt{s}_{NN}$ = 6 to 17 GeV"*, Phys. Rev. C **78** (2008) 044907 [arXiv:0806.1937 [nucl-ex]].

[68] Friese V., et al.,*"Strangeness from 20A GeV to 158A GeV"*, J. Phys. **G30**, S119 (2003)

[69] Abelev B. I.,et al., [STAR Collaboration], *"Measurements of ϕ meson production in relativistic heavy-ion collisions at RHIC"*, (2008) arXiv:0809.4737 [nucl-ex].

[70] Adams J.,et al., [STAR Collaboration], *"$K(892)^*$ resonance production in Au+Au and p+p collisions at $\sqrt{s_{NN}}$ = 200 GeV"* Phys. Rev. C **71** (2005) 064902 [arXiv:nucl-ex/0412019].

[71] Adler C., et al., [STAR Collaboration], *"K^{*0} production in relativistic heavy ion collisions at $\sqrt{s_{NN}} = 130$ GeV"*, Phys. Rev. C **66** (2002) 061901 [arXiv:nucl-ex/0205015].

[72] Dash S., [STAR Collaboration], *"K^* production in Cu+Cu and Au+Au collisions at $\sqrt{s_{NN}} = 62.4$ GeV and 200 GeV in STAR"*, J. Phys. G **35** (2008) 104057 [arXiv:0805.0081 [nucl-ex]].

[73] Torrieri G. and Rafelski J., *"Strange hadron resonances and QGP freeze-out"*, J. Phys. G **28** (2002) 1911 [arXiv:hep-ph/0112195].

[74] Torrieri G. and Rafelski J., *"Strange hadron resonances as a signature of freeze-out dynamics"*, Phys. Lett. B **509** (2001) 239 [arXiv:hep-ph/0103149].

[75] Afanasev S.,et al. [NA49 Collaboration], *"The NA49 large acceptance hadron detector"*, Nucl. Instrum. Meth. A **430** (1999) 210.

[76] Myers S., et al., *"http://public.web.cern.ch/public/en/Research/AccelComplex-en.html"*, web site

[77] Lasiuk B., [NA49 Collaboration], *"Particle identification in the NA49 TPCs"*, Nucl. Instrum. Meth. A **409** (1998) 402.

[78] Grebieszkow K., *"On transverse momentum event-by-event fluctuation in nuclear collisions at CERN SPS"*, Ph.D. thesis NA49 collaboration (2005)

[79] Markert C., *"$\Lambda(1520)$-Produkionen in Proton-Proton und zentralen Blei-Blei Reaktionen bei 158 GeV pro Nukleon"*, Ph.D. thesis NA49 collaboration (2000)

[80] Höhne C., *"System-Size Dependence of Strangeness Production in Heavy Ion Collision at 158 A GeV "*, Ph.D. thesis NA49 collaboration (2003).

[81] Friese V., *"Produktion von ϕ-Mesonen in ultrarelativistischen Stossen zwischen schweren Kernen"*, Ph.D. thesis NA49 collaboration (1999)

[82] DeMarzo C.,et al., *"A Segmented Photon - Hadron Calorimeter Using A Two Colored Wavelength Shifter Optical Readout System"*, Nucl. Instrum. Meth. **217** (1983) 405.

[83] Alt C.,et al., [NA49 Collaboration], *"Energy Dependence of Multiplicity Fluctuations in Heavy Ion Collisions at the CERN SPS"*, (2007) arXiv:0712.3216 [nucl-ex].

[84] Lungwitz B.,et al., [NA49 Collaboration], *"Energy, Rapidity and Transverse Momentum Dependence of Multiplicity Fluctuations in Heavy Ion Collisions at CERN SPS"*, PoS C **POD07** (2007) 023 [arXiv:0709.1646 [nucl-ex]].

[85] van Leeuwen M., *"Kaon and open charm production in central lead lead collisions at the CERN SPS"*, Ph.D. thesis NA49 collaboration (2000)

[86] Zybert R., *"DSPACK release notes"*, internal notes (1995)

[87] Brun R., *"http://root.cern.ch"*, web site

[88] van Leeuwen M., et al., *"Recent results on spectra and yields from NA49"*, Nucl. Phys. A **715** (2003) 161 [arXiv:nucl-ex/0208014].

[89] Lungwitz B., *"Energy Dependence of Multiplicity Fluctuations in Heavy Ion Collisions at the CERN SPS"*, Ph.D. thesis NA49 collaboration (2008)

[90] Bethe H., *"The theory of the passage of rapid neutron radiation through matter"*, ANNALEN DER PHYSIK 5 (3): 325-400 (1930) 325

[91] Bloch F., Z. Physik 81 (1933) 363

[92] Lasiuk B., *"Particle identification using dE/dx and its application for physics"*, NA49 collaboration paper (1999)

[93] van Leeuwen M., *"A practical guide to dE/dx" analysis in NA49"*, collaboration paper (2006)

[94] Leo W. R., *"Techniques for Nuclear and Particle Physics Experiments: a how to approach"* Berlin, Germany: Springer (1987) 368 p

[95] Sikler F.,*http://na49info.web.cern.ch/na49info/na49/Physics/dEdx*, web site.

[96] Roland C., *"Flavor fluctuation in Central Pb+Pb at 158 GeV/Nucleon"*, Ph.D. thesis NA49 collaboration (1999)

[97] Werner K., *"Strings, pomerons, and the venus model of hadronic interactions at ultrarelativistic energies"*, Phys. Rept. **232** (1993) 87.

[98] Gaździcki M., Lungwitz B., *"Compilation of NA49 results"*, NA49 resources (2009)

[99] Apostolakis J., et al., *"http://wwwasd.web.cern.ch/wwwasd/geant"*, web site

[100] Eidelman S.,et al., [Particle Data Group], *"Review of particle physics"*, Phys. Lett. B **592** (2004) 1.

[101] Blume C., [NA49 Collaboration], *"Review of results from the NA49 collaboration"*, J. Phys. G **31** (2005) S685 [arXiv:nucl-ex/0411039].

[102] Gorenstein M. I., Petrov V. K. and Zinovev G. M., *"Phase Transition In The Hadron Gas Model"*, Phys. Lett. B **106** (1981) 327.

[103] Vogel S., Private communication, (2008).

[104] Vogel S. and Bleicher M., *"Resonance absorption and regeneration in relativistic heavy ion collisions"*, (2008) arXiv:nucl-th/0505027.

[105] Bleicher M., and Aichelin J., *"Strange resonance production: Probing chemical and thermal freeze-out in relativistic heavy ion collisions"*, Phys. Lett. B **530** (2002) 81 [arXiv:hep-ph/0201123].

[106] Becattini F., Manninen J., and Gaździcki M., *"Energy and system size dependence of chemical freeze-out in relativistic nuclear collisions"*, Phys. Rev. C **73** (2006) 044905 [arXiv:hep-ph/0511092].

[107] Broniowski W. and Florkowski W., *"Explanation of the RHIC p(T)-spectra in a thermal model with expansion"*, Phys. Rev. Lett. **87**, 272302 (2001) [arXiv:nucl-th/0106050].

[108] Becattini F., Manninen J., Gaździcki M., *"Chemical equilibrium study in nucleus-nucleus collisions at relativistic energies"*, Phys.Rev. C **69**, 024905 (2004)

[109] Seyboth P., et al., *"Recent result from nucleus-nucleus collisions at CERN SPS"*, J.Phys. **G35** Nucl. Part. Phys., 104008 (2008)